To the Graduate Council:

I am submitting herewith a thesis written by SANJEEV KHOSLA entitled "PROPERTIES AND SITE SUBSTITUTIONS FOR TERNARY CHROMIUM ADDITIONS TO B2 IRON ALUMINIDES". I have examined the final copy of this thesis for form and content and recommend that it be accepted in partial fulfillment of the requirements for the degree of Master of Science, with a major in Metallurgical Engineering.

Carl J. McHargue, Major Professor

We have read this thesis
and recommend its acceptance:

Accepted for the Council:

Associate Vice Chancellor
and Dean of the Graduate School

PROPERTIES AND SITE SUBSTITUTIONS FOR TERNARY CHROMIUM ADDITIONS TO B2 IRON ALUMINIDES

A Thesis

Presented for the

Master of Science

Degree

The University of Tennessee, Knoxville

SANJEEV KHOSLA

December 1993

ACKNOWLEDGEMENTS

I would like to thank my advisor, Dr. Carl J. McHargue for his guidance. I would like to express my sincere gratitude to Dr. C. J. Sparks and Dr. Joachim Schneibel , Oak Ridge National Laboratory (ORNL) for their help, guidance and patience in the course of my project work. I would also like to thank Dr. R.A. Buchanan for consenting to be on my Committee.

Thanks are also due to Dr. Eliot Specht, Dr. Gene Ice, Dr. Xiaogang Jiang and Dr. Ravi Kumar (ORNL) for helping me at various stages of my work. I am thankful to Dr. Paul Zschack and Dr. Mitch Nelson at Brookhaven National Laboratory for helping me in the experimentation work. Many thanks to Elmer Lee, Hershel Pierce and Cecil Carmichael (ORNL) for their help and advice in the course of my experimentation work and alloy preparation.

I would like to thank the sponsor of the project, the Division of Materials Sciences, the U.S. Department of Energy under contract DE-AC05-84OR21400 with Martin Marietta Energy Systems, Inc.

Finally, I would like to take this opportunity to thank my parents, grandmother, sister and brother who have encouraged me in all my endevours.

ABSTRACT

The equiatomic and iron-rich ordered iron aluminides are potential medium temperature materials because of their low cost and good elevated temperature properties. However, their chief drawback is their brittleness at room temperature. Attempts have and are being made to increase their ductility by alloying. It has also been established that the site preference of the ternary element could affect the mechanical properties of these aluminides. A study was made of the site substitution of Cr in the B2 FeAl using the variable x-ray energy of a synchrotron source. Seven compositions were chosen of which three were binary FeAl alloys. It was found that Cr had a clear preference for the Al site for all the compositions. The amount of Al on the Fe site varied considerably with specimen composition for the ternary alloys but was relatively independent of composition for the binary alloys. These data represent one of the first systematic studies of the site preference of a ternary addition to a binary compound. Improvements in the sample preparation and data analysis provided significant reductions in uncertainties. These meaningful values of site preference were not strongly correlated with hardness but reflected the chemistry of the binary phases. The hardness values, after cooling from a low - temperature anneal were insensitive to composition except for the $Fe_{51}Al_{49}$ alloy which showed a much higher hardness.

TABLE OF CONTENTS

LIST OF TABLES

LIST OF FIGURES

Chapter 1

Introduction

Intermetallic compounds consisting of a transition metal and aluminum possess high strength, high melting point and oxidation resistance which makes them potential structural materials for high temperature applications [30]. The equiatomic ordered (B2 type) FeAl , because of its low cost has been the subject of much study. The chief drawback of this alloy is its brittleness at low temperature. Attempts to increase its ductility by alloying with ternary additions has met with limited success. It has been established by workers that Ni, Ti, Mn, Co, Cr and Si show complete solubility in the B2 FeAl up to a limit of at least 5 at.% [30]. It has also been established that the site preference of the ternary element can significantly alter the mechanical properties of the base alloy [21].

Munroe and Baker [21] studied the site occupation of 5 at.% Cr in the B2 $Fe_{55}Al_{40}Cr_5$. They compared the 100 and the 200 Bragg reflections of an x-ray diffraction pattern and concluded from the integrated peak intensities of these two reflections that Cr occupied the Al site. However, it may be noted that the atomic scattering factor of Cr is very close to that of Fe, so that the presence of Cr on the Fe site in an Fe-rich alloy would not significantly alter the 100 reflection. This insufficient contrast makes it difficult to determine the site preference of Cr from their data. Munroe and Baker also assumed that there were no anti-site defects present in the alloy, i.e., all the Al was on the Al site, the Fe site had only Fe atoms, with the excess Fe atoms (since the alloy was Fe rich) on the Al site. This assumption is also not valid since Chang, Pike and others have shown the presence of anti-site defects in the equiatomic FeAl [5].

In this study, we have determined the site preference of Cr using the variable energy of an x-ray synchrotron source. By working close to the absorption edges of the constituent elements, we have significantly altered the atomic scattering factors of the elements, which makes it possible to determine with a much better degree of confidence the site preference of Cr. Also we have been able to determine the concentration of anti-site defects, i.e., in this case, the fraction of Al atoms on the Fe site.

Data analysis has been done with the help of the GSAS (Generalized Structure Analysis and Systems) Software written by Robert von Dreele and Allen Larson [15] of Los Alamos National Laboratory. This software uses the Rietveld method of least-squares for refinement and analysis of the data. This method was developed by Rietveld in 1967 [24] and since then is acknowledged as a standard method for analysing x-ray and neutron diffraction data.

In the present work, seven specimens were prepared for site occupation determination. Of these, three were binary FeAl alloys while the others contained Cr, usually less than 5 at.%. Apart from determination of site occupation, hardness values and lattice parameters of these alloys were also determined in an effort to correlate them with site occupancy. However, no correlation with these parameters was observed in the case of these alloys. A theoretical model based on thermodynamic considerations of bond energy, developed by Ochiai and others [23] for determination of site preference of ternary additions was applied to the equiatomic FeAl. The ternary elements considered were those that showed solubility in FeAl up to at least 5 at.%. By this model, it was established by us that amongst the various ternary additions, Cr had the strongest preference for the Al site.

In the next chapter, a literature review pertaining to the mechanical properties and phase relationships of the FeAl alloy will be presented. Some of the

different methods of determining site occupations will be described, with particular emphasis on the method of x-ray and neutron diffraction. A description of the Rietveld method of least-squares will also be made. Chapter 3 describes the experimental work involved and the corrections to the data required for reliable analysis by GSAS. Chapter 4 presents a mathematical approach to determining site occupation by thermodynamic considerations as developed by Ochiai and others, and Chapter 5 mentions the results and discusses the granularity effects, site occupation behavior and the hardness data. Comparision of site occupations with the chemistry of the binary phase diagrams will be made.

Chapter 2

Literature review

2.1 Potential utilities and drawbacks of intermetallics

A major goal is that the good toughness that some metals have and the higher strength that results from the tighter bonds of intermetallics can be combined in some high-temperature intermetallics.

Ordered intermetallics make up a class of compounds that present special opportunities for unusual combinations of lightness and high-temperature strength (and/or stiffness). A compound is ordered if two or more sublattices are needed to describe its atomic structure. An example of such a structure is the simple cubic CsCl (B2) lattice - two interpenetrating simple cubic sublattices with the atoms of each at the body centers of the other. Although stoichiometry is inherent in the idea of a compound, many intermetallics can tolerate appreciable deviations from the ideal, simple concentration ratios. The existence of ordered intermetallic compounds arises when there are stronger bonds between unlike nearest-neighbor atoms than between like nearest-neighbors. As a result, many of these compounds have higher elastic stiffness than their metal constituents have separately [8].

Due to their high strength, high melting point, and oxidation resistance, intermetallic compounds consisting of a transition metal and aluminum have been explored as potential high-temperature materials. The equiatomic body centered cubic (ordered B2) aluminides of Fe, Ni, and Co are considered potential component and structural materials for diverse applications. These include power systems of aircrafts and automobiles, fossil fuel conversion technology, heat exchangers, and recuperators. In these applications, a high modulus, high tensile strength and high temperature creep

strength as well as exceptional oxidation resistance of these intermetallic compounds can improve operation efficiency and reduce component weight [30].

These equiatomic transition metal-aluminides crystallize in a rather simple structure, being ordered bcc or CsCl (B2-type). Most of these intermetallic compounds exist over a wide range of composition. Their properties may be strongly composition-dependent due to the different types and concentrations of point defects. In contrast to traditional solid-solution materials such as ferrous, aluminum, nickel and titanium alloys, our knowledge concerning the structure-property relationships as well as the processing science of the intermetallic compounds is limited [5].

The main drawback to the use of these alloys is their brittleness at room temperature. None of these alloys has exhibited commercially acceptable ductility (> 9 percent) at room temperature [9]. FeAl brittleness, at room temperatures, is attributed to environmental embrittlement and the lack of active slip systems [16] which may lead to intergranular fracture. Furthermore, the FeAl B2 structure is favourable to the formation of vacancies by thermal activation which are retained easily inside the lattice by quenching. This can explain the increased hardness of the quenched alloys at low temperatures, especially for the FeAl stoichiometric composition [16].

2.2 The B2 FeAl intermetallic

The B2 binary FeAl has a melting point in excess of 1500 K, and exists over a wide range of compositions with some solubility for third elements [30]. It is also highly oxidation and sulfidation resistant at elevated temperatures. This resistance stems from the formation of a highly protective and adherent Al_2O_3 scale [18]. In tensile tests, the alloys are brittle up to 400°C but above 600°C, the ductility increases markedly. The densities of these alloys, depending upon the aluminum content, is about 5490 - 6680 kg/m^3, which is 30% lower than those of commercial nickel-base

superalloys [18]. Furthermore, the alloy constituents are not expensive and only small quantities of strategic elements are used [16]. This makes them potentially low-cost structural materials for medium-temperature applications.

2.3 The Fe-Al phase diagram

Figure 2.1 shows the iron-aluminum phase diagram. It can be seen that depending upon composition, iron and aluminum alloyed together exist in a number of crystalline phases at room temperature. Aluminum is only slightly soluble in fcc γ-iron but it is highly soluble in bcc iron with the solubility limit occuring at about 54 at.% aluminum. Within this solid solution field, several ordering reactions occur [11].

The ordered phases are based on the B2 (Figure 2.2) and DO_3 structures (Figure 2.3). The B2 ordered structure consists of two simple interpenetrating cubic lattices with the atoms of each at the body centers of the other. In other words, it consists of a bcc arrangement with iron atoms at the body corners and aluminum atoms at the body centers (or vice versa). The B2 phase, at room temperature exists from 36 at.% to 50 at.% aluminum. Fully ordered B2 can only occur at 50 at.% aluminum. Alloys containing between 24 to 32 at.% aluminum exhibit homogenous DO_3 long range order. The DO_3 ordered structure is also a bcc type of atomic arrangement of eight cells but with iron atoms replacing the aluminum atoms at the body centers of every other alternate cell. This gives the Fe_3Al stoichiometry. The critical order-disorder temperature for DO_3 long-range order is about 550°C while B2 order persists to the melting point [11].

Fe-Al Phase Diagram

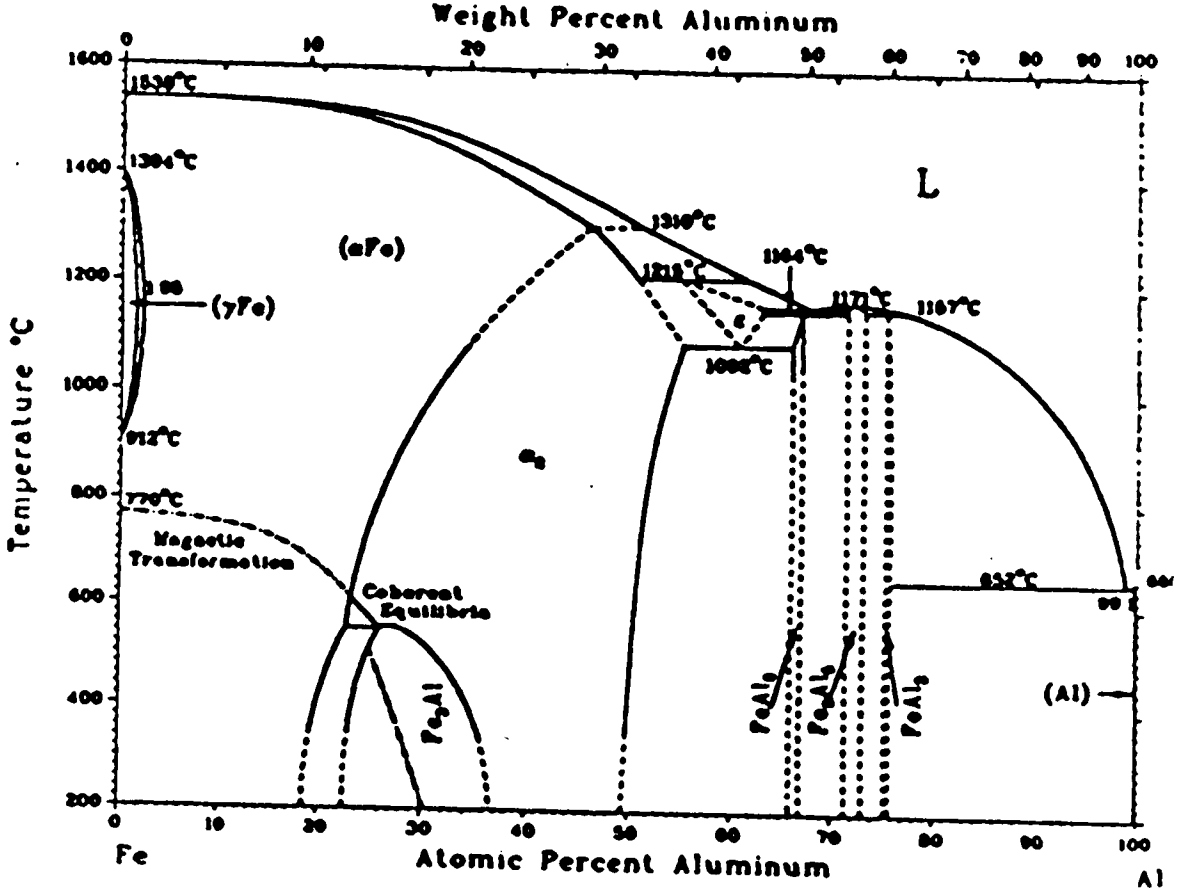

Figure 2.1 The Fe-Al phase diagram

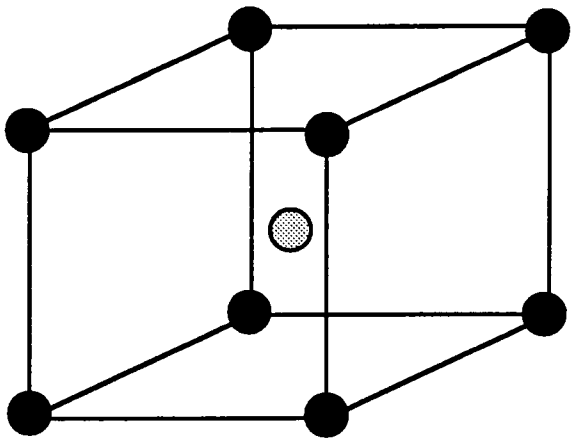

Figure 2.2 The AB unit cell with B2 structure

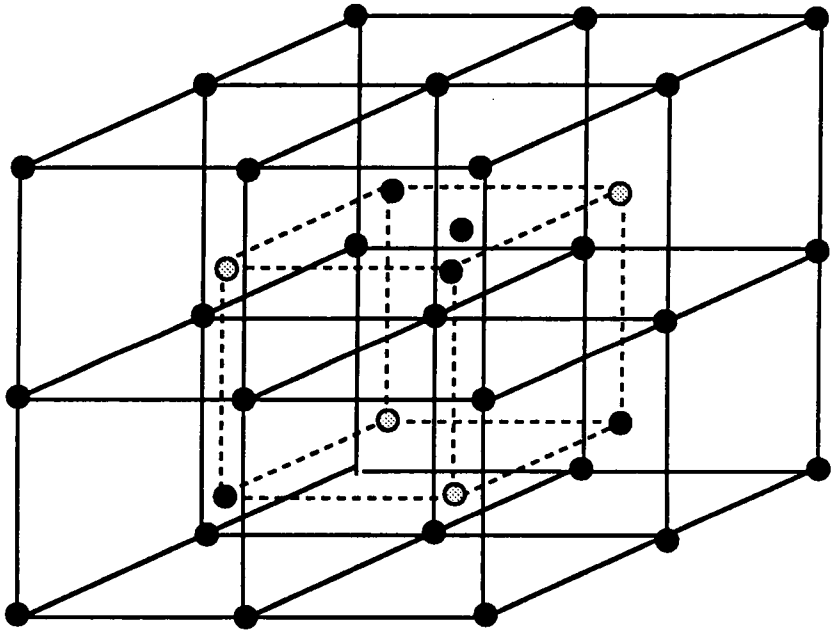

Figure 2.3 The A_3B unit cell with DO_3 structure.
A = ● B= ◎

2.4 Mechanical behaviour

1) The yield strength of FeAl is approximately independent of temperature at low temperatures but decreases rapidly at higher temperatures (above 500 K for the near-stoichiometric alloy and above 800 K for the iron-rich alloy), and

2) Ductility increases with increasing temperature, but at 1000 K in air a ductility minimum occurs [3].

Furthermore, it has also been seen that the yield strength decreases with increasing deviation from stoichiometry at low temperatures but increases with increasing deviation from stoichiometry at high temperatures. A brittle-to-ductile transition is observed around 700 K decreasing with decreasing grain size. It was confirmed that a change in slip vector from <111> to <100> occurs with increasing temperature and that the temperature of this transition increases with increasing deviation from stoichiometry [3]. FeAl, like many other intermetallic alloys suffers from severe room temperature brittleness . This brittleness results, even though the observed <111>{110} slip should provide enough slip systems to satisfy von-Mises criterion [6]. Two possible explanations are suggested for the brittleness of these intermetallic alloys. Weak grain boundaries may fail before sufficient slip systems can be activated, or limited cross slip may result in stress concentrations from dislocation pile-ups at grain boundaries, and result in brittle failure along grain boundaries [13].

The change from a <111> to a <100> slip vector at high temperatures means a reduction from five to only three independent slip systems [10] which are insufficient for uniform plastic flow in a polycrystalline metal [26]. It might be expected that the occurence of only <100> slip would lead to a sudden drop to almost zero plastic elongation. However, according to Schulson [27], the fine grain size in these alloys may be below the critical grain size for the brittle to ductile transition and would allow ductility because of stable microcracking. The critical grain size would

decrease with increasing temperature which would make the material more ductile because of stable microcracking at higher temperatures [27]. The ductility drop at 1000 K appears to be due to the onset of creep cavitation which occurs on boundaries which are at large angles to the tensile axis [3]. The fracture modes with increasing temperature are :

1) Transgranular cleavage to intergranular fracture for the iron-rich alloy.

2) Intergranular to dimple-like transgranular (at 800 K) to again intergranular failure for the near stoichiometric alloy [3].

2.5 Alloying the B2 FeAl with a third element

Since the binary FeAl exists over a range of compositions and possesses solubility for third element additions, it offers the potential of producing an acceptable ductility by alloying. That is, third element additions may be able to induce room temperature ductility or to increase elevated temperature strength whichever is more critical for a particular application [30].

Titran, Vedula and Anderson [30] found that materials produced by alloying FeAl with 5 at. % of a ternary element can be classified in three broad categories based on the extent to which the 5 at. % ternary element dissolves. The Class I FeAlX alloys are single phase materials after homogenization and include the elements Ni, Co, Ti, Si, Mn and Cr. The Class II alloys show incomplete solubility even after extensive homogenization while the Class III alloys consist of elements which do not exhibit any significant solubility.

Titran, Vedula and Anderson found that the Class I Alloys containing additions of 1 to 5 at. % Cr, Ti, Mn, Fe and Co all exhibit higher flow stress than a comparable FeAl binary and show solid solution strengthening. However, the most remarkable strengthening effect was observed by the addition of 0.8 at.% boron.

Titran et al attribute this to grain boundary strengthening. They also found that Class II and Class III alloys in general exhibited much higher flow stress than Class I compounds. This is due to precipitation of the second phase [30]. It may be noted that Munroe and Baker [21] observed solid-solution softening with the addition of up to 6 at.%. chromium. This is supported by other workers as well.

2.6 Fe-Al-Cr alloys

In a study at ORNL of DO_3-structured Fe+28at.%Al+Cr alloys, where the chromium concentration varied from 0-6 at. %, it was demonstrated that the chromium additions enhanced the ductility and slightly decreased the yield strength. It was also shown that the chromium additions decreased the anti-phase boundary (APB) energy of the <111> dislocations, which made cross-slip easier [17].

In another study of B2-structured iron-rich FeAl alloys conducted by Munroe and Baker [21] , it was shown that gliding <111>{110} dislocations interact during deformation to form <001> edge dislocations. The energetic driving force for the formation of these <001> dislocations is the removal of the {110} APB energy. It was suggested that these <001> dislocations may be the cause of transgranular cleavage in FeAl alloys.

Munroe and Baker [21] studied the effect on the {110} APB energy by the addition of 5-10 at. % chromium to the Fe-40Al alloy. The idea was that in reducing the APB energy, the density of <001> dislocations would be reduced and hence the ductility may be increased. A maximum of 6 at. % chromium was observed in solution in the $FeAl_{40}Cr_{10}$ alloy, which suggests that this is the solubility limit of chromium in $FeAl_{40}$. The as-cast hardness of chromium-containing alloys was considerably lower than that observed in both iron-rich and stoichiometric FeAl, which suggests that fewer vacancies are retained following high-temperature treatment of the

chromium-containing alloys. However, following vacancy removing anneals, the hardness of the chromium-containing alloys was still slightly lower than that of the binary alloy, indicating that chromium produces solute softening in FeAl [21].

Munroe and Baker [21] performed ALCHEMI (electron channeling to be described later) tests on the ternary alloys and found that Cr had a preference for the Al site. A ductility test indicated that the chromium-containing alloys had a similar ductility to unalloyed Fe-40Al, but were more ductile than Fe-45Al. In contrast, for the DO_3 alloys McKamey had demonstrated that a 2 at.% addition of chromium increased the room temperature tensile elongation of Fe-28Al from 2% to 9%. In that instance, it was demonstrated that the APB energy had been reduced, making cross-slip easier [17].

In the work of Munroe and Baker, the <111> dislocation partial spacing in the Fe-40Al+Cr alloys could not be measured, which they interpreted as suggesting that chromium additions had little effect in reducing APB energy. Chromium additions to FeAl may be expected to reduce APB energy by producing changes in bonding energy. However, Munroe and Baker argue that the presence of chromium on the aluminum sublattice will reduce the number of iron anti-site defects and so increase APB energy. Hence, they suggest that no significant improvement in ductility is obtained on addition of chromium to Fe-40Al [21].

2.7 Ternary element site occupation

As seen from the literature review on Fe-Al-Cr alloys, the mechanical properties are influenced by the addition of a ternary element. The correlation between the site preference of the ternary element. It is not known if there is a correlation between the site preference of ternary elements with mechanical properties. Knowledge

of the site preference of various elements may help us to understand and optimize the mechanical properties.

2.8 Methods of determining site substitution

1) Direction of solubility lobe

2) Statistical mechanics and thermodynamics

3) Atom probe field ion microscopy

4) ALCHEMI

5) X-ray and neutron diffraction

2.8.1 Direction of solubility lobe

This method is based on the idea [23] that the site occupation of a ternary addition (X) can be inferred from the direction of the solubility lobe in the corresponding ternary phase diagram (Figure 2.4). If the solubility lobe of the alloy AB extends in the direction from AB to XB (direction a), then the ternary element X will preferentially occupy the sites occupied by atom A. On the other hand, if the solubility lobe direction is from AB to AX (direction b), the ternary element X will occupy the sites occupied by atom B. Finally, for the solubility lobe in the direction bisecting the 'a and b directions', the ternary element will occupy both the sites.

With few exceptions, Ochiai et al found good agreement [23] of site occupancies determined by this method with those obtained from x-ray data. However, a practical limitation in implementing the solubility lobe method is that the solubility of most additions is too small for the direction of the solubility lobe to be resolved. This method is unsuitable for those alloys which show solubility for third element over a range of composition, i.e., where the solubility lobe is poorly defined, and where the

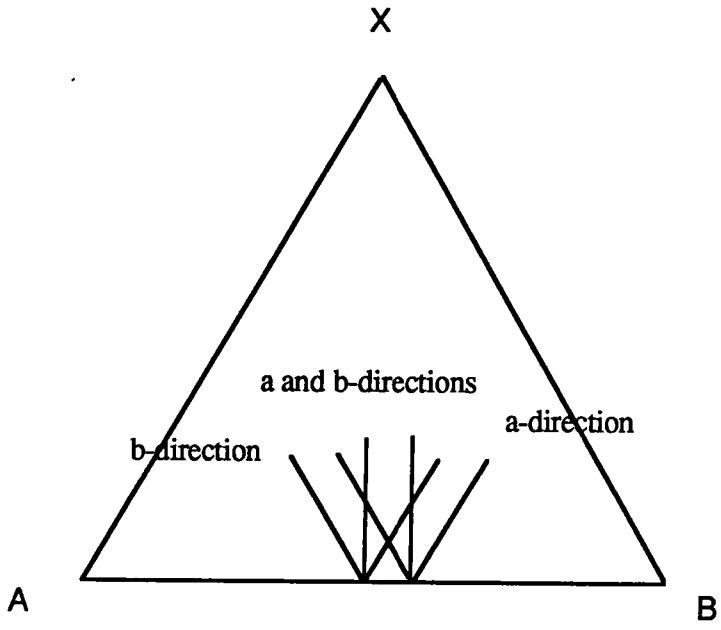

Figure 2.4 : Solubility lobe method for the determination of site occupancies.

X substitutes for A along a-direction, for B along b-direction and substitutes equally for A and B along the a and b-directions.

site preference of the ternary addition changes with the composition of the base alloy [33].

2.8.2 Statistical mechanics and thermodynamics

In the course of his work on solubility lobes, Ochiai has also shown that the site occupation of the ternary element can be predicted from thermodynamic considerations. The theoretical model that he constructed considers only nearest-neighbor interactions because he argues that the second and distant neighbor interaction energies are likely to be almost zero [23].

In this model, the total bond energy H, is expressed as

$H = N_{AA} H_{AA} + N_{BB} H_{BB} + N_{CC} H_{CC} + N_{AB} H_{AB} + N_{AC} H_{AC} + N_{BC} H_{BC}$, where H_{AA} is the bond energy for A-A pairs and N_{AA} is the number of nearest neighbor pairs of type A-A, and similarly for the other atoms. To determine the site occupation of addition C, a stoichiometric composition is considered with : a) C atoms replacing A atoms at a-sites, b) C atoms replacing B atoms at b-site. The bond energies, H(a) and H(b) are expressed in terms of these two conditions [23]. The differentials of the values H(a) and H(b) with respect to the ternary addition X_C, are compared (i.e. $dH(a)/dX_C$ and $dH(b)/dX_C$ are compared). The lower value leads to an energetically favorable condition with the ternary element C preferring that site i.e., if $dH(a)/dX_C$ is lower than $dH(b)/dX_C$, then the ternary element C favors the a-site [23].

The values H_{AB} cannot be obtained from experiment as the experimental data is too limited to obtain the bonding energy. However, Miedema and co-workers have developed a method for the prediction of the heat of alloy formation (see Chapter 4 for a detailed mathematical application of this method for the B2 structure). The accuracy of this prediction has been successfull as shown by many investigators [19].

2.8.3 Atom Probe Field Ion Microscopy

In this method, the atomic composition of the material is analysed atomic layer by layer. The site occupation is determined directly by comparing the concentrations of the planes with that of the ordered crystal structure [20].

This type of analyses requires that the atom probe be capable of precisely analysing the composition of single atomic layers without any contribution from the adjacent layers. The determination of the composition of individual planes requires that atom probe analysis be taken along a direction perpendicular to the atomic planes, ie. along a pole [20]. The selection of the plane on which to perform the analysis is based on two main considerations:

1) To choose a plane with the largest composition difference in successive layers, ideally pure A versus pure B, and

2) To collect the maximum number of atoms per layer to obtain the optimum statistics. In this method, care has to be taken to select experimental conditions [20] such as to ensure uniform evaporation of all elements without any preferential evaporation or retention.

2.8.4 ALCHEMI

Atom Location by Channelling Enhanced Microanalysis (ALCHEMI) is a quantitative technique for identifying the crystallographic sites, distribution and types of substitutional impurities in many crystals. The method uses the incident electron beam channeling orientation dependance of characteristic x-ray emission and uses an energy dispersive Si(Li) x-ray detector fitted to a transmission electron microscope [29].

For arbitrary orientations of the crystal with respect to the electron beam, all atomic species in a crystalline plane experience an equal flux of electrons,

averaged through the crystal thickness. However, for orientations at or near strong diffraction conditions, the phenomenon of electron channelling results in standing waves which peak at different sites in the unit cell, and which move as the orientation is varied. Thus the emission of characteristic flourescent x-rays - and the corresponding electron energy losses from the different atomic species can vary dramatically. This phenomenon is the basis of the ALCHEMI technique for the location of the species on the atomic sites in the crystal structure [30].

For materials where low energy flourescent x-rays (< 3 keV) must be used because of constituents with low Atomic Number (Z), ionization delocalization is often an important limiting factor. In minerals and ceramics with large unit cells as in spinel, the interplanar spacings (d) are large enough to mask delocalization effects; consequently reliable results can still be obtained. In intermetallics, the d-spacings generally are much smaller and gross corrections for the effects of ionization delocalization on the low - Z components are necessary to obtain even a qualititative indication of site occupancies [4].

2.8.5 X-ray and neutron diffraction

The relative integrated intensities of diffracted x-ray peaks from powder diffractometry are given by :

$$I = |F|^2 p ((1 + \cos^2 2\theta)/\sin^2 \theta \cos \theta) \exp(-2M)$$

where F is the structure factor for the unit cell,

p is the multiplicity factor for the hkl indices,

θ is the Bragg angle,

$(1 + \cos 2\theta)/\sin \theta \cos \theta$ is the Lorentz-polarization factor,

$\exp(-2M)$ is the temperature factor where

$M = B (\sin \theta/\lambda)^2$ where λ =wavelength in Å and

$B = 8\pi^2 \langle\mu^2\rangle$, where $\langle\mu^2\rangle$ is the mean square atomic displacement.

The structure factor F for the unit cell is defined in terms of the atomic scattering factor as :

$F_{hkl} = \sum f\, e^{2\pi i\,(hu + kv + lw)}$

where f is the atomic scattering factor for an atom,

h, k, l refer to the Miller Indices of the plane, and

u, v, w refer to the atom co-ordinates in the x, y, z directions respectively.

We make use of the relationship $e^{in\pi} = (-1)^n$ to determine the structure factor F, for a bcc binary solid solution (AB) with [7] complete disorder and complete order.

1. Complete disorder

In this case we may consider the unit cell to have two average A-B atoms, one at the cell corner and one at the cell center. The co-ordinates of these atoms are at (0 0 0) and (1/2 1/2 1/2) respectively. The structure factor is given by :

$F = f_{ave}\,[\,1 + e^{\pi i\,(h+k+l)}]$,

$F = 2f_{av} = (f_A + f_B)$, for h+k+l = even,

$F = 0$. for h+k+l = odd.

2. Complete order

In this case we may consider the unit cell to have an A atom at the cell corner (0 0 0) and a B atom at the cell center (1/2 1/2 1/2). The structure factor is given by :

$F = f_A + f_B\, e^{\pi i\,(h+k+l)}$,

$F_f = f_A + f_B$, for h+k+l = even,

$F_s = f_A - f_B$, for h+k+l = odd.

The ordered alloy thus produces diffraction lines for all values of h+k+l = even or odd and its diffraction pattern therefore resembles that of a simple cubic substance. The diffraction lines from planes where h+k+l is even are called fundamental lines, since they occur at the same positions and with the same intensities in the patterns of both ordered and disordered alloys. The extra lines which appear in the pattern of an ordered alloy, arising from the planes where h+k+l is odd, are called superlattice lines, and their presence is direct evidence that ordering has taken place.

Not all ordered alloys are fully ordered. This departure from perfect order is described by means of the long-range order parameter S, defined as :

$S = (r_A - C_A)/(1 - C_A)$, where r_A = fraction of A sites occupied by the 'right' atoms, i.e., A atoms, C_A = atom fraction of A atoms in the alloy. When the long-range order is perfect, r_A =1 and therefore S = 1. When the atomic arrangement is completely random, $r_A = C_A$ and S = 0. Any departure from perfect long-range order causes the superlattice lines to become weaker. The structure factors of a partially ordered B2 alloy are given by :

$F = f_A + f_B$, for h+k+l = even,

$F = S(f_A - f_B)$, for h+k+l = odd.

On comparision of these equations with those for the fully ordered alloy, we note that only the superlattice lines are affected. But the effect is a strong one, because the intensity of a superlattice line is proportional to $|F|^2$ and therefore to S^2.

In the case of the B2 alloys, adding a ternary element increases or decreases F_f depending on the value of the atomic scattering factor relative to the atomic scattering factors of the base elements, independently of where the ternary element sits.

However, the superlattice peak intensity Fs is strongly affected both by the atomic scattering factor and by the site occupancy of the ternary element.

The intensity of a superlattice line from an ordered solid solution is proportional to the square of the difference in atomic scattering factors and therefore much lower than that of a fundamental line. Sometimes it can it be so low that it cannot be detected. We take the case of the fully ordered CuZn and ignore the variation in multiplicity factor and Lorentz-polarization factor from line to line to obtain the ratio of the intensities of the superlattice and fundamental lines as :

$I_s/I_f \sim (f_{Cu} - f_{Zn})/(f_{Cu} + f_{Zn}) \sim (29 - 30)^2/(29 + 30)^2 \sim 0.0003$. This ratio is so low that a x-ray powder pattern of this alloy, ordered or disordered, ordinarily appears to be that of a body-centered cubic substance. The same is true of any superlattice of elements A and B which differ in atomic number by only one or two because the superlattice-line intensity is generally proportional to $(f_A - f_B)^2$.

There is one way, however, of increasing the intensity of a superlattice line, when the two atoms involved have almost the same atomic numbers. This can be done by the proper choice of the incident wavelength. At constant $\sin(\theta/\lambda)$, the atomic scattering factor of an element is independent of the wavelength of the scattered radiation as long as the incident wavelength λ, is not near any absorption edge of the scattering element. When the incident wavelength λ, is nearly equal to the wavelength λ_k, of the K absorption edge of the scattering element, then the atomic scattering factor of that element may be several units lower than it is when λ is much shorter than λ_k. This change in f is due to the anomalous dispersion. Physically, it can be regarded as a resonance effect in which the oscillations of the K electrons, which contribute to the scattering, are disturbed when the incident radiation has a frequency near that at which K electrons can be actually ejected from the atom. If we put f_0 as the frequency independent atomic scattering for $\lambda << \lambda_k$, and Δf as the change in f_0 when λ is near

λ_k, then the quantity $f = f0 + \Delta f$ gives the value of the atomic scattering factor when λ is near λ_k. Δf has a real and an imaginary part and is expressed as $\Delta f = f' + if''$ where f' is the real part and f'' is the imaginary part. Figure 2.5 shows the variation of f', the real part with λ/λ_k. To a very good approximation, the change in atomic scattering factor, f' is independent of scattering angle and therefore a constant for all lines on the diffraction pattern [7].

Site occupation in binary alloys with two sublattices can be determined by conventional diffraction techniques using a single energy when there is high contrast between atoms. However, in a ternary alloy with two sublattices, there are two unknowns thus requiring two diffraction measurements rather than a single diffraction experiment. In principle, one chooses x-ray wavelengths to maximize the contrast between the elements. Anomalous x-ray scattering provides a technique in which diffraction experiments are performed near the absorption edges of the constituent elements in a multielement system to produce increased contrast through changes in the atomic scattering factor [14].

2.9 Rietveld method of least-squares

In this work we have used the GSAS (Generalized Structure and Analysis Systems) software for analysis of the data. This software uses the Rietveld method of least squares for refinement of the experimental data. For any experimental data, the most satisfactory set of parameters are the ones that make the sum of the squares of the errors a minimum. This is the basis of the least-squares method. The traditional approach to the refinement of powder data has been to reduce the pattern to a set of integrated intensities, i.e., line data, and then to $\sum F_k^2$ values, F_k being the customary structure factor and the $\sum$ denoting a summation for overlapping reflections [1]. In the Rietveld profile refinement program, instead of using line data, the

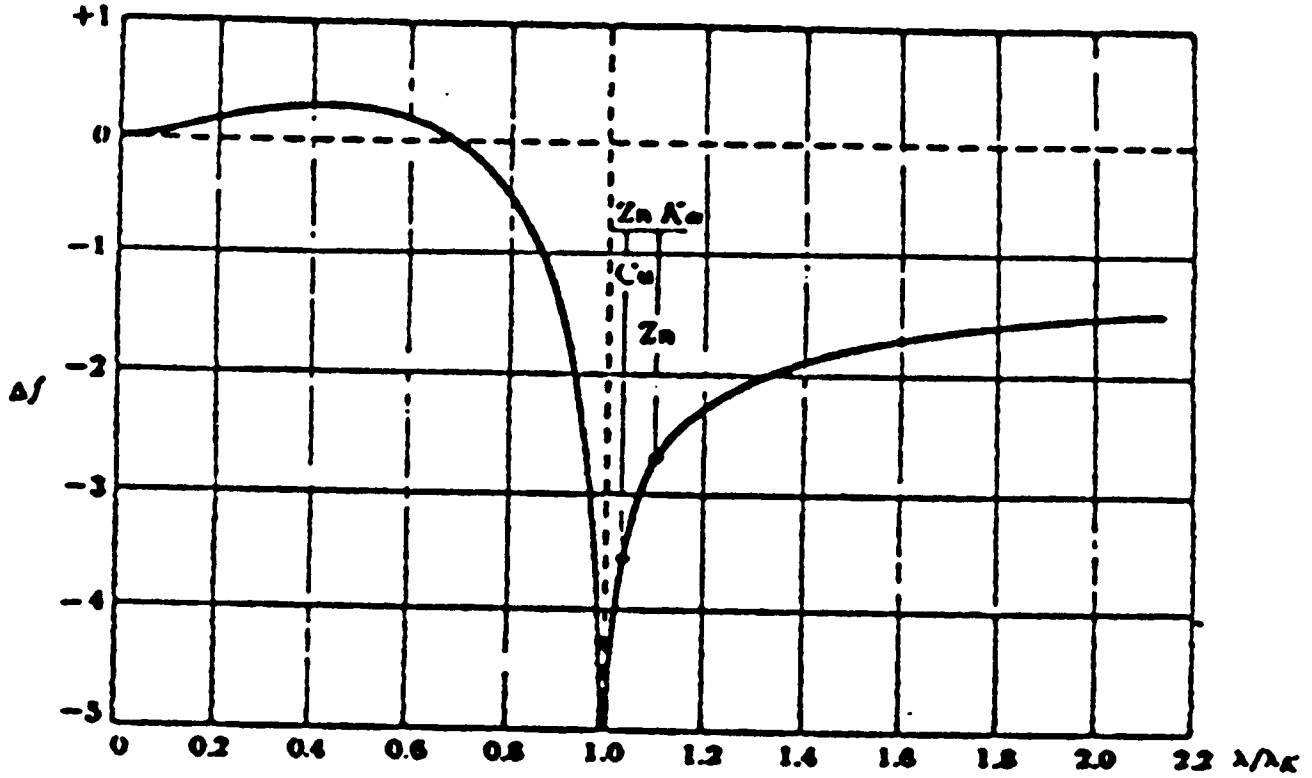

Figure 2.5 Variation of f' with λ/λ_k

structural parameters are fitted to the overall profile of the powder pattern. The assumption is that the pattern is the sum of a number of Gaussian-shaped Bragg reflections centered at their respective Bragg angle positions with much overlapping. Least-squares refinement is achieved by minimizing the function $M = \sum w_i[y_i(obs) - y_i(calc)/c]^2$, where the summation is over all points in the pattern. $y_i(obs)$ and $y_i(calc)$ are the observed and calculated intensities respectively of the diffraction pattern at position i. The weighting factor w_i, is inversely proportional to the variance of the quantity in square brackets and c is an overall scale factor [1].

Peak shape

A Gaussian peak shape for each Bragg peak is assumed and its contribution to the measured profile y_i at position $2\theta_1$ can be written as

$$y_i = \frac{t F_k^2 j_k L_k 2 (\sqrt{\ln 2}) \exp[-4 \ln 2\{(2\theta_1 - 2\theta_k)/H_k\}^2]}{H_k\sqrt{\pi}}$$

where

t = the step width of the counter,

F_k^2 is the intensity of the Bragg reflections,

j_k = the multiplicity of the reflection,

L_k = the Lorentz factor,

$2\theta_k$ = the calculated position of the Bragg peak corrected for the zero-point shift of the counter,

H_k = the full width at half height.

We put $I_k = \frac{t F_{k2} j_k L_k 2 \sqrt{\ln 2}}{H_k \sqrt{\pi}}$ and $b_k = \frac{4\ln 2}{H_{k2}}$,

to simplify the profile equation to $y_i = I_k \exp[-b_k (2\theta_i - 2\theta_k)_2]$.

At very low scattering angles, however, the peaks begin to show a

pronounced asymmetry. This is mainly because of the use of finite x-ray diffractometer slit heights. This vertical divergence effect [1] causes the maximum of the peak to shift to lower angles, but does not affect the integrated peak area. Introduction of a semi-empirical correction factor in the equation gives a good approximation to the asymmetric peak profile :

$$y_i = I_k \exp[-b_k (2\theta_i - 2\theta_k)2] \{1 - P(2\theta_i - 2\theta_k)2\, s/ \tan \theta_k\}, \qquad (24)$$

where P is the asymmetry parameter and s = +1, 0, -1 depending on the difference $2\theta_i - 2\theta_k$ being positive, zero, or negative, respectively. As can be seen, this correction has two main effects : the peak is shifted to lower angles and the Gaussian peak shape is made slightly asymmetric [1].

Least-squares parameters

The least-squares parameters can be divided into two main groups. The first group, the profile parameters, define the positions, the halfwidths, and the possible asymmetry of the diffraction peaks. The second group, the structure parameters, define the contents of the asymmetric unit cell such as the overall scale factor, the overall isotropic temperature parameter and the fractional coordinates of the atoms in the asymmetric unit [32].

Chapter 3

Experimental work

3.1 Selection of specimen composition

The specimen compositions were intended to be in the single phase B2 region. As shown in the iron-aluminum phase diagram (Figure 2.1), this is between 36-50 at.% aluminum. According to Munroe and Baker [21], chromium is soluble in Fe-40Al up to a limit of 6 at.%. Titran, Vidula and Anderson [30] working on Fe-40Al and Fe-45Al found complete solubility with addition of 5 at.% chromium.

Seven compositions were chosen for this work. Four of these had chromium as a ternary addition while the balance three were binary iron-aluminum alloys. The compositions chosen are given in Table 3.1. All specimens were later verified for single phase by microstructure examination and x-ray diffraction.

3.2 Specimen preparation

The samples were prepared as 15 g buttons by argon-arc casting the constituent pellets at a pressure of 50 x 10^{-3} Torr to minimize oxidation. The chromium pellets were placed at the bottom to minimize oxidation of chromium. Each button was flipped over and remelted five times to ensure macroscopic homogeneity.

The specimens were then given a homogenization treatment at 1000°C for 7 days. The vacuum maintained in the furnace was of the order of 3 x 10^{-6} Torr.

3.2.1 Preparation of powders for diffraction runs

These specimens were then ground into fine powder with the help of a diamond grinding wheel. About 0.8 g of powder was ground for each specimen. The

TABLE 3.1 : Specimen compositions and the corresponding numbers

Composition	Specimen number
$Fe_{51}Al_{49}$	51
$Fe_{55}Al_{45}$	55
$Fe_{55}Al_{40}Cr_5$	55C
$Fe_{57.5}Al_{37.5}Cr_5$	57C
$Fe_{59}Al_{36}Cr_5$	59C
$Fe_{60}Al_{40}$	60
$Fe_{60}Al_{35}Cr_5$	60C

powders obtained were passed through a series of sieves (325, 450 and 635 mesh). The coarse powders that did not pass through the 325 mesh were discarded.

The percentage of powders that passed through the various sieves was roughly the same for each sample.

Passed through	Percent
325	10
450	45
635	45

As the iron-aluminum powders were brittle and could not be pressed into a briquette that would hold together on handling, it was necessary to mount them in a specimen holder. Seven square nickel plates 2.7 cm on a side were cut from a nickel plate of thickness 1.5 mm. A circular hole of diameter 1.6 cm was punched into each plate and the circular plug retained. Two more holes of diameter 3 mm were drilled at diametrically opposite ends of the plates. The distance between these two holes was maintained at 2.4 cm (Figure 3.1). The size and positioning of the holes was chosen so as to securely fit the nickel holders on the rotation stage for powder diffraction on the synchrotron source.

With the circular plug placed below but centered in the plate cavity, the powder was placed in the cavity and compacted against a polished tungsten carbide block at a pressure of 105 MPa [Figure 3.2]. The specimen powder was so placed that the finest powders (that had passed the 635 mesh) were furthest away from the plug and formed the surface on which the x-ray beam would strike. This was done to reduce the roughness correction and to minimize preferred orientation.

To relieve the stress caused by grinding the iron-aluminum powders, and to fully order the alloys to equilibrium, these pressed powders were heat treated at

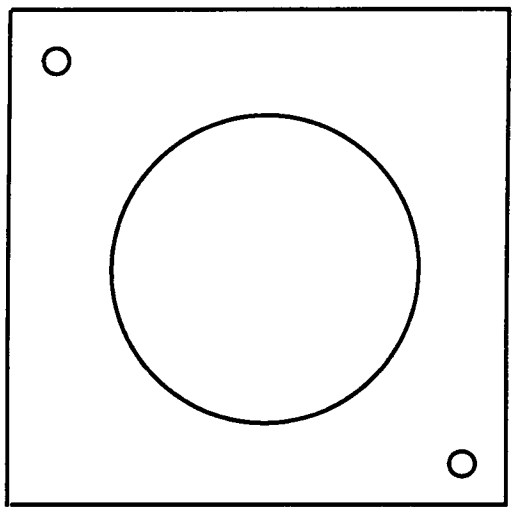

Figure 3.1 Specimen holder

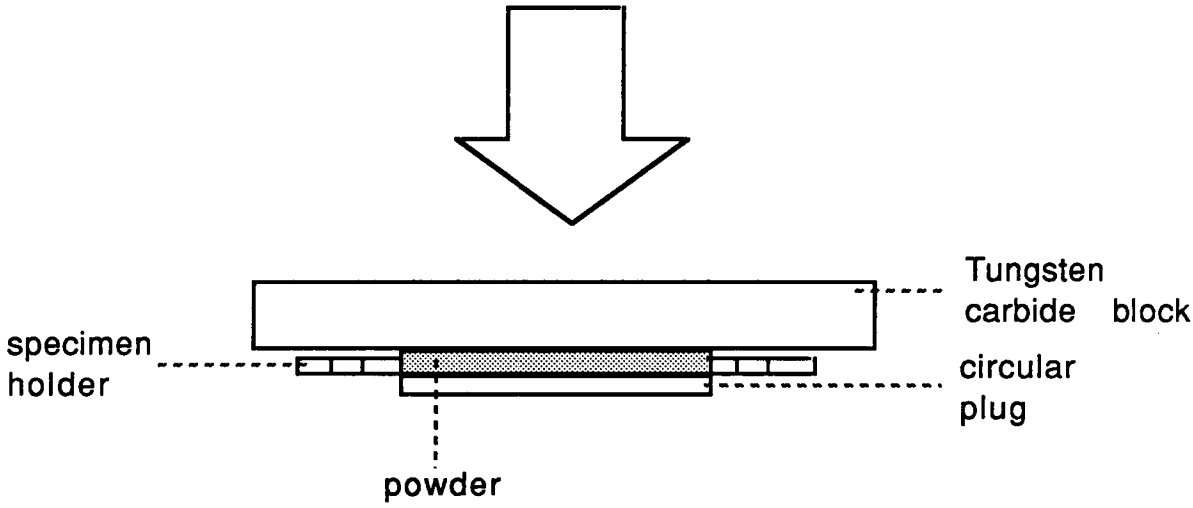

Figure 3.2 Compacting powder specimen into specimen holder

800°C for 3 hours followed by 400°C for 5 days. This closely resembles the proceedure of Nagpal and Baker [22] who suggest a heat treatment of 660°C for 3 hours followed by 400°C for 5 days. As these powder compacts are friable, they were alternatively stacked in layers of the nickel holders containing the powders and the nickel plates and then tightly wrapped in tantalum foil, prior to heat treatment. This was then encapsulated in a quartz tube at a pressure of 3×10^{-6} Torr.

The quartz tube was placed in an air furnace at 800°C for 3 hours followed by 400°C for 5 days. The powder specimens being somewhat sintered were easier to handle and ready for diffraction runs. After these successive heat treatments, no weight loss was detected for the binary alloys but the chromium containing alloys showed a small weight loss. This entire weight loss was attributed to the oxidation of chromium. The resulting atomic compositions are given in Table 3.2. While we shall use the actual compositions for calculation of site occupancies, we shall, for the sake of convenience refer to the specimens by the attempted composition.

3.2.2 Specimen preparation for microstructure examination and microhardness testing

For microhardness testing, all alloys received a homogenizing treatment in vacuum at 1000°C for 7 days. Subsequently, two different types of heat treatment were given to these alloys. One lot was annealed at 1000°C in air for 1 hour and subsequently air cooled. The other lot was annealed at 400°C in air for 5 days and then air cooled. Another specimen $Fe_{51}Al_{46}Cr_3$ (sample 51C) was prepared and given this heat treatment. The specimens were then polished for microhardness testing. An etchant consisting of 70% H_20, 10% HNO_3, 15% CH_3COCH_3 and 5% HCl by volume was used to reveal the microstructure [25] of the alloys annealed at 400°C for 5 days.

TABLE 3.2 : Actual specimen compositions and the corresponding numbers

Composition	Specimen number
$Fe_{51}Al_{49}$	51
$Fe_{55}Al_{45}$	55
$Fe_{55.6}Al_{40}Cr_{4.6}$	55C
$Fe_{57.8}Al_{37.7}Cr_{4.5}$	57C
$Fe_{59.5}Al_{36.2}Cr_{4.3}$	59C
$Fe_{60}Al_{40}$	60
$Fe_{60.5}Al_{35.4}Cr_{4.1}$	60C

3.2.3 Specimen preparation for site occupation determination by the Atom Probe

One specimen was prepared ($Fe_{57.5}Al_{37.5}Cr_5$ - sample 57C) for analysis by the Atom Probe. A thin needle of the specimen with dimensions 11mm x 0.5mm x 0.5mm was fabricated from the button and given the same heat treatment as the powder specimen (1000°C for 7 days followed by 800°C for 3 hours and 400°C for 5 days in vaccum).

3.3 X-ray diffraction of powders

Diffraction runs of powder specimens on a Philips x-ray diffractometer at an energy of 8.04 keV (Cu K_α) were conducted over a range of Bragg angles, from $2\theta = 26^\circ$ to $2\theta = 110^\circ$ with a step size of 0.03° and a counting time of 4 seconds. Eight B2 phase Bragg reflections, four fundamental and four superlattice were observed in these diffraction patterns. Because of the presence of the nickel specimen holder, some Ni reflections were observed in the diffraction pattern. The Ni (111) fundamental reflection overlaps with the B2 (110) fundamental reflection (at ~ 44° 2θ). Therefore, diffraction patterns at this energy were analysed between $2\theta = 50^\circ$ to 110°.

The atomic scattering factors of iron, aluminum and chromium are given in Table 3.3. It can be seen that the values for iron and chromium differ by only 2. This makes it difficult to differentiate between the iron and chromium atoms with x-rays.

However, when diffraction is carried out at an energy close to an absorption edge, additional terms have to be added to the atomic scattering factor. These terms, as described earlier are due to the anomalous scattering close to the absorption edge, and include a real part f', and an imaginary coefficient f". The atomic scattering factor f is then given as $f = f_0 + f' + if''$ where f_0 is the atomic scattering factor far from a diffraction edge [2].

TABLE 3.3 : Atomic scattering factors (fo) of Fe, Al and Cr

Element	Atomic Scattering Factor (f0 value) at sin $\theta/\lambda = 0$
Fe	26
Al	13
Cr	24

For the case of the Cu K_α x-rays, the anomalous scattering terms are not significant enough to differentiate between iron and chromium. Therefore, the variable wavelength beam at the National Synchrotron Light Source (NSLS) at Brookhaven National Laboratory (BNL) was used to select x-ray wavelengths to highlight the contrast between the elements.

Diffraction runs at two x-ray energies were conducted at the NSLS facility. All specimens except specimen 59C were run at these two energies. The runs were at :

1. 15 eV below the chromium K edge - i.e. at 5.974 keV. The run was conducted between the scattering angles, $2\theta=35^\circ$ to $2\theta=130^\circ$ with a step size of 0.02°. Only the chromium-containing alloys and one of the binary alloys, the $Fe_{60}Al_{40}$ were run at this energy. Six Bragg peaks were observed in the diffraction pattern within this range, and
2. 15 eV below the iron K edge - i.e. at 7.097 keV. The run was conducted between the scattering angles, $2\theta=28^\circ$ to $2\theta=155^\circ$ with a step size of 0.02°. Nine Bragg peaks were observed in the diffraction pattern within this range.

The anomalous dispersion corrections at these energies are given in Table 3.4. These values are calculated from tables given by Kromer and Liberman [15].

In addition, the fluorescent intensity of Fe K_α radiation was measured from the same specimens excited with an x-ray energy of 8.3 keV which is above the K edges of both Fe and Cr. This measurement was made to determine the effect of sample granularity on the intensity of the diffracted x-ray pattern. Reductions in flourescent x-ray intensity are attributed to an internal porosity which is independent of 2θ and a surface porosity which is 2θ dependent. A correction to powder diffraction data requires a suitable experimental determination of this granularity or microroughness effect. Figure 3.3 shows the changes in flourescent intensity with scattering angles from the specimens. The sharp lines occur when the 2θ value of

TABLE 3.4 : Anomalous scattering factors of Fe, Al and Cr at Cu K_α, near the Fe edge and Cr edge

Atom	Cu Kα		Fe-edge		Cr-edge	
	f'	f''	f'	f''	f'	f''
	E =8.04keV		E = 7.097 keV		E = 5.974 keV	
Fe	-1.192	3.202	-5.760	0.545	-1.688	0.640
Al	0.203	0.246	0.239	0.313	0.288	0.434
Cr	-0.207	2.448	-0.811	2.997	-5.950	0.593

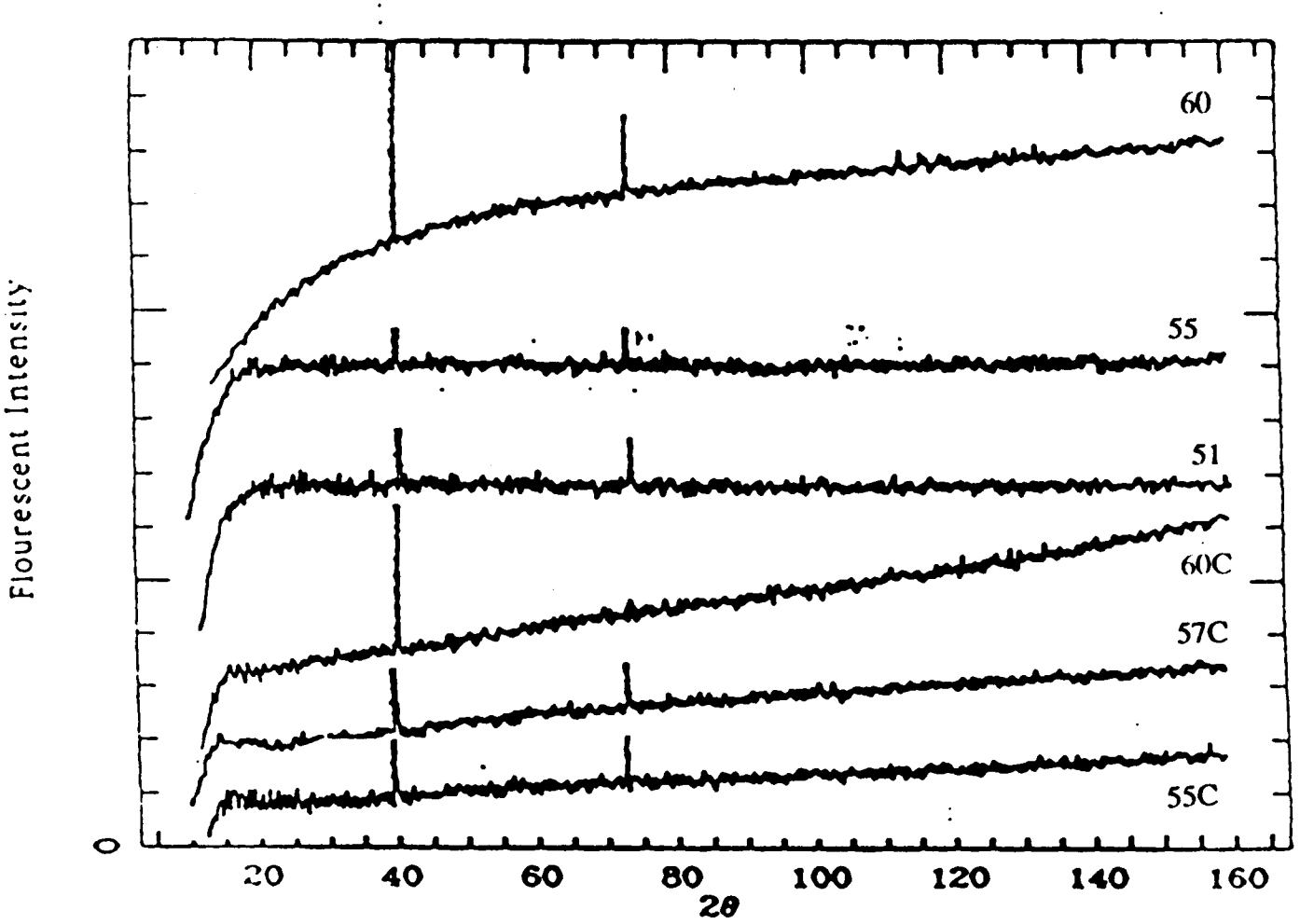

Figure 3.3 **Variation of flourescent intensity with scattering angle**

measurement is close to a Bragg reflection. As the angle of the incident radiation equals the angle of the emerging radiation the flourescent intensity should either be a constant (for no granularity effect) or a function of 2θ [28]. The powder data were corrected by the slope of the flourescent intensity to remove the decrease in diffracted intensity with lower 2θ values.

3.4 Data correction

Before the data was refined and analysed by the General Structure and Analysis Systems (GSAS) software based on the Rietveld method of least-squares it was necessary to incorporate a dead-time correction to the count rate and then the granularity correction.

Dead-time correction

The variable x-ray counting rate in the diffraction patterns were corrected for dead-time in the detector and electronics by the equation $I_{true} = I_{obs.} \exp(\tau I_{true})$ where I_{obs} and I_{true} are the observed and the dead-time corrected intensities respectively, and τ is the dead-time. At NSLS, τ was measured by varying the intensity of the primary beam and measuring the count rate in a nitrogen filled ion chamber (I_{true}) with no dead-time and simultaneously in the proportional counter (I_{obs}) used for detecting the diffracted x-rays. For the CuK_α diffraction pattern, τ was measured by changing the x-ray tube current in known amounts with the assumption that the x-ray flux is directly proportional to the tube current.

Values of τ obtained in these ways from BNL and ORNL are given in Table 3.5.

TABLE 3.5 : Detector deadtime at the Cu K_α, Fe edge and Cr edge energies

Energy	τ(μseconds)
Cu K_α	12.0
Fe edge	3.22
Cr edge	2.68

Granularity correction

The Fe Kα flourescence data at 8.3 keV was extrapolated to a value of one at $2\theta=180^{o}$ for each specimen. The entire data was then divided by a suitable equation (function of 2θ) to bring it to a value of one. This was done by fitting a curve of the form : $I_{corr} = I_{obs}/[1-A(180 -2\theta)]$, where I_{obs} and I_{corr} represent the observed and granularity-corrected intensities respectively, and A is a measure of the Fe Kα flourescence as a function of 2θ which reflects the reduction in the diffracted intensity due to the granularity within the specimen. The values of A so obtained are given in Table 3.6.

The data uncorrected for granularity would be expected to give incorrect (low and possibly negative) values of the thermal parameters for the atoms [28]. Both corrected and uncorrected data were processed with the GSAS program to determine the sensitivity of the thermal parameters and site occupations to the granularity corrections and errors in the thermal parameters.

Two sets of data, one corrected for both dead-time and granularity, and the other corrected only for dead-time were analysed by GSAS. After refining the peak positions with zero correction and lattice parameter, the peak profiles were fitted with a Gaussian-Lorentzian function based on Simpsons pseudovoigt method of integration [12]. However, due to peak asymmetry and broadening of higher angle reflections, the function could only fit the low angle peaks well. The Lorentzian tails of the high-angle peaks could not be fitted well by the function (Figure 3.4).

3.5 Reconstructing the data

Much effort can be expended on trying to find peak shape fitting parameters without success. We know that the site occupation depends upon the integrated intensity and is independent of the peak profile since only one reflection and

TABLE 3.6 : Granularity correction for all the specimens

Sample no.	A
60	8.073×10^{-4}*
55	1.308×10^{-4}
51	1.506×10^{-4}
60C	1.738×10^{-3}
57C	5.302×10^{-4}
55C	4.326×10^{-4}

* between $2\theta = 60^{\circ}$ to 180°. For $2\theta = 10^{\circ}$ to 60°, $A' = 3 \times 10^{-3}$,
$I_{corr} = I_{obs}/[1-A'(92^{\circ} - 2\theta)]$

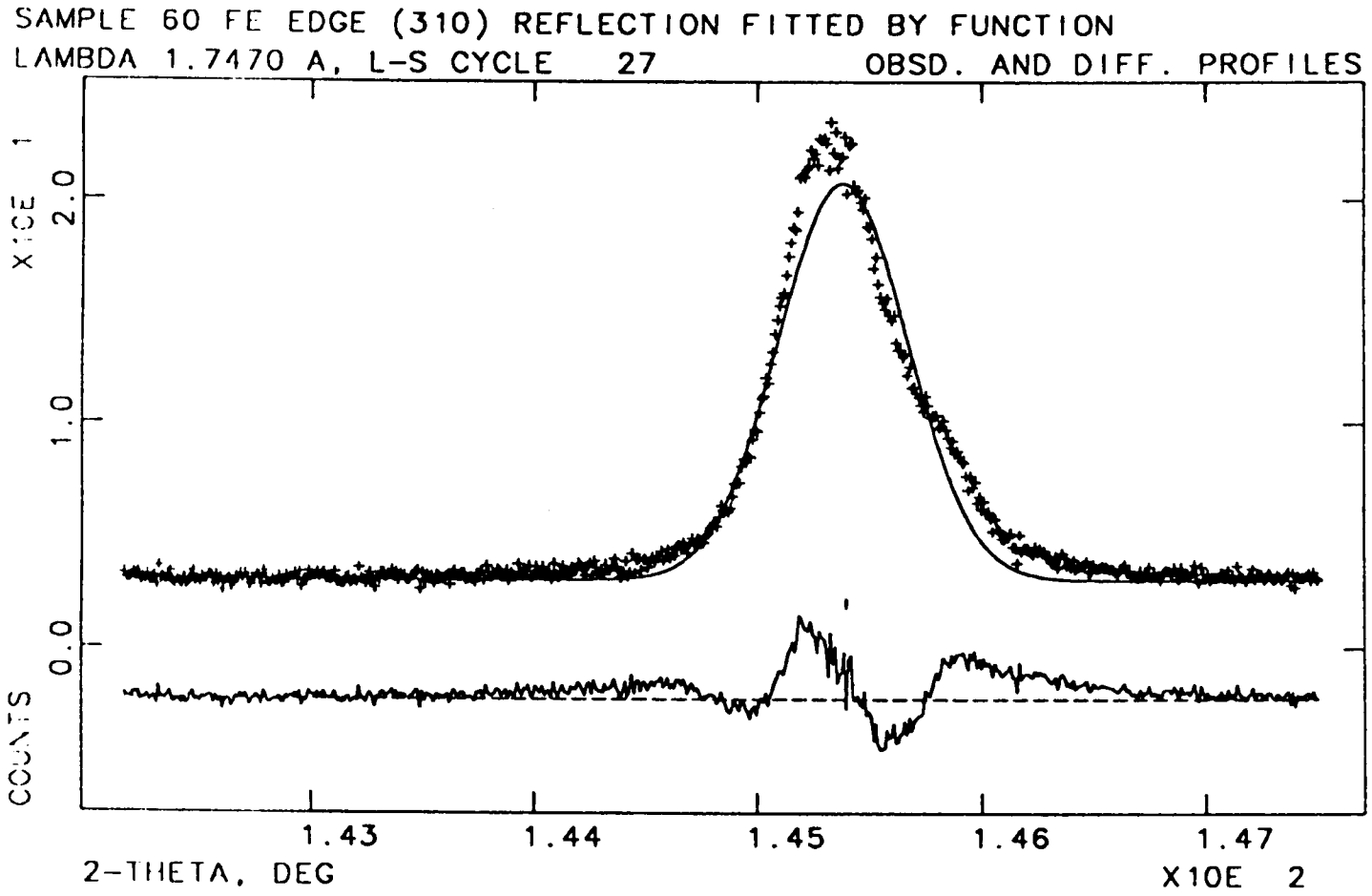

Figure 3.4 Rietveld fit to (310) reflection for $Fe_{60}Al_{40}$ near the Fe edge

no overlap is incurred in these powder patterns. Wetherefore integrated each reflection and then constructed Gaussian peak shapes having the same areas as the observed reflections. This is done by first finding the area of each peak with a program called Curvefit. A Gaussian curve of the same area is reconstructed at the appropriate Bragg angle. The entire diffraction pattern is therefore constructed in this manner with the background intensity set to zero. Again, two sets of data are constructed, one with the granularity correction and the other without the granularity correction.

3.6 Refinement of peak profiles

These reconstructed diffraction patterns are then analysed by GSAS. In the refinement, the peak profiles are first refined (now easily and precisely fitted) followed by the isotropic temperature factors and the site occupancy. The isotropic temperature factors are refined for the three elements while keeping their ratios inversely proportional to their atomic masses, i.e.,

$$B_{Fe} : B_{Cr} : B_{Al} = m_{Al} : m_{Cr} : m_{Fe}$$

where B_A refers to the atomic isotropic factor of element A and m_A refers to the atomic mass of A. The mean-square thermal vibrations, proportional to the isotropic temperature factors have been shown to be inversely proportional to the mass of the atom. Since we don't know their values, we fix their ratios in the least-squares refinement. Once reasonable values of χ^2 (< 0.2) are achieved, the site occupancies are refined keeping the stoichiometry fixed and maintaining one atom per site.

3.7 Determination of site occupancies

Comparisions of the iron, aluminum and chromium x-ray atomic scattering factors at the three different energies for different values of $\sin(\theta/\lambda)$ shall be shown. Tables 3.7, 3.8, 3.9 give the values of $f_0 + f'$ (the real part of the atomic

TABLE 3.7 : $f_o + f'$ values for Fe, Al and Cr over a range of $\sin(\theta/\lambda)$ values at an energy of 8.04 keV (Cu-Kα)

Atom	$f_o + f'$			
	$\sin(\theta/\lambda)$			
	0.2	0.3	0.4	0.5
Fe	18.898	15.578	12.648	10.278
Al	9.363	8.083	6.973	5.893
Cr	18.163	14.803	12.013	9.933

TABLE 3.8 : $f_o + f'$ values for Fe, Al and Cr over a range of $\sin(\theta/\lambda)$ values at an energy of 7.097 keV (near Fe-edge)

Atom	$f_o + f'$			
	$\sin(\theta/\lambda)$			
	0.2	0.3	0.4	0.5
Fe	14.330	11.010	8.080	5.710
Al	9.399	8.119	7.010	5.930
Cr	17.559	14.199	11.410	9.330

TABLE 3.9 : $f_o + f'$ values for Fe, Al and Cr over a range of $\sin(\theta/\lambda)$ values at an energy of 5.974 keV (near Cr-edge)

Atom	$f_o + f'$			
	$\sin(\theta/\lambda)$			
	0.2	0.3	0.4	0.5
Fe	18.402	15.082	12.152	9.782
Al	9.448	8.168	7.058	5.978
Cr	12.420	9.060	6.270	4.190

scattering factor) with $\sin(\theta/\lambda)$ for the 3 different wavelengths. We shall choose $\sin(\theta/\lambda) = 0.2, 0.3, 0.4, 0.5$. The first 3 values are very close to the superlattice peaks (100), (111), (210) respectively. $\sin(\theta/\lambda) = 0.5$ is close to the fundamental (211) reflection. Changes as large as 50% in the x-ray atomic scattering factors can be produced.

3.7.1 Site refinement for binary alloys

For the binary alloys, site refinement was performed at x-ray data taken at 8.04 keV (Cu K_α), the synchrotron data at 7.097 keV (near the Fe edge) and 5.974 keV (near the Cr edge). Before refinement, the site positions of these Fe-rich alloys ($Fe_{0.5+x}Al_{0.5-x}$) were entered into GSAS as follows :

Atom No.	Atom type	Position	Fraction
1	Fe	(0 0 0)	1
2	Al	(0 0 0)	0
3	Fe	(1/2 1/2 1/2)	2x
4	Al	(1/2 1/2 1/2)	1 - 2x

As seen, the first two atoms are at the cell corners and the other two at the cell center. The column labeled Fraction is consistent with the alloy stoichiometry and the occupancy of one atom per site. Site refinement was done by fixing the stoichiometry and the occupancy of one atom per site. These conditions were met as follows:

Atom No.	Parameter	Coefficient
1	FRAC	+1
2	FRAC	-1
3	FRAC	-1
4	FRAC	+1

The coefficients indicate the magnitude and direction of change of the atom fractions on a particular site. Sites with the same coefficient (magnitude and sign) will increase or decrease by equal amounts while sites having the same coefficient magnitudes but of opposite sign will change by identical amounts in the opposite direction. We see that the above constraints are such that they fix the stoichiometry and the occupancy of one atom per site. Site refinement is performed under these constraints. To obtain more reliable results, the site preference refinement is also performed on all the energies simultaneously

.

3.7.2 Site refinement for ternary alloys

For a ternary alloy ABC, we have done the site refinement by two different methods.

Method 1

We first refine the data taken with the Cu K_α radiation. This is because at this energy, the atomic scattering factors of iron and chromium differ by only a small amount (refer to Tables 3.3 and 3.4). Thus, this data is most sensitive to the sites of the Al atoms since Cr is almost indistinguishable from Fe. With this data, there is only one site occupation parameter to refine as Fe and Cr are treated as the same atom.

We proceed by considering two extreme cases of chromium site preference for the alloy $Fe_{0.5+x}Al_{0.5-y}Cr_{y-x}$:

1) All the chromium goes to the Al-site - In this case, we put only Fe atoms on the Fe-site, all the Al and Cr on the Al-site and the excess Fe on the Al-site. By fixing the Cr atom occupancy, we then refine the site occupancies of the Fe and Al atoms, maintaining stoichiometry and one atom per site.

Atom No.	Atom type	Position	Fraction
1	Fe	(0 0 0)	1
2	Al	(0 0 0)	0
3	Cr	(0 0 0)	0
4	Fe	(1/2 1/2 1/2)	2x
5	Al	(1/2 1/2 1/2)	1 - 2y
6	Cr	(1/2 1/2 1/2)	2y - 2x

The refinement is done with the following constraints which maintain the stoichiometry and the occupancy of one atom per site.

Atom No.	Parameter	Coefficient
1	FRAC	+1
2	FRAC	-1
4	FRAC	-1
5	FRAC	+1

2) All the chromium goes to the the Fe-site - In this case we put all the Cr on the Fe-site, and Fe atoms on the balance of the Fe-site. We then put all the Al and the remaining Fe on the Al-site. Again by fixing the Cr site occupancy, we then refine the site occupancies of the Fe and Al sites, maintaining the conditions of stoichiometry and crystal structure. In this case, the site occupation constraints are identical to those mentioned above.

Atom No.	Atom type	Position	Fraction
1	Fe	(0 0 0)	1 - (2y - 2x)
2	Al	(0 0 0)	0
3	Cr	(0 0 0)	2y -2x
4	Fe	(1/2 1/2 1/2)	2y
5	Al	(1/2 1/2 1/2)	1 - 2y
6	Cr	(1/2 1/2 1/2)	0

By this method, we get different, although very similar values of the site occupancies of the aluminum atom. This is because the f values of iron and chromium are so close that it really does not make much difference to the site position of the aluminum atom if we introduce chromium atoms on the Fe-site at the expense of the iron atoms. The actual site positioning of the Al atom would be in-between these two nearly-similar values, and would depend upon the site preference of the Cr atom.

Since the f values of iron and chromium at the Fe-edge and Cr-edge are appreciably different, it is possible to determine the site occupancy of the iron and chromium atoms from data at these two energies. Refinement is performed separately at these two energies by fixing the aluminum site distribution, obtained from the mean of the results at 8.04 keV (Cu K_α). Determination of site occupancy of Fe and Cr atoms is conducted by refining the site positioning of the iron and chromium atoms. To get more reliable results, refinement is also performed simultaneously near the Fe and Cr-edges with the Al site preference fixed from results at 8.04 keV. The site occupation constraints at these two edges are :

Atom No.	Parameter	Coefficient
1	FRAC	+1
3	FRAC	-1
4	FRAC	-1
6	FRAC	+1

Site preferences of atoms 2 and 4, i.e. the Al atoms are fixed from the results obtained from the Cu Kα data.

Method 2

In this method, we refine the site positions of Fe, Al and Cr simultaneously maintaining the stoichiometry and the occupation of one atom per site. We see from Tables 3.3 and 3.4 that the data at 8.04 keV is insensitive to the site positions of Fe and Cr, the data at 5.974 keV is insensitive to the site positions of Al and Cr (especially at higher diffraction angles), and the data at 7.097 keV is insensitive to the site positions of Fe and Cr at low angles and to the positions of Al and Cr at higher angles. Therefore, refinement is performed in pairs, i.e., Fe edge - Cu K_α, Fe edge - Cr edge, Cr edge - Cu K_α, and finally for all the three wavelengths together. Stoichiometry and the occupation of one atom per site are fixed by the following three constraints :

I

Atom No.	Parameter	Coefficient
1.	FRAC	+1
2.	FRAC	-1
4.	FRAC	-1
5.	FRAC	+1

II

Atom No.	Parameter	Coefficient
1.	FRAC	+1
3.	FRAC	-1
4.	FRAC	-1
6.	FRAC	+1

III

Atom No.	Parameter	Coefficient
2.	FRAC	+1
3.	FRAC	-1
5.	FRAC	-1
6.	FRAC	+1

3.8 Microhardness measurements

The polished specimens were tested for hardness with the help of a Leitz Hardness testing equipment. Each specimen was given 4-8 indentations of a 100g load depending upon the standard deviation of the results.

Chapter 4

Calculation of ternary element site preference in FeAl by thermodynamic considerations

A brief description of this method of determining site preference has already been mentioned in section 2.8. Here we shall show how we determine the site preference of ternary elements for the B2 FeAl system [23].

For convenience let A and B represent the Fe and Al atoms respectively. Let C denote the ternary element. Let the deviations from stoichiometry be given as :

$X_A = 0.5 - C_A$,

$X_B = C_B - 0.5$,

$X_C = C_C$, where C_A, C_B and C_C represent the atomic fractions of A, B and C respectively in the alloy ($C_A + C_B + C_C = 1$).

If the randomness of atomic distribution for each site is assumed, the number of atoms at each site can be obtained by :

$$[A/a] = N [0.5 - (X_A + z)],$$

$$[A/b] = Nz,$$

$$[B/a] = N [X_B + z + k],$$

$$[B/b] = N [0.5 - z - k],$$

$$[C/a] = N [X_C - k],$$

$$[C/b] = Nk, \qquad (4.1)$$

where the symbol [A/a] represents the number of A atoms on a-sites, and similarly for the other atoms. The new parameters z and k are introduced to describe the anti-structure defect.

We use the expressions in eq.(4.1) to obtain the number of nearest neighbor pairs of each kind (N_{AA} represents the number of nearest neighbors of atoms

A-A). The value N_{AB} is found by summation of the bonds between A atoms on a-site and B atoms on b-site, with the bonds between A atoms on b-site and B atoms on a-site.

$N_{AA} = 16\,Nz\,[0.5 - (X_A + z)]$,

$N_{BB} = 16\,N\,[X_B + z + k]\,[0.5 - z - k]$,

$N_{CC} = 16\,Nk\,[X_C - k]$,

$N_{AB} = 16\,Nz\,[X_B + z + k] + 16\,N\,[0.5 - (X_A + z)]\,[0.5 - z - k]$,

$N_{AC} = 16\,Nk\,[0.5 - (X_A + z)] + 16\,Nz\,[X_C - k]$,

$N_{BC} = 16\,Nk\,[X_B + z + k] + 16\,N\,[0.5 - z - k]\,[X_C - k]$. (4.2)

In general, the total bond energy, H, is expressed as :

$H = N_{AA} H_{AA} + N_{BB} H_{BB} + N_{CC} H_{CC} + N_{AB} H_{AB} + N_{BC} H_{BC} + N_{AC} H_{AC}$, where H_{AA} is the bond energy for AA pairs, and similarly for the other pairs.

Let us consider the change in total bond energy in the equiatomic AB by a small addition of the ternary component C for two extreme substitution cases, namely a-direction and b-direction. In the case for a-direction in which C atoms exclusively substitute for A atoms in the a-site, the conditions are $X_A = X_C$ and $X_B = z = k = 0$.

The total energy H(a) can then be written as

$H(a) = 8\,N\,[0.5 - X_A]\,H_{AB} + 8\,N\,X_C$. (4.3)

In case for b-direction in which C atoms exclusively substitute for B atoms in the b-site, the conditions are $X_A = z = 0$, and $-X_B = X_C = k$. The total bond energy H(b) can then be written as

$H(b) = 8\,N\,[0.5 - X_C]\,H_{AB} + 8\,N\,X_C$. (4.4)

We now introduce the interaction parameter V. $V_{AB} = H_{AB} - (H_{AA} + H_{BB})/2$ and similarly for the formation of the other pairs. Eq(4.3) now becomes

$H(a) = 2\,N\,[(1 - 2\,X_C)\,H_{AA} + H_{BB} + 2\,(1 - 2\,X_C)\,V_{AB} + 4\,X_C\,V_{BC} + 2\,X_C\,H_{CC}]$. (4.5)

Eq(4.4) now becomes

$$H(b) = 2N[H_{AA} + (1 - 2X_C)H_{BB} + 2X_C H_{CC} + 2(1 - 2X_C)V_{AB} + 4X_C V_{AC}]. \quad (4.6)$$

In comparison between H(a) and H(b), the site-preference for a ternary addition of C atoms can be directed by the following expression

$[dH(b)/dX_C]_{X_C=0} \gtrless [dH(a)/dX_C]_{X_C=0}$.

If the quantity on the left-hand side is larger, the substitution of a-direction is preferred. If that on the right-hand is larger, the substitution for b-direction is preferred.

Using expressions (4.5) and (4.6),

$$[dH(a)/dX_C]_{X_C=0} = -4H_{AA} - 8V_{AB} + 8V_{BC} + 4H_{CC}. \quad (4.7)$$

$$[dH(b)/dX_C]_{X_C=0} = -4H_{BB} - 8V_{AB} + 8V_{AC} + 4H_{CC}. \quad (4.8)$$

Equations (4.8) and (4.9) reduce to

$$V_{AC}/V_{AB} \gtrless V_{BC}/V_{AB} + T \quad (4.10)$$

where $T = (H_{AA} - H_{BB})/2V_{AB}$

Calculation of interaction parameters

To find the values V_{AB} etc., we have used the method developed by Miedema and coworkers [19] for the prediction of the heat of alloy formation.

According to this method, the interaction parameter V is given as :

$V \sim [-P e (\Delta\phi)^2 + Q_o (\Delta n_{ws}^{1/3})^2 - R]$, where Δn_{ws} is the discontinuity in the density of electrons at the boundary between dissimilar Wigner-Seitz cells, $\Delta\phi$ is the difference in chemical potential for electrons in the two types of pure metal cells, e is the elementary charge, and P, Q, R are constants for a particular class of metals, eg. transition-transition or transition-non transition metal bondings etc.

According to Vidula, Titran and Anderson [30] and Mendiratta [18], Cr, Ti, Mn, V, Co and Ni are soluble in FeAl up to at least 5 at.%. To calculate the interaction parameters between these elements, Fe and Al, we have used the values of n_{ws}, ϕ, P, Q and R provided by Miedema [19]. These values are given in Table 4.1 and 4.2

We recall that site preference can be obtained from eq.(4.10). Therefore, we calculate the values V_{AB}, V_{AC}, V_{BC}, V_{AC}/V_{AB}, V_{BC}/V_{AB}. These values are tabulated in Table 4.3 for A = Fe, B = Al and C = Cr, Ti, Mn, Co and Ni. The intercept T cannot be calculated as it is not possible to calculate the values H_{AA}. We then plot V_{AC}/V_{AB} vs. V_{BC}/V_{AB} (Figure 4.1). A line drawn with intercept T and a slope of 1 would divide the points into two categories. The points that would fall above the line would reflect those elements that show a preference for the Al-site while the points below the line would be for the elements that show a preference for the Fe-site. Since the value of T is unknown, it is not possible to determine the site preferences of the ternary elements. However, by constructing lines at 45° to the axes, we see that among all the ternary elements considered, Cr and V show the greatest preference for the Al-site.

TABLE 4.1 : Parameters ϕ and nws for calculation of interaction parameters

Metal	ϕ	$(n_{ws})^{1/3}$
Fe	4.93	1.77
Al	4.20	1.39
Cr	4.65	1.73
Ti	3.65	1.47
V	4.25	1.64
Mn	4.45	1.61
Co	5.10	1.75
Ni	5.20	1.75

TABLE 4.2 : Values P, Q and R for calculation of interaction parameter

	Metal B is a transition metal		
Metal A	$P(V^{-1})$	$Q(eV^{1/2}/d.u.)^{2/3}$	R(eV)
Transition metal	1.05	9.87	0
Aluminum	0.85	7.99	1.615

TABLE 4.3 : Interaction parameters of ternary additions (C) with Fe (A) and Al (B). $V_{AB} = -7.67$

Ternary addition	V_{AC}	V_{BC}	V_{AC}/V_{AB}	V_{BC}/V_{AB}
Cr	-0.56	-7.25	.073	0.95
Ti	-7.00	-15.30	.910	2.00
Mn	0.09	-10.76	-.012	1.40
Co	-0.22	-10.65	.029	1.39
V	-2.68	-9.39	.350	1.22
Ni	-0.61	-12.00	.080	1.56

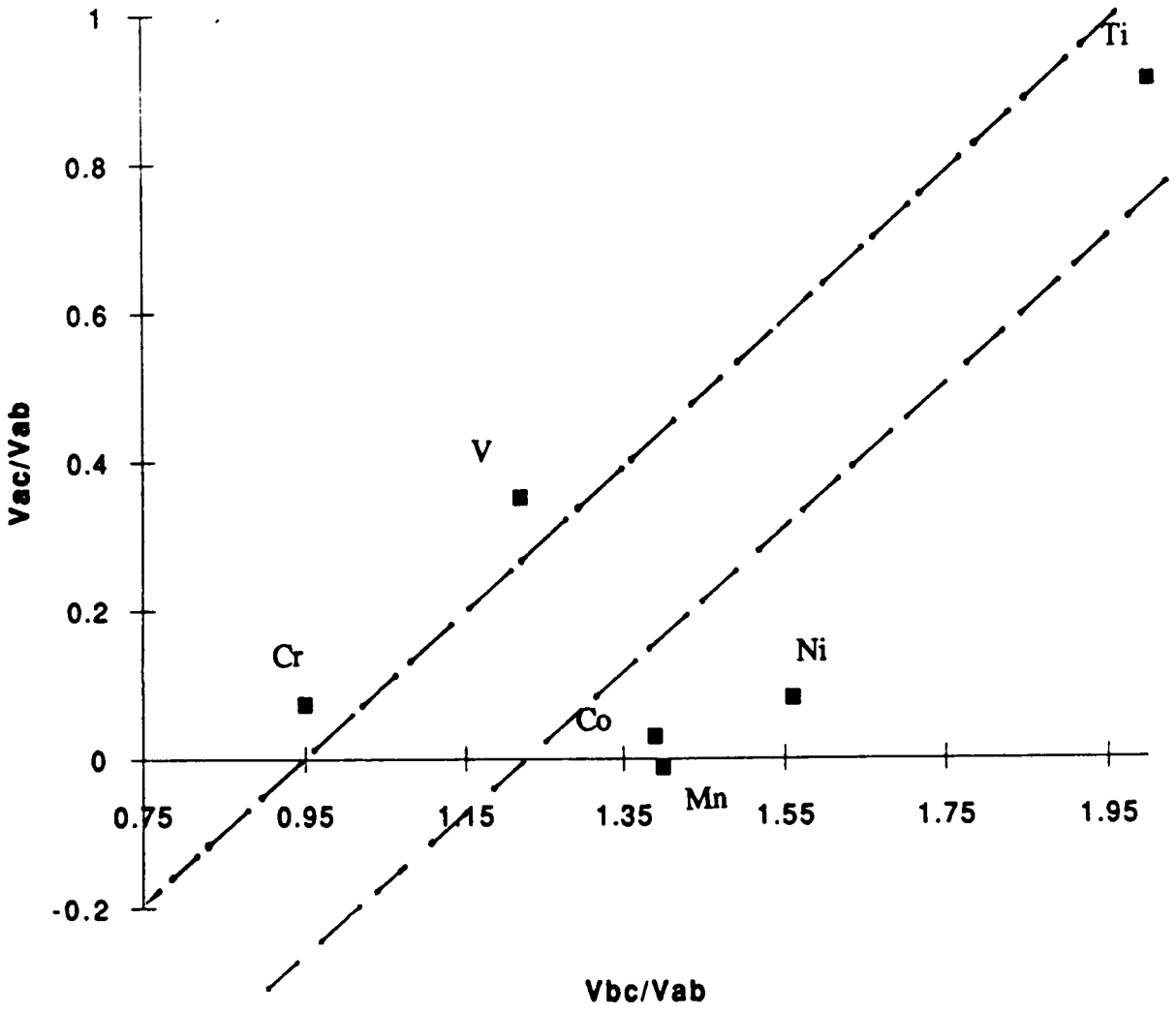

Figure 4.1 V_{AC}/V_{AB} vs V_{BC}/V_{AB} for Fe(A)-Al(B)-X(C) alloys

Chapter 5

Results and discussion

5.1 Results

Tables 5.1 to 5.35* show the site preferences of the Fe, Al and Cr atoms for all the specimens as determined from energies at 8.04, 7.097 and 5.974 keV. Table 5.36 compares the result of Rietveld refinement on data corrected and uncorrected for granularity. The lattice parameters, as calculated by GSAS from the original data are shown in Table 5.37. Tables 5.38 and 5.39 show respectively the mean and the standard deviations of the hardness values for specimens annealed at 1000°C for 1 hour, and 400°C for 5 days. Tables 5.40 to 5.46 give the mean values of the site occupancies alongwith the standard deviations, for all the specimens. Table 5.47 compares the site occupation results of the Rietveld analysis with those from the atom probe for $Fe_{57.5}Al_{37.5}Cr_5$.

The Rietveld analysis plots are shown in Figures 5.1 to 5.17. In each plot is shown the constructed profile (as modified after deadtime and granularity corrections and with a Gaussian distribution), the calculated profile (as calculated by GSAS) and the difference of the two profiles. The inset profile shows the actual diffraction profile for that sample. Figures 5.18 and 5.19 show respectively the hardness values vs. (Al + Cr) concentration for annealing treatments of 1000°C (1 hour) and 500°C (5 days). Figure 5.20 shows the lattice parameters of the alloys as a function of the Al/Fe ratio.

---

* For reading convenience, Tables 5.1 to 5 .47 and Figures 5.1 to 5.25 may be found at the end of the Chapter

From the diffraction profiles, we note that most of the peaks are very well fitted by the Rietveld peak profiles. The χ^2 values, an indication of the goodness of fit, are shown from Table 5.27 to Table 5.34 for a typical specimen, 55C. These values indicate a good fit between the constructed and Rietveld calculated profiles. It may be noted that the χ^2 values obtained by method 1 are slightly lower than those by method 2. This is not surprising since method 2 gives an average value of site occupancies from the different energies while method 1 gives the site occupation from only one x-ray energy at a time. It can also be seen from the tables that the thermal parameters (U_{iso} values) vary significantly for each sample across different energies. This may be because we have corrected for the granularity measured at 8.3 keV and used this correction factor at all the energies without considering the dependence of the granularity factor on the wavelength of the incident beam.

The site determination of the ternary alloys by the two different methods mentioned in Chapter 3 is described for the case of the refinement of $Fe_{55}Al_{40}Cr_5$. The refinement results for this sample are given in Tables 5.27 to 5.34. In Table 5.27, the site position of the Al atoms is determined by first fixing all the Cr on the Al site and then on the Fe site at the Cu Kα energy. The first of the two Fraction columns gives the atom site positions when all the Cr is fixed on the Al site while the second Fraction column gives the atom site positions when all the Cr is fixed on the Fe site. From this we conclude that the percentage of Fe sites occupied by Al atoms is between 0.9% and 2% and the percentage of Al sites occupied by Al atoms is between 78.3% and 79.4%. The mean values of the Al site occupations (1.5 % of the Fe sites and 78.9% of the Al sites) is fixed near the Cr and Fe edges (Tables 5.28 and 5.29). Site refinement at these two energies is performed on the Fe and Cr atoms. Site refinement is also performed simultaneously at these two energies (Table 5.30) with the Al atoms fixed from Table 5.27. From this method of determination we conclude that the Cr atom has a

preference for the Al sublattice, with about 1.5% of the Fe sites occupied by Al atoms. Tables 5.31 to 5.34 give the site occupation results as determined by method 2. Table 5.31 gives the site occupations of the Fe, Al and Cr atoms by refining simultaneously near the Fe edge and Cr edge. Table 5.34 gives the site occupations when refinement is performed at all the three wavelengths simultaneously. By this method, we conclude that all the Cr is on the Al sublattice with about 4% of the Fe sublattice occupied by Al atoms.

5.2 Discussion

Before we talk of the site occupation of Cr and the fraction of Al anti-site defects, let us examine the results of site occupation for data corrected and uncorrected for granularity. Table 5.36 compares the results of the Rietveld analysis for data corrected and uncorrected for granularity for specimen 60. It can be seen from Figure 3.3 that specimen 60 shows substantial granularity. It is seen that the data uncorrected for granularity yields nearly similar values of site occupation to those obtained after correcting for granularity. However, the thermal parameters are significantly lower in the case of the data uncorrected for granularity. This can be explained by examining typical profiles of granularity curves with the thermal parameter curves. Figure 3.3 shows the changes in flourescent intensity with scattering angles from the specimens. A reduction in flourescent intensity is observed as the scattering angle is decreased. We find that the general shape of the curves is similar with a nearly linear fall off down to about 30° 2θ where the intensity begins to fall rapidly. The similarity of the intensity reduction from granularity can be compared to the effect of the thermal parameter, e^{-2M}, plotted in Figure 5.21. If we make the sign of the mean-square displacement, U_{iso}, negative, where $2M = 16\,\pi^2\,U_{iso}\,\sin^2\theta/\lambda^2$ or plot $1/e^{-2M}$ and then scale the result so that the value of e^{+2M} is equal to unity at $2\theta = 180^{\circ}$, the

curve labeled U_{iso} in Figure 5.21 results. This curve bears a resemblance to the granularity reduction in intensity and shows why the thermal parameters are too small when obtained from x-ray powder data affected by granularity. In Rietveld analysis, there is no separate correction for the granularity effect so the thermal parameter tries to compensate for the low 2θ intensity reduction (just opposite to the usual temperature reduction at high 2θ) by scaling the data with smaller thermal displacements which can even go negative [28].

Site substitution information is not easily obtained and its scarcity makes it difficult to draw any general conclusion about materials properties based on substitution information. Our observations here should be received as new information and more systematic than the few other studies of site substitution. Tables 5.40 to 5.46 show the site substitution data for the seven samples with the estimated error. We note that Cr has a strong tendency to substitute on the Al sublattice, with there being no Cr present on the Fe sublattice within experimental error. A look at the Fe-Cr phase diagram (Figure 5.22) shows a miscibility gap. The Al-Cr binary phase diagram (Figure 5.23) shows a series of compounds which reflects the preference of Cr to form atomic pairs with Al. If we look at the crystal structure of the ordered B2 phase (Figure 2.2), we note that an Al atom has all Fe first neighbors. On the basis of a simplistic counting of only first neighbor bonds, a Cr atom on the Al site would have Fe atoms as first neighbors which it avoids when alloyed to pure Fe. Thus this simplistic bond argument would seem to suggest that Cr might prefer to be on the Fe sublattice where it would have predominantly Al atoms as first neighbors. As observed from the data, Cr has a strong preference for the Al site where it has Al as second neighbors. The more developed approach of Chapter 4 did predict that Cr has a stronger preference for the Al site than other third row transition elements. With reference to eq.(4.10), if VFeCr/VFeAl > VAlCr/VFeAl + T, then Cr prefers to substitute for Al. If we neglect

T, then VFeCr > VAlCr. From the phase diagram, we can argue that Cr does not like Fe neighbors but prefers to bond to Al so that VFeCr < VAlCr and Cr should go to the Fe sites. But this ignores the value of T which could be significant. Another approach is to ask whether Cr behaves more like Al or like Fe. From the Al-Cr and Fe-Cr binary phase diagrams, we would believe that Cr is more like Al in its behavior since the Cr phase separates from Fe but has some solubility for Al and forms with it several compounds. We should then make the argument that if Cr behaves more like Al than like Fe, then it would prefer to sit on the same sites as the Al atoms.

Even for the Fe-rich binary alloys, some Al occupies the Fe sites. These anti-site defects constitute about 5 % of the Fe sites. On the addition of Cr, the fraction of Al anti-site defects varies considerably with Al concentration. Plotted in Figure 5.24 are the fraction of Fe sites occupied by Al atoms for the various at.% Al/at.% Fe studied. The lesser the amount of Al on the Fe sublattice, the more ordered the alloy as more of the sites are correctly occupied. There is a large increase in the number of Al atoms going to the Fe site between 59.5 and 60.5 at.% Fe. We speculate whether this additional ordering tendency could push the alloy towards the DO_3 phase. However, in general, as the composition of the alloy approaches 50 at.%Al, the ordering improves. From Table 5.47, we note that the results of the Rietveld analysis, within the limits of standard deviation agree with those of the atom probe.

As Al has the largest atomic radius, we see that Al expands the lattice with increasing concentration (Figure 5.20). Hardness data, obtained from air cooling from 500°C (5 days) was rather insensitive to Al concentrations other than the one with 49 at.% Al which showed much higher hardness. This agrees with the results of Chang, Pike and others [5] who found that annealing out of vacancies at low temperatures results in hardness values insensitive to Al content up to 47 at.% Al.

Since hardness is not correlated with Al content, we would not expect it to be sensitive to site occupations.

It is also observed that for alloys annealed at 1000°C for 1 hour, the hardness increases with Al content in the B2 region. Addition of Cr results in a drop in hardness, the reason for which has been attributed by Munroe and Baker to a lower retention of vacancies, and solute softening caused by the Cr atom [19]. The microstructure of Fe59Al36Cr5 (sample 59C) is shown in Figure 5.25 at a magnification of 50x. From the microstructure, we observe the presence of large grains with considerable pitting.

The chemistry of the phase stability of these ternary solid solutions is important to their synthesis and properties. Our understanding of site substitution is poor and the data that exists is meagre. Nevertheless, the alloying of metals and studies of their properties is an important materials undertaking in the search for better and new properties. This site occupation study has added significantly to the limited data base of knowledge. This work has shown that binary phase diagrams can provide guidance to the synthesis of ternary alloys. Reliable site occupation parameters provide a test for theories and should stimulate theoretical explanation.

TABLE 5.1 : Atom site occupations determined from x-ray data at 8.04 keV (Cu K_α) for sample 60 ($Fe_{60}Al_{40}$)

Atom No.	Atom type	Position	Fraction	U_{iso}
1	Fe	0	0.942	0.00335
2	Al	0	0.058	0.00696
3	Fe	1/2	0.258	0.00335
4	Al	1/2	0.742	0.00696

TABLE 5.2 : Atom site occupations determined from x-ray data at 7.097 keV (Fe edge) for sample 60 ($Fe_{60}Al_{40}$)

Atom No.	Atom type	Position	Fraction	U_{iso}
1	Fe	0	0.947	0.00575
2	Al	0	0.053	0.01192
3	Fe	1/2	0.253	0.00575
4	Al	1/2	0.747	0.01192

TABLE 5.3 : Atom site occupations determined from x-ray data at 5.974 keV (Cr edge) for sample 60 ($Fe_{60}Al_{40}$)

Atom No.	Atom type	Position	Fraction	U_{iso}
1	Fe	0	0.955	0.00509
2	Al	0	0.045	0.01055
3	Fe	1/2	0.245	0.00509
4	Al	1/2	0.755	0.01055

TABLE 5.4 : Atom site occupations determined from x-ray data at all the energies together for sample 60 ($Fe_{60}Al_{40}$)

Atom No.	Atom type	Position	Fraction	U_{iso}
1	Fe	0	0.948	0.00425
2	Al	0	0.052	0.00880
3	Fe	1/2	0.252	0.00425
4	Al	1/2	0.748	0.00880

TABLE 5.5 : Atom site occupations determined from x-ray data at 8.04 keV (Cu K_α) for sample 55 ($Fe_{55}Al_{45}$)

Atom No.	Atom type	Position	Fraction	U_{iso}
1	Fe	0	0.937	0.00003
2	Al	0	0.063	0.00007
3	Fe	1/2	0.163	0.00003
4	Al	1/2	0.837	0.00007

TABLE 5.6 : Atom site occupations determined from x-ray data at 7.097 keV (Fe edge) for sample 55 ($Fe_{55}Al_{45}$)

Atom No.	Atom type	Position	Fraction	Uiso
1	Fe	0	0.934	0.00527
2	Al	0	0.066	0.01087
3	Fe	1/2	0.166	0.00527
4	Al	1/2	0.834	0.01087

TABLE 5.7 : Atom site occupations determined from x-ray data at both the energies together for sample 55 ($Fe_{55}Al_{45}$)

Atom No.	Atom type	Position	Fraction	U_{iso}
1	Fe	0	0.936	0.00323
2	Al	0	0.064	0.00669
3	Fe	1/2	0.164	0.00323
4	Al	1/2	0.836	0.00669

TABLE 5.8 : Atom site occupations determined from x-ray data at 8.04 keV (Cu K_α) for sample 51 ($Fe_{51}Al_{49}$)

Atom No.	Atom type	Position	Fraction	U_{iso}
1	Fe	0	0.969	0.00448
2	Al	0	0.031	0.00928
3	Fe	1/2	0.051	0.00448
4	Al	1/2	0.949	0.00928

TABLE 5.9 : Atom site occupations determined from x-ray data at 7.097 keV (Fe edge) for sample 51 ($Fe_{51}Al_{49}$)

Atom No.	Atom type	Position	Fraction	U_{iso}
1	Fe	0	0.942	0.00448
2	Al	0	0.058	0.00928
3	Fe	1/2	0.080	0.00448
4	Al	1/2	0.920	0.00928

TABLE 5.10 : Atom site occupations determined from x-ray data at 7.097 keV (Fe edge) and 8.04 keV (Cu K_α) for sample 51 ($Fe_{51}Al_{49}$)

Atom No.	Atom type	Position	Fraction	Uiso
1	Fe	0	0.954	0.00527
2	Al	0	0.046	0.01087
3	Fe	1/2	0.066	0.00527
4	Al	1/2	0.934	0.01087

TABLE 5.11 : Site occupation for Al determined for sample 60C ($Fe_{60}Al_{35}Cr_5$) from x-ray data at 8.04 keV (Cu K_α) where Fe and Cr have similar atomic scattering factors

Atom No.	Atom type	Position	Fraction	U_{iso}	Fraction	Uiso
1	Fe	0	0.992	0.00097	0.921	0.00097
2	Al	0	0.008	0.00202	-0.002	0.00202
3	Cr	0	0.000 fixed	0.00105	0.081 fixed	0.00105
4	Fe	1/2	0.220	0.00097	0.290	0.00097
5	Al	1/2	0.699	0.00202	0.710	0.00202
6	Cr	1/2	0.081 fixed	0.00105	0.000 fixed	0.00105

TABLE 5.12 : Site occupation for Fe and Cr determined for sample 60C ($Fe_{60}Al_{35}Cr_5$) from synchrotron data at 5.974 keV (Cr edge) with Al atomic positions fixed from mean of Cu K_α results (Table 5.11)

Atom No.	Atom type	Position	Fraction	U_{iso}
1	Fe	0	0.990	0.00340
2	Al	0	0.003 (fixed)	0.00706
3	Cr	0	0.007	0.00366
4	Fe	1/2	0.221	0.00340
5	Al	1/2	0.704 (fixed)	0.00706
6	Cr	1/2	0.075	0.00366

TABLE 5.13 : Site occupation for Fe and Cr determined for sample 60C ($Fe_{60}Al_{35}Cr_5$) from synchrotron data at 7.097 keV (Fe edge) with Al atomic positions fixed from mean of Cu K_α results (Table 5.11)

Atom No.	Atom type	Position	Fraction	U_{iso}
1	Fe	0	1.010	0.00340
2	Al	0	0.003 (fixed)	0.00706
3	Cr	0	-0.013	0.00366
4	Fe	1/2	0.202	0.00340
5	Al	1/2	0.704 (fixed)	0.00706
6	Cr	1/2	0.094	0.00366

TABLE 5.14 : Site occupation for Fe and Cr determined for sample 60C ($Fe_{60}Al_{35}Cr_5$) from synchrotron data at 7.097 keV (Fe edge) and 5.974 keV (Cr edge) with Al atomic positions fixed from mean of Cu K_α results (Table 5.11)

Atom No.	Atom type	Position	Fraction	U_{iso}
1	Fe	0	0.994	0.00394
2	Al	0	0.003 (fixed)	0.00817
3	Cr	0	0.003	0.00423
4	Fe	1/2	0.217	0.00394
5	Al	1/2	0.704 (fixed)	0.00817
6	Cr	1/2	0.079	0.00423

TABLE 5.15 : Site occupation determined for sample 60C ($Fe_{60}Al_{35}Cr_5$) from synchrotron data at 7.097 keV (Fe edge) and 5.974 keV (Cr edge)

Atom No.	Atom type	Position	Fraction	U_{iso}
1	Fe	0	0.991	0.00401
2	Al	0	0.008	0.00831
3	Cr	0	0.001	0.00431
4	Fe	1/2	0.220	0.00401
5	Al	1/2	0.700	0.00831
6	Cr	1/2	0.080	0.00431

TABLE 5.16 : Site occupation determined for sample 60C ($Fe_{60}Al_{35}Cr_5$) from synchrotron data at 7.097 keV (Fe edge) and 8.04 keV (Cu K_α)

Atom No.	Atom type	Position	Fraction	U_{iso}
1	Fe	0	0.973	0.00406
2	Al	0	0.017	0.00841
3	Cr	0	0.009	0.00436
4	Fe	1/2	0.238	0.00406
5	Al	1/2	0.690	0.00841
6	Cr	1/2	0.072	0.00436

TABLE 5.17 : Site occupation determined for sample 60C ($Fe_{60}Al_{35}Cr_5$) from synchrotron data at 5.974 (Cr edge) and 8.04 keV (Cu K_α)

Atom No.	Atom type	Position	Fraction	U_{iso}
1	Fe	0	0.994	0.00297
2	Al	0	0.012	0.00617
3	Cr	0	-0.006	0.00320
4	Fe	1/2	0.218	0.00297
5	Al	1/2	0.695	0.00617
6	Cr	1/2	0.087	0.00320

TABLE 5.18 : Site occupation determined for sample 60C ($Fe_{60}Al_{35}Cr_5$) from synchrotron data at all the three wavelengths

Atom No.	Atom type	Position	Fraction	U_{iso}
1	Fe	0	0.988	0.00395
2	Al	0	0.011	0.00819
3	Cr	0	0.001	0.00424
4	Fe	1/2	0.223	0.00395
5	Al	1/2	0.696	0.00819
6	Cr	1/2	0.081	0.00424

TABLE 5.19 : Site occupation for Al determined for sample 57C ($Fe_{57.5}Al_{37.5}Cr_5$) from x-ray data at 8.04 keV (Cu K_α) where Fe and Cr have similar atomic scattering factors

Atom No.	Atom type	Posi-tion	Fraction	U_{iso}	Fraction	Uiso
1	Fe	0	0.890	0.00125	0.812	0.00116
2	Al	0	0.110	0.00260	0.098	0.00242
3	Cr	0	0.000 fixed	0.00135	0.090 fixed	0.00126
4	Fe	1/2	0.266	0.00125	0.344	0.00116
5	Al	1/2	0.644	0.00260	0.656	0.00242
6	Cr	1/2	0.090 fixed	0.00135	0.000 fixed	0.00126

TABLE 5.20 : Site occupation for Fe and Cr determined for sample 57C ($Fe_{57.5}Al_{37.5}Cr_5$) from synchrotron data at 5.974 keV (Cr edge) with Al atomic positions fixed from mean of Cu K_α results (Table 5.19)

Atom No.	Atom type	Position	Fraction	U_{iso}
1	Fe	0	0.948	0.00336
2	Al	0	0.104 (fixed)	0.00698
3	Cr	0	-0.052	0.00362
4	Fe	1/2	0.208	0.00336
5	Al	1/2	0.650 (fixed)	0.00698
6	Cr	1/2	0.142	0.00362

TABLE 5.21 : Site occupation for Fe and Cr determined for sample 57C ($Fe_{57.5}Al_{37.5}Cr_5$) from synchrotron data at 7.097 keV (Fe edge) with Al atomic positions fixed from mean of Cu K_α results (Table 5.19)

Atom No.	Atom type	Position	Fraction	U_{iso}
1	Fe	0	0.856	0.00468
2	Al	0	0.104 (fixed)	0.00970
3	Cr	0	0.040	0.00503
4	Fe	1/2	0.300	0.00468
5	Al	1/2	0.650 (fixed)	0.00970
6	Cr	1/2	0.050	0.00503

TABLE 5.22 : Site occupation for Fe and Cr determined for sample 57C ($Fe_{57.5}Al_{37.5}Cr_5$) from synchrotron data at 7.097 keV (Fe edge) and 5.974 keV (Cr edge) with Al atomic positions fixed from mean of Cu K_α results (Table 5.19)

Atom No.	Atom type	Position	Fraction	U_{iso}
1	Fe	0	0.903	0.00445
2	Al	0	0.104 (fixed)	0.00920
3	Cr	0	0.007	0.00478
4	Fe	1/2	0.252	0.00445
5	Al	1/2	0.650 (fixed)	0.00920
6	Cr	1/2	0.083	0.00478

TABLE 5.23 : Site occupation determined for sample 57C ($Fe_{57.5}Al_{37.5}Cr_5$) from synchrotron data at 7.097 keV (Fe edge) and 5.974 keV (Cr edge)

Atom No.	Atom type	Position	Fraction	U_{iso}
1	Fe	0	0.936	0.00445
2	Al	0	0.061	0.00921
3	Cr	0	0.003	0.00448
4	Fe	1/2	0.220	0.00445
5	Al	1/2	0.693	0.00921
6	Cr	1/2	0.087	0.00448

TABLE 5.24 : Site occupation determined for sample 57C ($Fe_{57.5}Al_{37.5}Cr_5$) from synchrotron data at 7.097 keV (Fe edge) and 8.04 keV (Cu K_α)

Atom No.	Atom type	Position	Fraction	U_{iso}
1	Fe	0	0.859	0.00453
2	Al	0	0.103	0.00938
3	Cr	0	0.038	0.00487
4	Fe	1/2	0.297	0.00453
5	Al	1/2	0.651	0.00938
6	Cr	1/2	0.052	0.00487

TABLE 5.25 : Site occupation determined for sample 57C ($Fe_{57.5}Al_{37.5}Cr_5$) from synchrotron data at 5.974 (Cr edge) and 8.04 keV (Cu K_α)

Atom No.	Atom type	Position	Fraction	U_{iso}
1	Fe	0	0.950	0.00291
2	Al	0	0.113	0.00602
3	Cr	0	-0.063	0.00313
4	Fe	1/2	0.206	0.00291
5	Al	1/2	0.641	0.00602
6	Cr	1/2	0.153	0.00313

TABLE 5.26 : Site occupation determined for sample 57C ($Fe_{57.5}Al_{37.5}Cr_5$) from synchrotron data at all the three wavelengths

Atom No.	Atom type	Position	Fraction	U_{iso}
1	Fe	0	0.924	0.00438
2	Al	0	0.077	0.00907
3	Cr	0	-0.001	0.00471
4	Fe	1/2	0.232	0.00438
5	Al	1/2	0.678	0.00907
6	Cr	1/2	0.091	0.00471

TABLE 5.27 : Site occupation for Al determined for sample 55C ($Fe_{55}Al_{40}Cr_5$) from x-ray data at 8.04 keV (Cu K_α) where Fe and Cr have similar atomic scattering factors

Atom No.	Atom type	Position	Fraction	U_{iso}	Fraction	Uiso
1	Fe	0	0.980	-0.00228	0.908	-0.00228
2	Al	0	0.020	-0.00469	0.009	-0.00469
3	Cr	0	0.000 fixed	-0.00242	0.083 fixed	-0.00242
4	Fe	1/2	0.134	-0.00228	0.206	-0.00228
5	Al	1/2	0.783	-0.00469	0.794	-0.00469
6	Cr	1/2	0.083 fixed	-0.00242	0.000 fixed	-0.00242
			$\chi 2 = 0.027$		$\chi 2 = 0.028$	

TABLE 5.28 : Site occupation for Fe and Cr determined for sample 55C ($Fe_{55}Al_{40}Cr_5$) from synchrotron data at 5.974 keV (Cr edge) with Al atomic positions fixed from mean of Cu K_α results (Table 5.27)

Atom No.	Atom type	Position	Fraction	U_{iso}
1	Fe	0	0.971	0.00245
2	**Al**	0	0.015 **(fixed)**	0.00508
3	Cr	0	0.014	0.00263
4	Fe	1/2	0.142	0.00245
5	**Al**	1/2	0.789 **(fixed)**	0.00508
6	Cr	1/2	0.069	0.00263

$\chi 2 = 0.077$

TABLE 5.29 : Site occupation for Fe and Cr determined for sample 55C ($Fe_{55}Al_{40}Cr_5$) from synchrotron data at 7.097 keV (Fe edge) with Al atomic positions fixed from mean of Cu K_α results (Table 5.27)

Atom No.	Atom type	Position	Fraction	U_{iso}
1	Fe	0	1.028	0.00468
2	**Al**	0	0.015 **(fixed)**	0.00970
3	Cr	0	-0.043	0.00503
4	Fe	1/2	0.085	0.00468
5	**Al**	1/2	0.789 **(fixed)**	0.00970
6	Cr	1/2	0.126	0.00503

$\chi 2 = 0.013$

TABLE 5.30 : Site occupation for Fe and Cr determined for sample 55C ($Fe_{55}Al_{40}Cr_5$) from synchrotron data at 7.097 keV (Fe edge) and 5.974 keV (Cr edge) with Al atomic positions fixed from mean of Cu K_α results (Table 5.27)

Atom No.	Atom type	Position	Fraction	U_{iso}
1	Fe	0	0.984	0.00402
2	Al	0	0.015 (fixed)	0.00835
3	Cr	0	0.002	0.00433
4	Fe	1/2	0.130	0.00402
5	Al	1/2	0.789 (fixed)	0.00835
6	Cr	1/2	0.082	0.00433

$\chi 2 = 0.163$

TABLE 5.31 : Site occupation determined for sample 55C ($Fe_{55}Al_{40}Cr_5$) from synchrotron data at 7.097 keV (Fe edge) and 5.974 keV (Cr edge)

Atom No.	Atom type	Position	Fraction	U_{iso}
1	Fe	0	0.968	0.00443
2	Al	0	0.037	0.00919
3	Cr	0	-0.005	0.00476
4	Fe	1/2	0.145	0.00445
5	Al	1/2	0.766	0.00919
6	Cr	1/2	0.086	0.00476

$\chi 2 = 0.087$

TABLE 5.32 : Site occupation determined for sample 55C ($Fe_{55}Al_{40}Cr_5$) from synchrotron data at 7.097 keV (Fe edge) and 8.04 keV (Cu K_α)

Atom No.	Atom type	Position	Fraction	U_{iso}
1	Fe	0	0.941	0.00462
2	Al	0	0.054	0.00959
3	Cr	0	0.006	0.00497
4	Fe	1/2	0.173	0.00462
5	Al	1/2	0.750	0.00959
6	Cr	1/2	0.078	0.00497

$\chi 2 = 0.080$

TABLE 5.33 : Site occupation determined for sample 55C ($Fe_{55}Al_{40}Cr_5$) from synchrotron data at 5.974 (Cr edge) and 8.04 keV (Cu K_α)

Atom No.	Atom type	Position	Fraction	U_{iso}
1	Fe	0	0.979	0.00173
2	Al	0	0.039	0.00359
3	Cr	0	-0.018	0.00187
4	Fe	1/2	0.134	0.00173
5	Al	1/2	0.764	0.00359
6	Cr	1/2	0.102	0.00187

$\chi 2 = 0.094$

TABLE 5.34 : Site occupation determined for sample 55C ($Fe_{55}Al_{40}Cr_5$) from synchrotron data at all the three wavelengths

Atom No.	Atom type	Position	Fraction	U_{iso}
1	Fe	0	0.964	0.00431
2	Al	0	0.043	0.00894
3	Cr	0	-0.006	0.00463
4	Fe	1/2	0.150	0.00431
5	Al	1/2	0.761	0.00894
6	Cr	1/2	0.089	0.00463

$\chi 2 = 0.112$

TABLE 5.35 : Site occupation for Al determined for sample 59C ($Fe_{59}Al_{36}Cr_5$) from x-ray data at 8.04 keV (Cu K_α) where Fe and Cr have similar atomic scattering factors

Atom No.	Atom type	Posi-tion	Fraction	U_{iso}	Fraction	Uiso
1	Fe	0	0.876	0.01493	0.801	0.01495
2	Al	0	0.124	0.03092	0.113	0.03096
3	Cr	0	0.000 fixed	0.01599	0.086 fixed	0.01602
4	Fe	1/2	0.314	0.01493	0.389	0.01495
5	Al	1/2	0.600	0.03092	0.611	0.03096
6	Cr	1/2	0.086 fixed	0.01599	0.000 fixed	0.01602

TABLE 5.36 : Comparision of site occupation and thermal parameter results for data corrected and uncorrected for granularity - sample 60 Cr edge

			Granularity corrected		Granularity uncorrected	
Atom No.	Atom type	Posi-tion	Fraction	U_{iso}	Fraction	Uiso
1	Fe	0	0.955	0.00509	0.956	0.00293
2	Al	0	0.045	0.01055	0.044	0.00607
3	Fe	1/2	0.245	0.00509	0.244	0.00293
4	Al	1/2	0.755	0.01055	0.756	0.00607

TABLE 5.37 : Lattice parameters of the alloys

Specimen composition	Lattice parameter (Å)
$Fe_{60}Al_{35}Cr_5$	2.8816
$Fe_{57.5}Al_{37.5}Cr_5$	2.8837
$Fe_{55}Al_{40}Cr_5$	2.8852
$Fe_{60}Al_{40}$	2.8922
$Fe_{55}Al_{45}$	2.8927
$Fe_{51}Al_{49}$	2.8976

TABLE 5.38 : Results of Hardness measurements on samples annealed at 1000°C for 1 hour.

Sample Composition	Microhardness (DPH)	S.D.
$Fe_{60}Al_{35}Cr_5$	301.3	1.2
$Fe_{59}Al_{36}Cr_5$	322.3	17.5
$Fe_{57.5}Al_{37.5}Cr_5$	361.3	16.9
$Fe_{55}Al_{40}Cr_5$	392.6	29.8
$Fe_{51}Al_{46}Cr_3$	528.5	11.5
$Fe_{60}Al_{40}$	378.7	7.3
$Fe_{55}Al_{45}$	478.4	9.7
$Fe_{51}Al_{49}$	585.9	29.8

TABLE 5.39 : Results of Hardness measurements on samples annealed at 400°C for 5 days.

Sample Composition	Microhardness (DPH)	S.D.
$Fe_{60}Al_{35}Cr_5$	273.4	11.6
$Fe_{59}Al_{36}Cr_5$	264.2	5.1
$Fe_{57.5}Al_{37.5}Cr_5$	265.2	6.4
$Fe_{55}Al_{40}Cr_5$	274.4	8.9
$Fe_{60}Al_{40}$	277.7	18.8
$Fe_{55}Al_{45}$	252.3	8.1
$Fe_{51}Al_{49}$	525.6	18.4

TABLE 5.40 : Mean value of site occupancies for $Fe_{60}Al_{40}$

Atom No.	Atom type	Position	Fraction
1	Fe	0	0.948(7)
2	Al	0	0.052(7)
3	Fe	1/2	0.252(7)
4	Al	1/2	0.748(7)

TABLE 5.41 : Mean value of site occupancies for $Fe_{55}Al_{45}$

Atom No.	Atom type	Position	Fraction
1	Fe	0	0.936(2)
2	Al	0	0.064(2)
3	Fe	1/2	0.164(2)
4	Al	1/2	0.836(2)

TABLE 5.42 : Mean value of site occupancies for $Fe_{51}Al_{49}$

Atom No.	Atom type	Position	Fraction
1	Fe	0	0.955(15)
2	Al	0	0.045(15)
3	Fe	1/2	0.065(15)
4	Al	1/2	0.935(15)

TABLE 5.43 : Mean value of site occupancies for $Fe_{60}Al_{35}Cr_5$

Atom No.	Atom type	Position	Fraction
1	Fe	0	0.988(15)
2	Al	0	0.011 (5)
3	Cr	0	0.001 (1)
4	Fe	1/2	0.223(15)
5	Al	1/2	0.696 (5)
6	Cr	1/2	0.081 (1)

TABLE 5.44 : Mean value of site occupancies for $Fe_{57.5}Al_{37.5}Cr_5$

Atom No.	Atom type	Position	Fraction
1	Fe	0	0.923 (60)
2	Al	0	0.077 (26)
3	Cr	0	0.000 (1)
4	Fe	1/2	0.233 (60)
5	Al	1/2	0.677 (26)
6	Cr	1/2	0.090 (1)

TABLE 5.45 : Mean value of site occupancies for $Fe_{55}Al_{40}Cr_5$

Atom No.	Atom type	Position	Fraction
1	Fe	0	0.958 (20)
2	Al	0	0.042 (11)
3	Cr	0	0.000 (5)
4	Fe	1/2	0.152 (20)
5	Al	1/2	0.762 (11)
6	Cr	1/2	0.083 (5)

TABLE 5.46 : Mean value of site occupancies for $Fe_{59}Al_{36}Cr_5$

Atom No.	Atom type	Position	Fraction
1	Fe	0	xxxx
2	Al	0	0.118 (11)
3	Cr	0	xxxx
4	Fe	1/2	xxxx
5	Al	1/2	0.606 (11)
6	Cr	1/2	xxxx

TABLE 5.47: Comparision of site occupation results obtained from Rietveld analysis and Atom probe for $Fe_{57.5}Al_{37.5}Cr_5$

Atom type	Position	Rietveld analysis Fraction	Atom probe Fraction
Fe	0	0.923±0.060	0.915±0.119
Al	0	0.077±0.026	0.139±0.071
Cr	0	0.000±0.001	0.015±0.003
Fe	1/2	0.233±0.060	0.240±0.119
Al	1/2	0.677±0.026	0.617±0.071
Cr	1/2	0.009±0.001	0.075±0.003

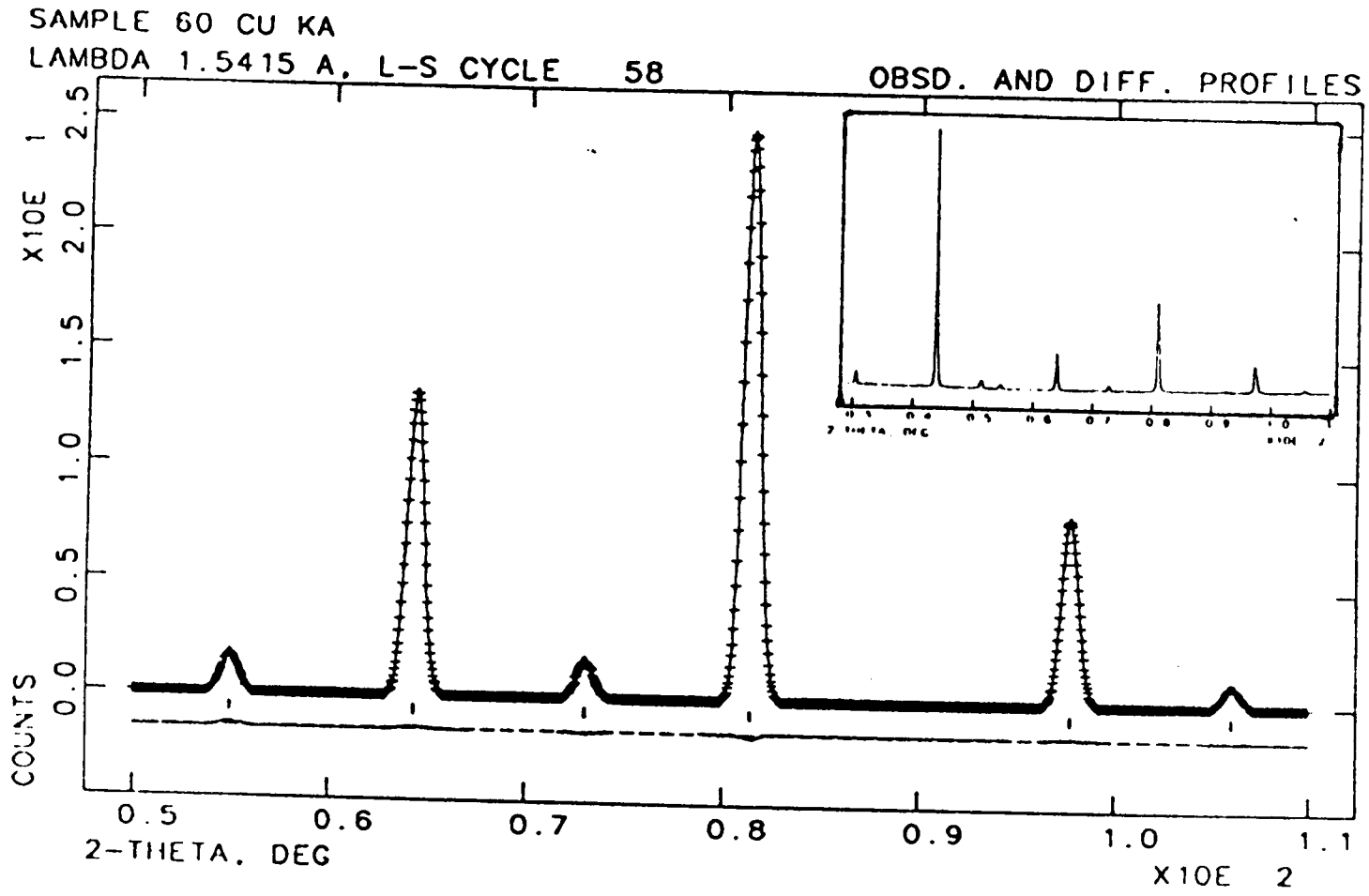

Figure 5.1 Rietveld fit (—) to constructed profile (+), and the difference profile (--) for sample $Fe_{60}Al_{40}$ at Cu K_α. Inset shows the observed diffraction profile.

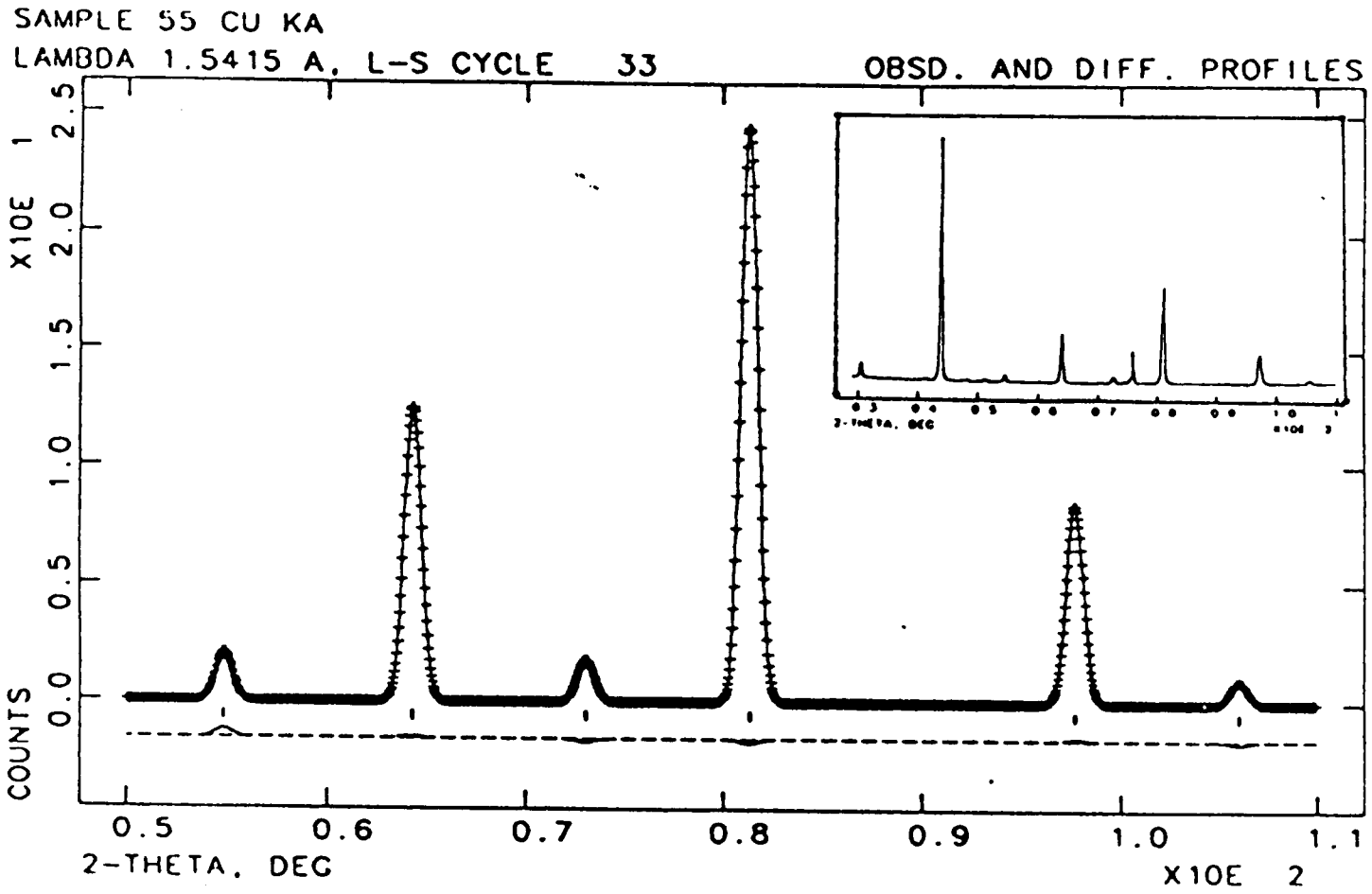

Figure 5.2 Rietveld fit (—) to constructed profile (+), and the difference profile (--) for sample $Fe_{55}Al_{45}$ at Cu K_α. Inset shows the observed diffraction profile.

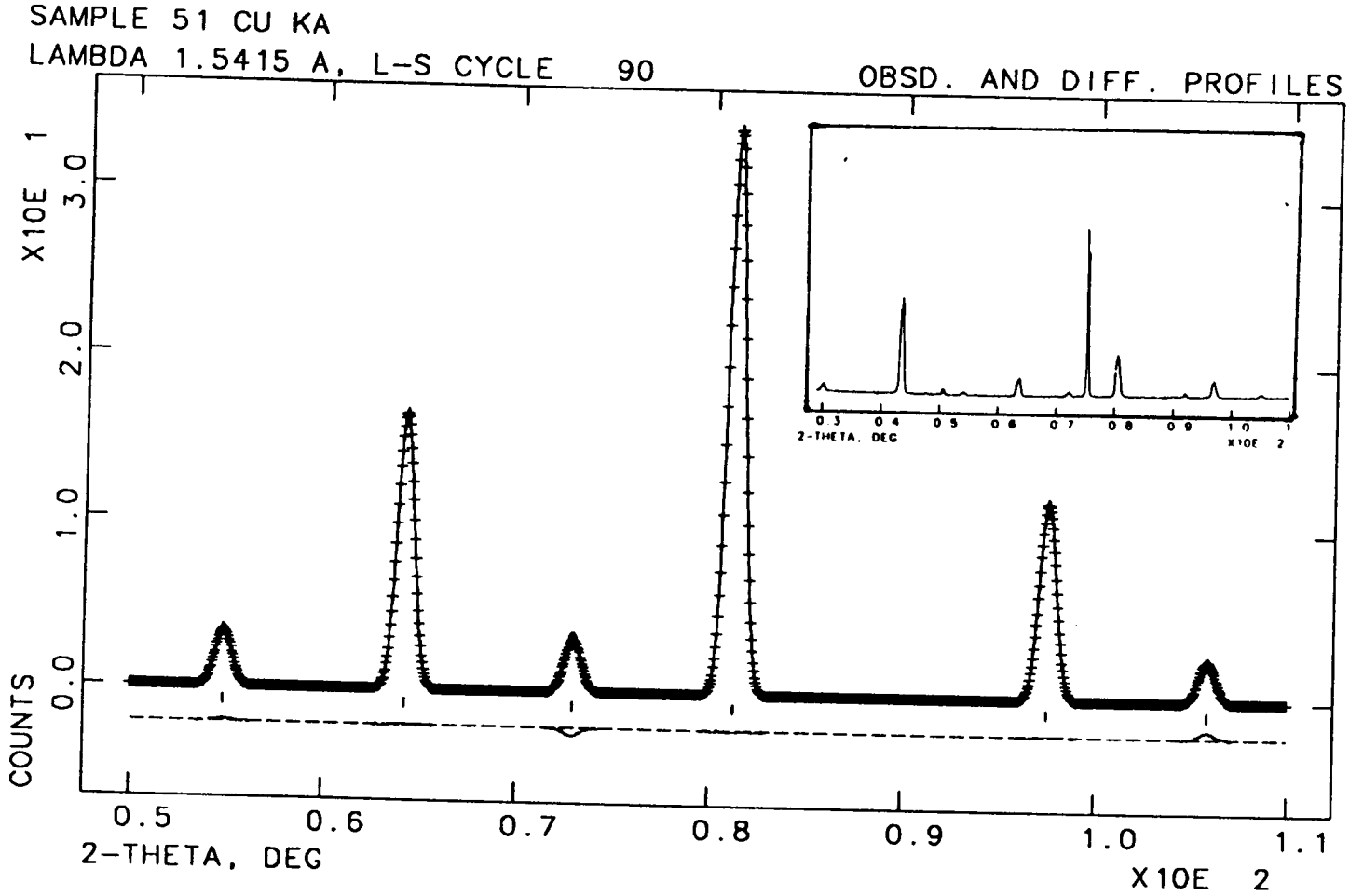

Figure 5.3 Rietveld fit (—) to constructed profile (+), and the difference profile (--) for sample $Fe_{51}Al_{49}$ at Cu K_α. Inset shows the observed diffraction profile.

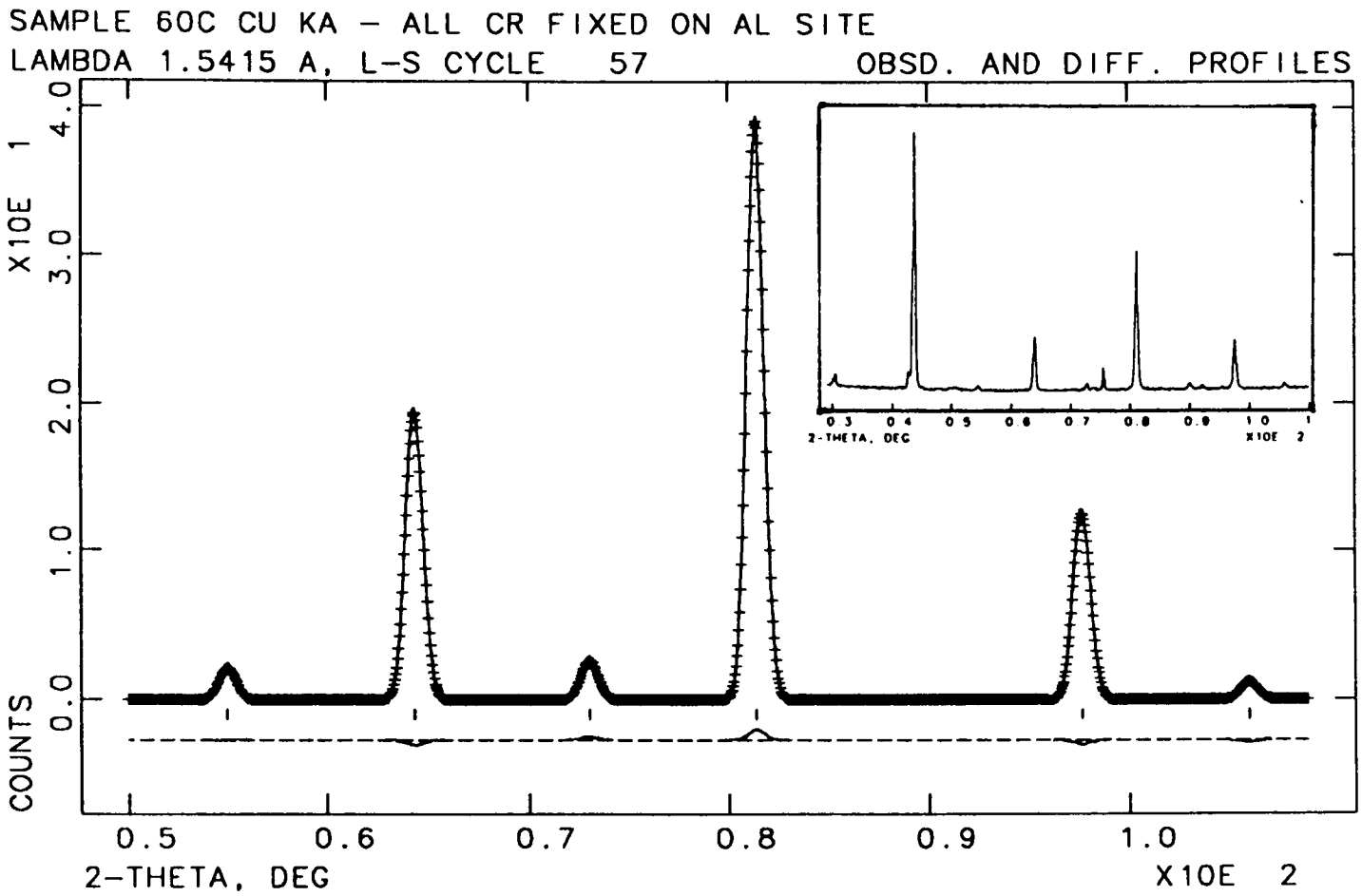

Figure 5.4 Rietveld fit (—) to constructed profile (+), and the difference profile (--) for sample $Fe_{60}Al_{35}Cr_5$ at Cu K_α. Inset shows the observed diffraction profile.

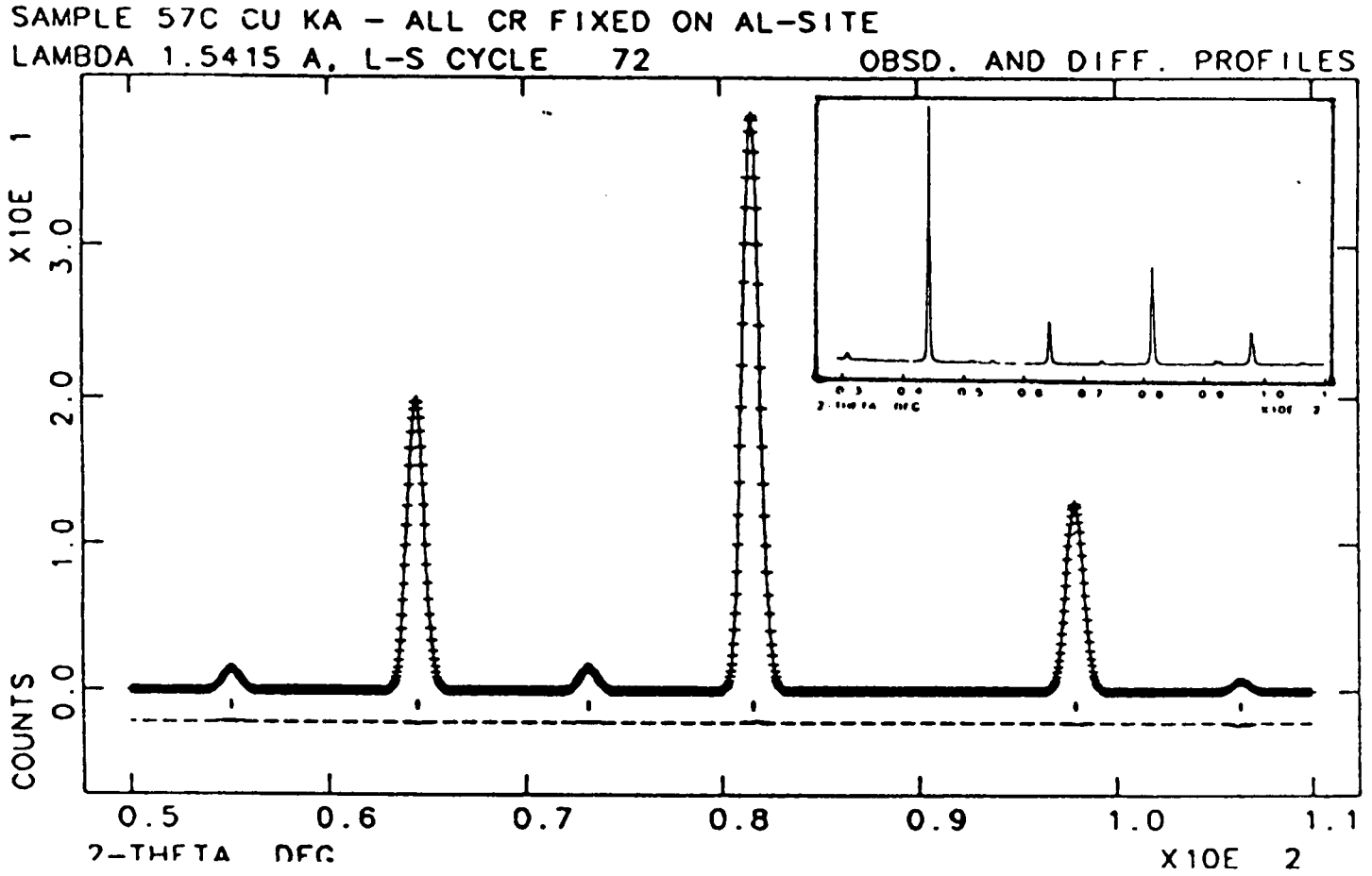

Figure 5.5 Rietveld fit (—) to constructed profile (+), and the difference profile (--) for sample $Fe_{57.5}Al_{37.5}Cr_5$ at Cu K_α. Inset shows the observed diffraction profile.

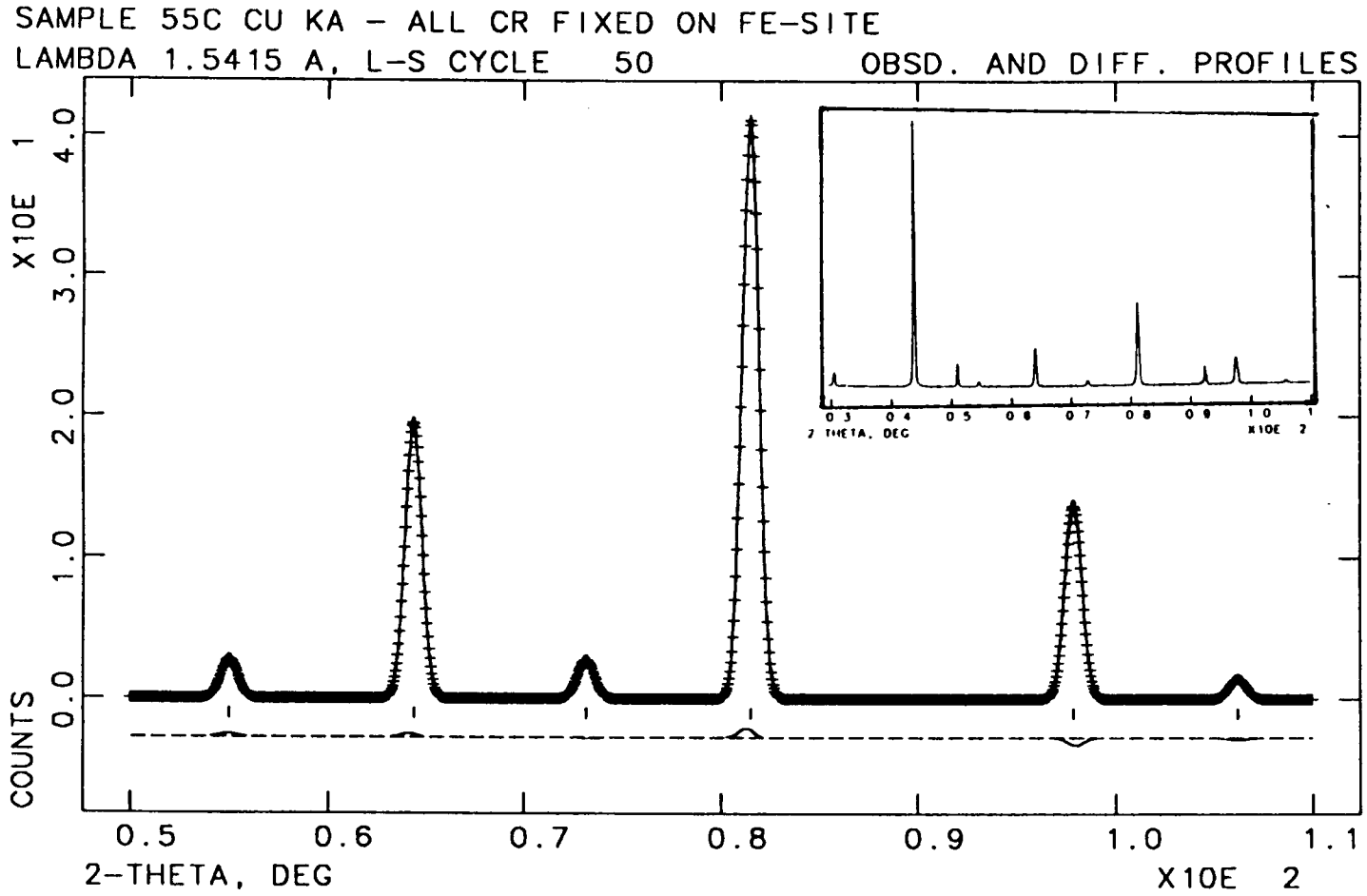

Figure 5.6 Rietveld fit (—) to constructed profile (+), and the difference profile (--) for sample $Fe_{55}Al_{40}Cr_5$ at Cu K_α. Inset shows the observed diffraction profile.

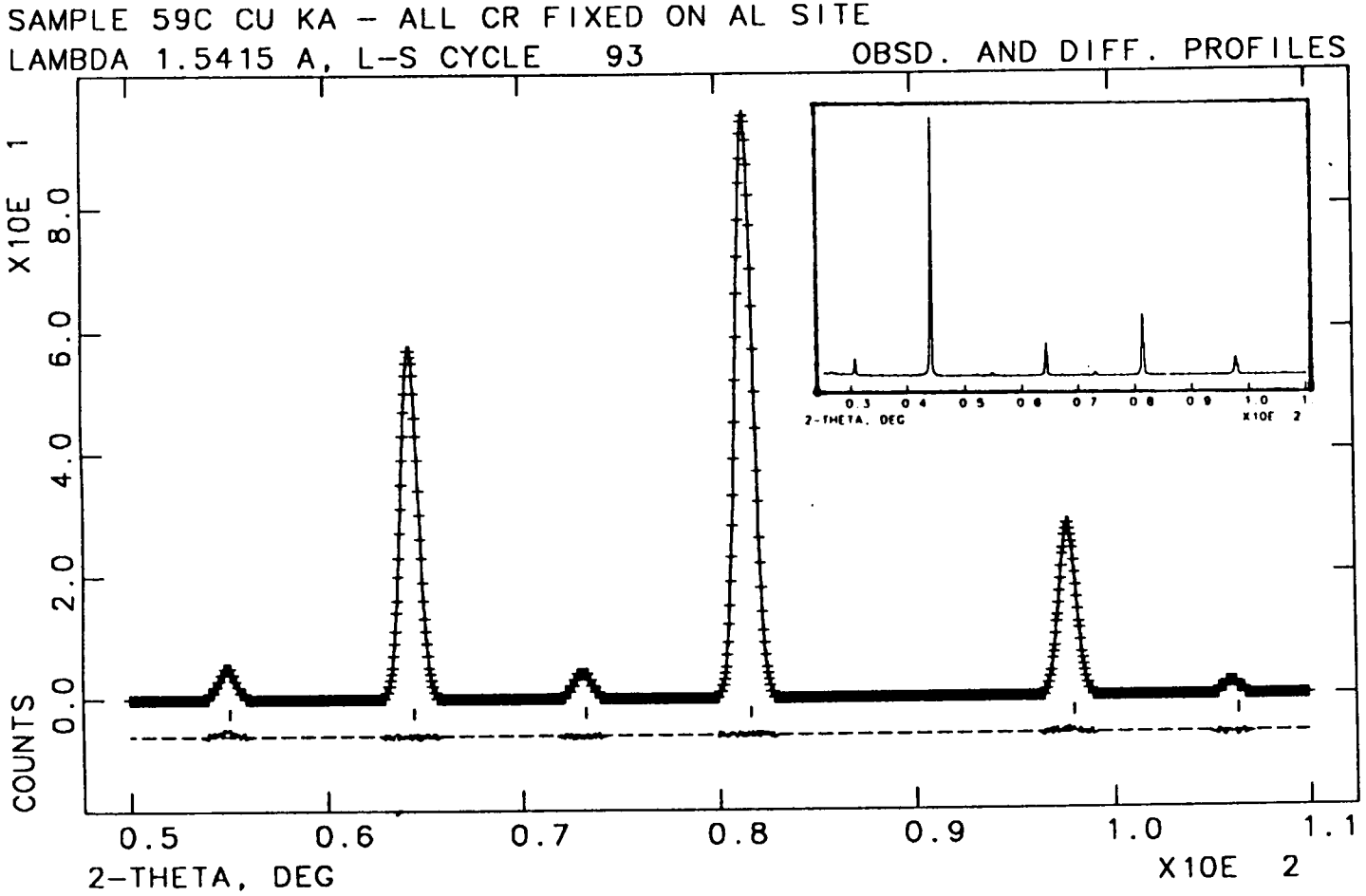

Figure 5.7 Rietveld fit (—) to constructed profile (+), and the difference profile (--) for sample $Fe_{59}Al_{36}Cr_5$ at Cu K_α. Inset shows the observed diffraction profile.

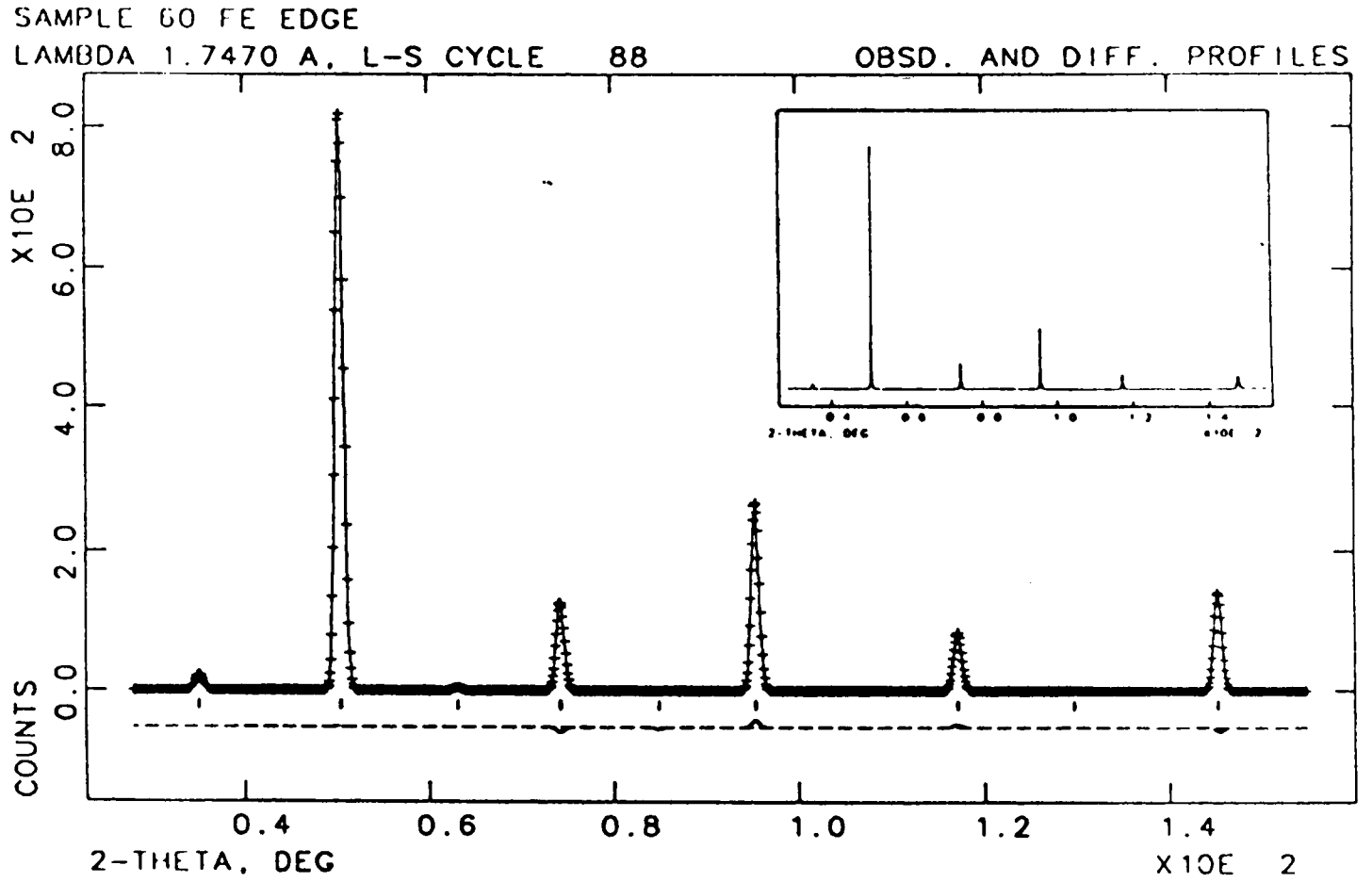

Figure 5.8 Rietveld fit (—) to constructed profile (+), and the difference profile (--) for sample $Fe_{60}Al_{40}$ near Fe edge. Inset shows the observed diffraction profile.

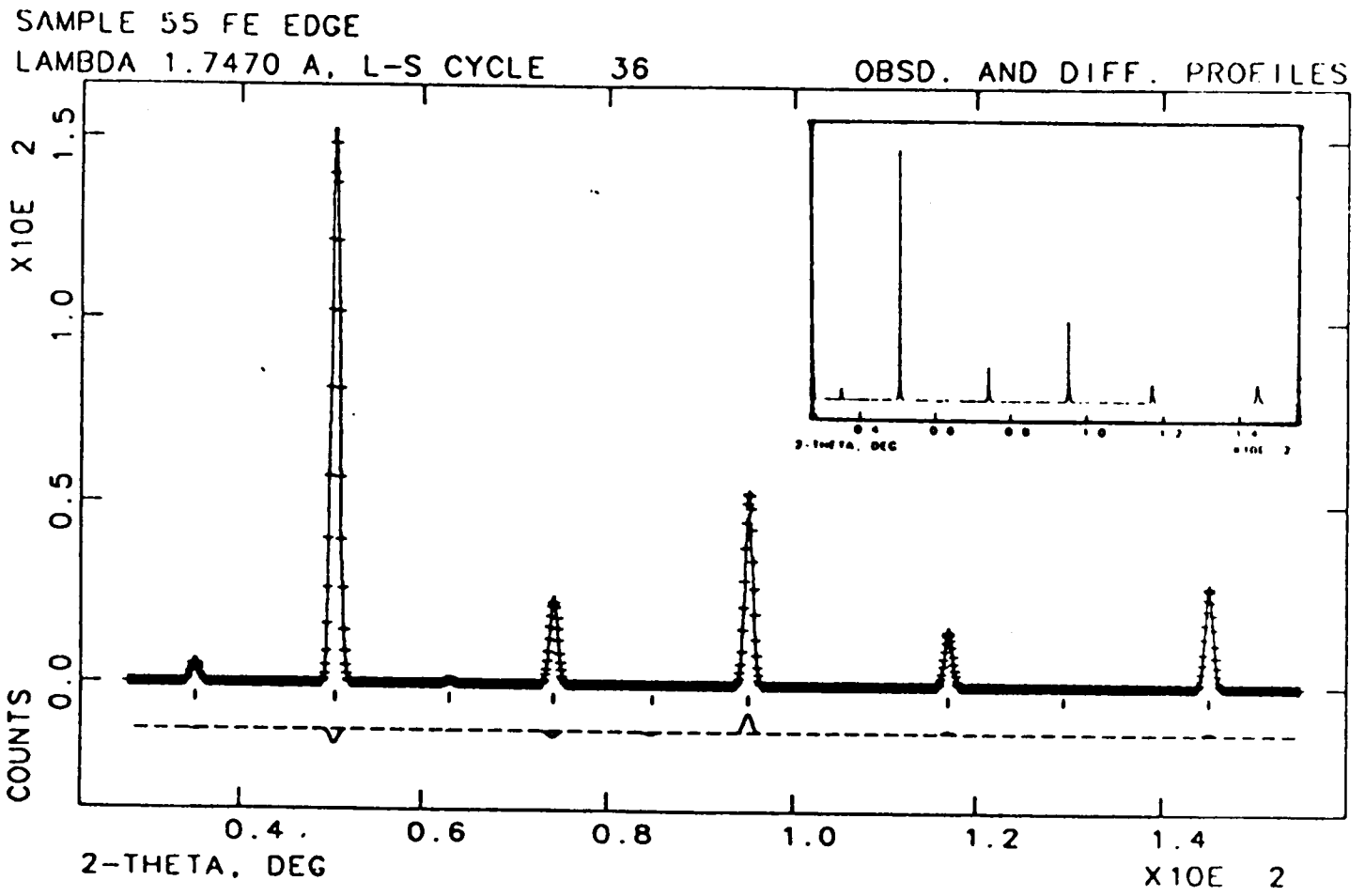

Figure 5.9 Rietveld fit (—) to constructed profile (+), and the difference profile (--) for sample $Fe_{55}Al_{45}$ near Fe edge. Inset shows the observed diffraction profile.

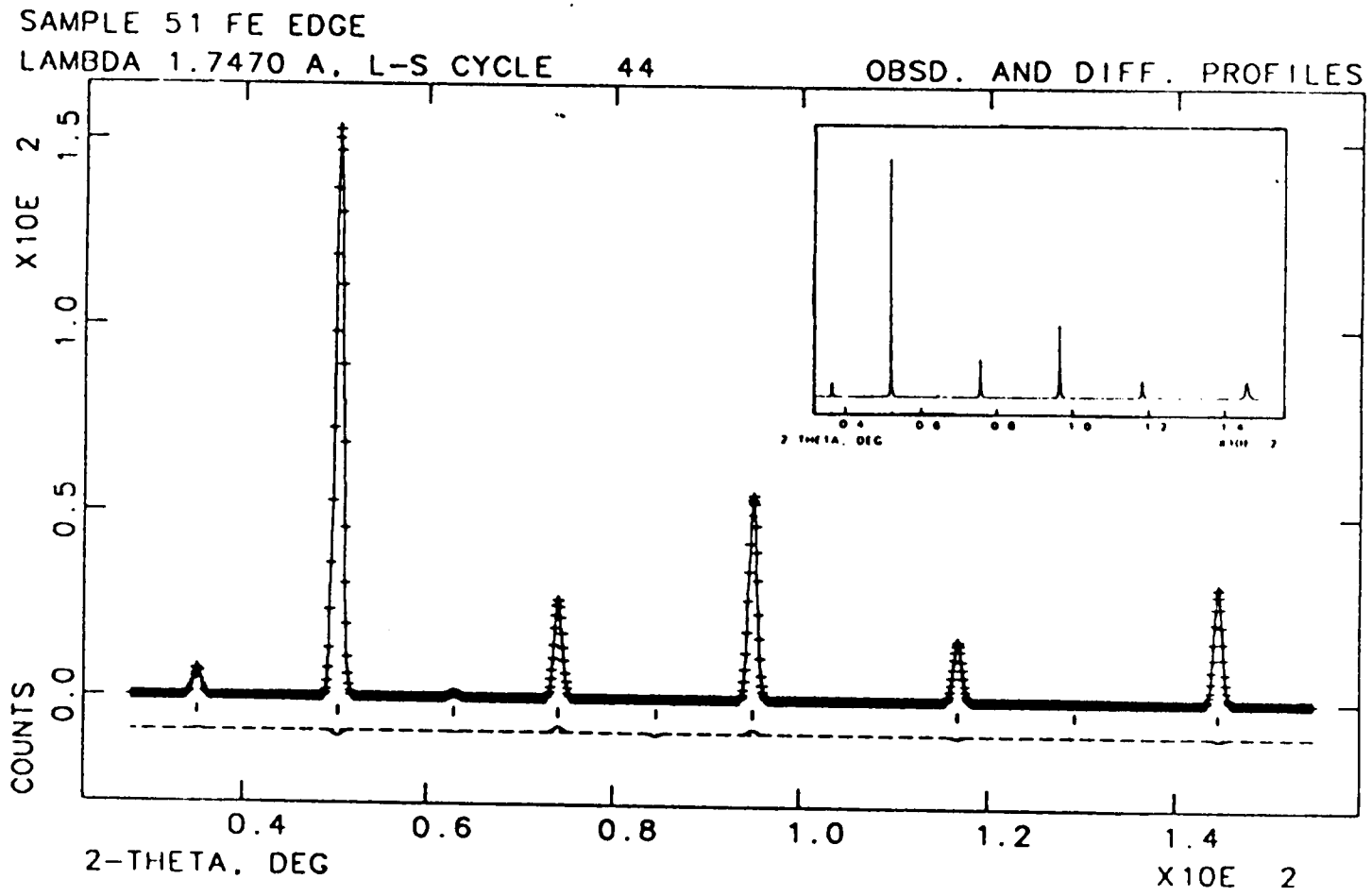

Figure 5.10 Rietveld fit (—) to constructed profile (+), and the difference profile (--) for sample $Fe_{51}Al_{49}$ near Fe edge. Inset shows the observed diffraction profile.

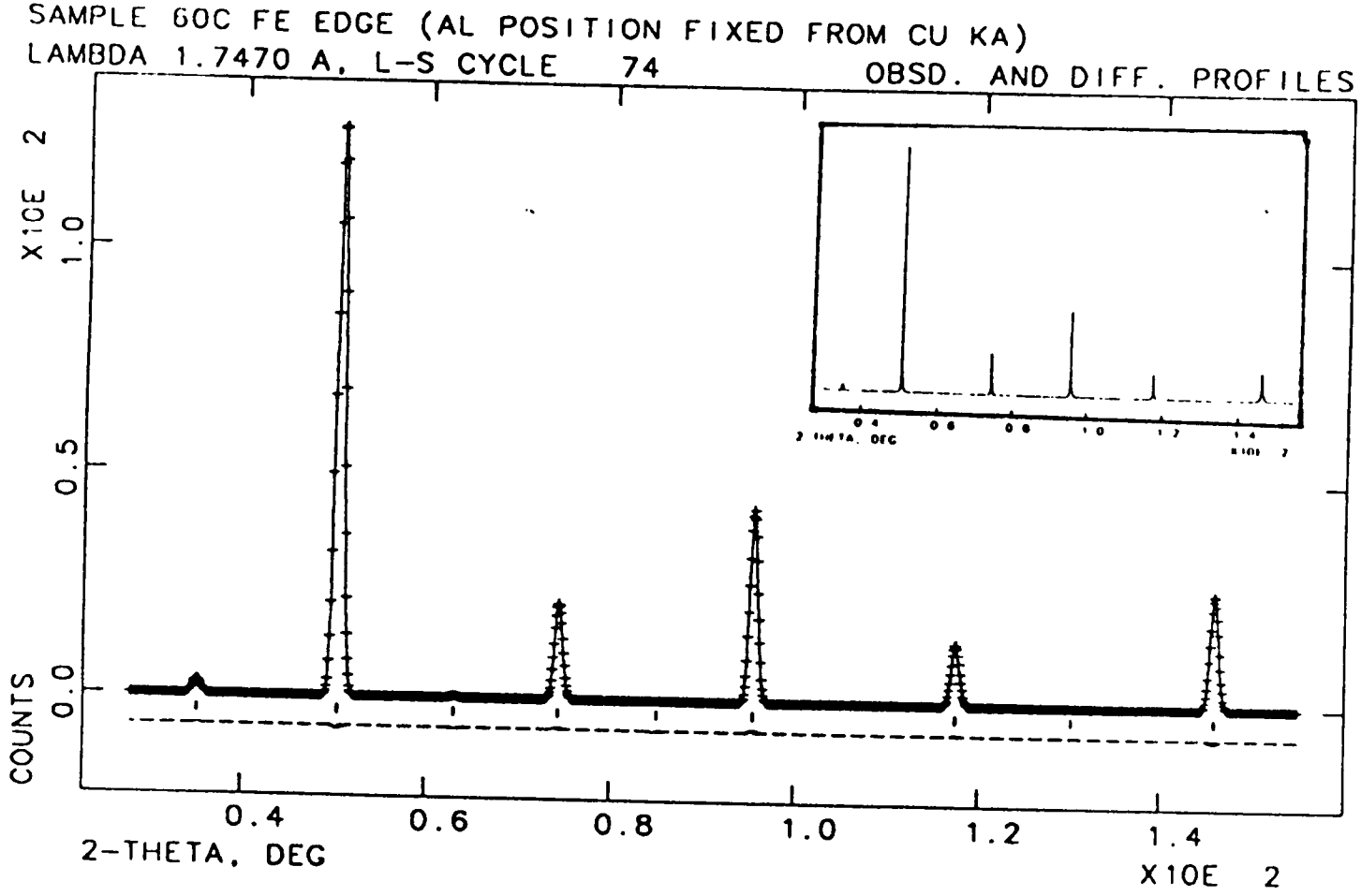

Figure 5.11 Rietveld fit (—) to constructed profile (+), and the difference profile (--) for sample $Fe_{60}Al_{35}Cr_5$ near Fe edge. Inset shows the observed diffraction profile.

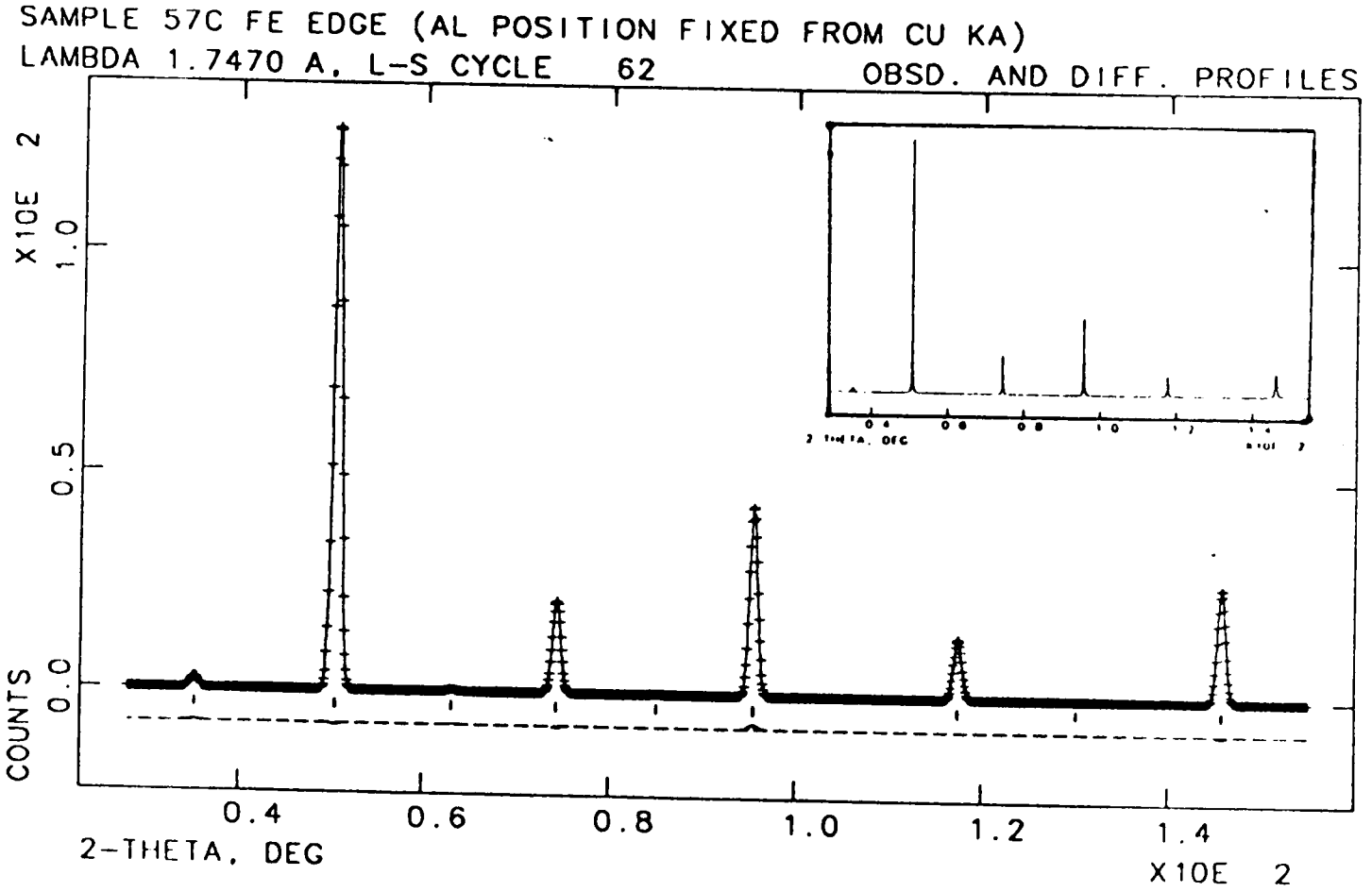

Figure 5.12 Rietveld fit (—) to constructed profile (+), and the difference profile (--) for sample $Fe_{57.5}Al_{37.5}Cr_5$ near Fe edge. Inset shows the observed diffraction profile.

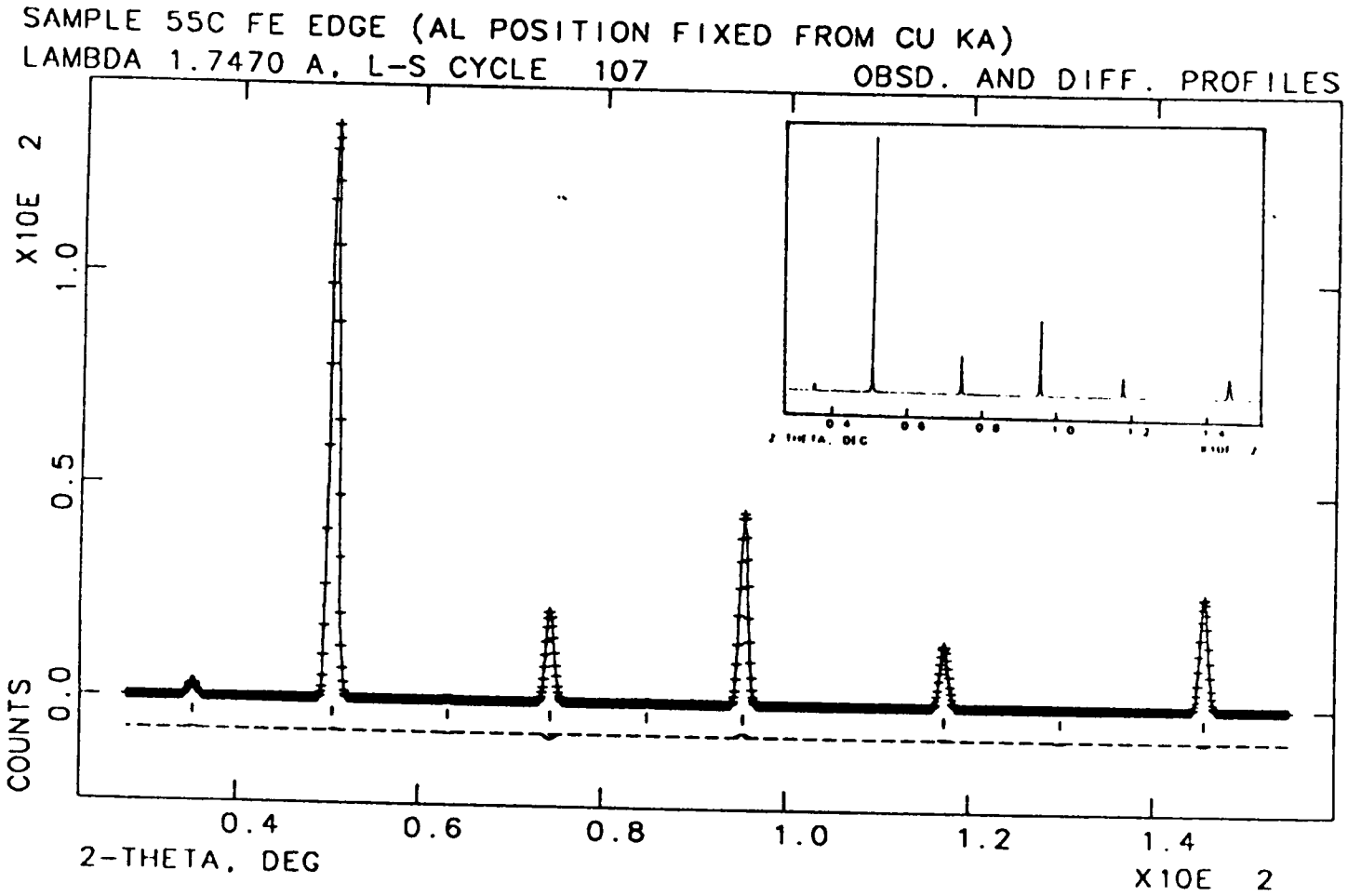

Figure 5.13 Rietveld fit (—) to constructed profile (+), and the difference profile (--) for sample $Fe_{55}Al_{40}Cr_5$ near Fe edge. Inset shows the observed diffraction profile.

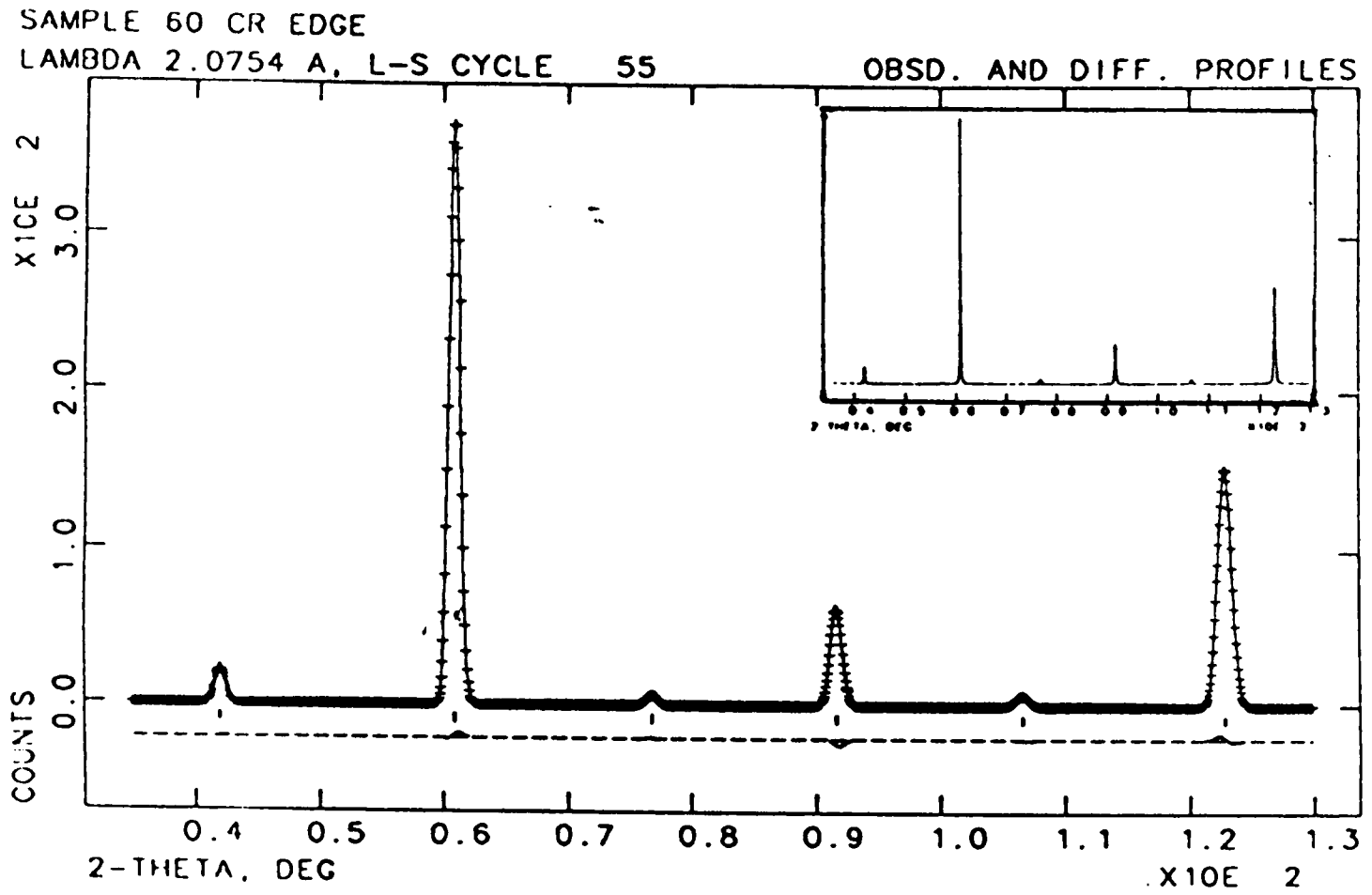

Figure 5.14 Rietveld fit (—) to constructed profile (+), and the difference profile (--) for sample $Fe_{60}Al_{40}$ near Cr edge. Inset shows the observed diffraction profile.

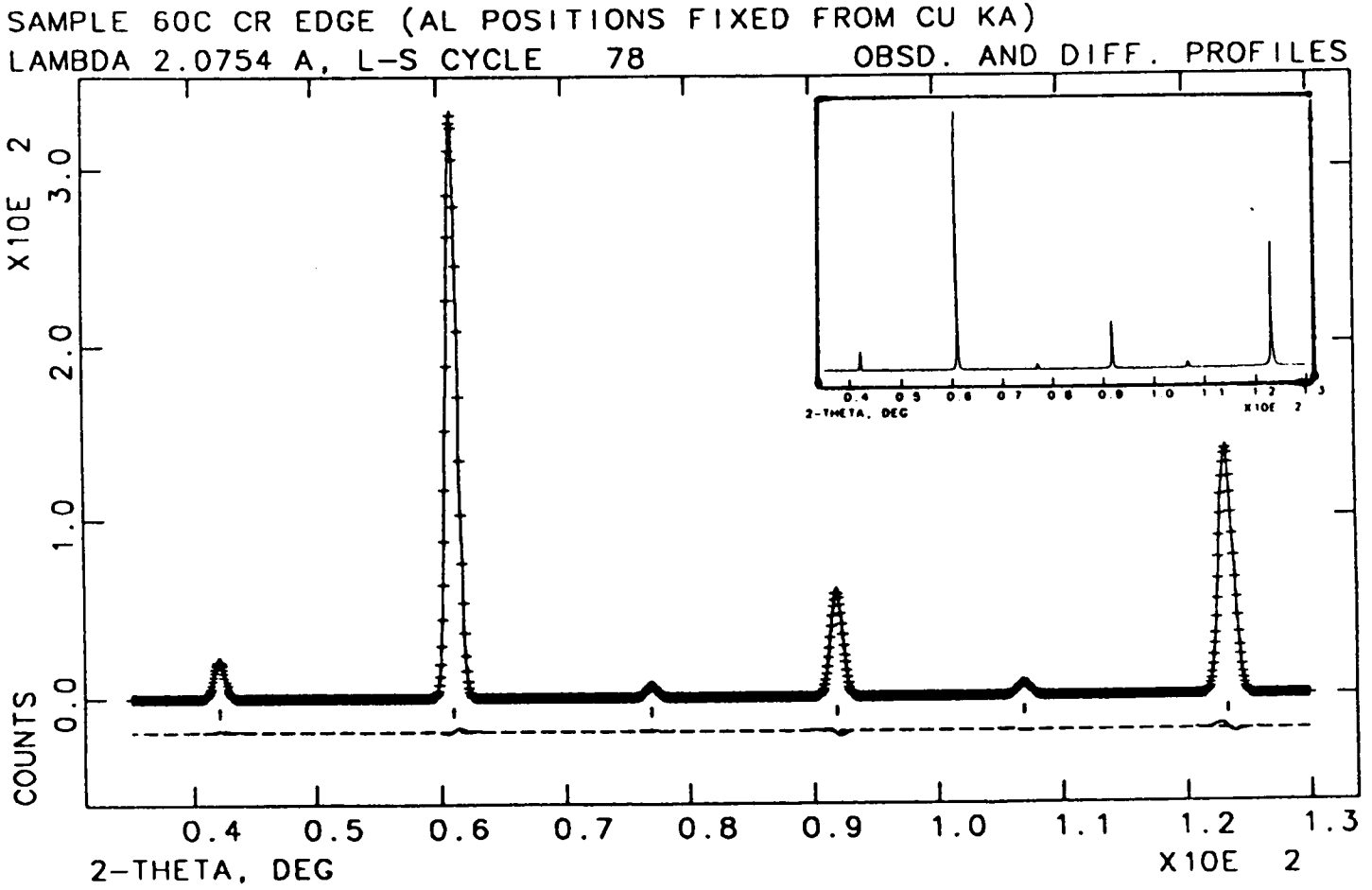

Figure 5.15 Rietveld fit (—) to constructed profile (+), and the difference profile (--) for sample $Fe_{60}Al_{35}Cr_5$ near Cr edge. Inset shows the observed diffraction profile.

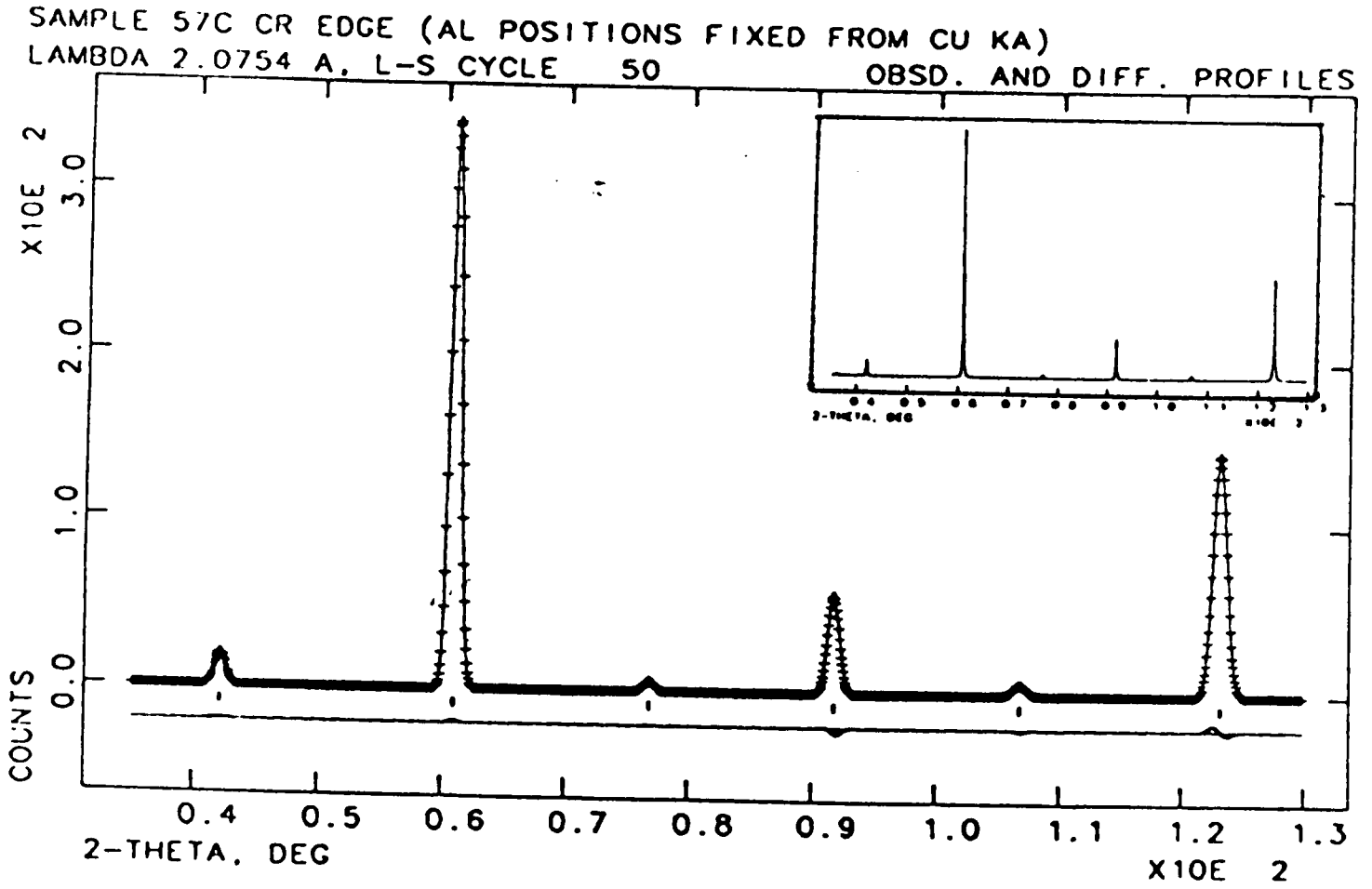

Figure 5.16 Rietveld fit (—) to constructed profile (+), and the difference profile (--) for sample $Fe_{57.5}Al_{37.5}Cr_5$ near Cr edge. Inset shows the observed diffraction profile.

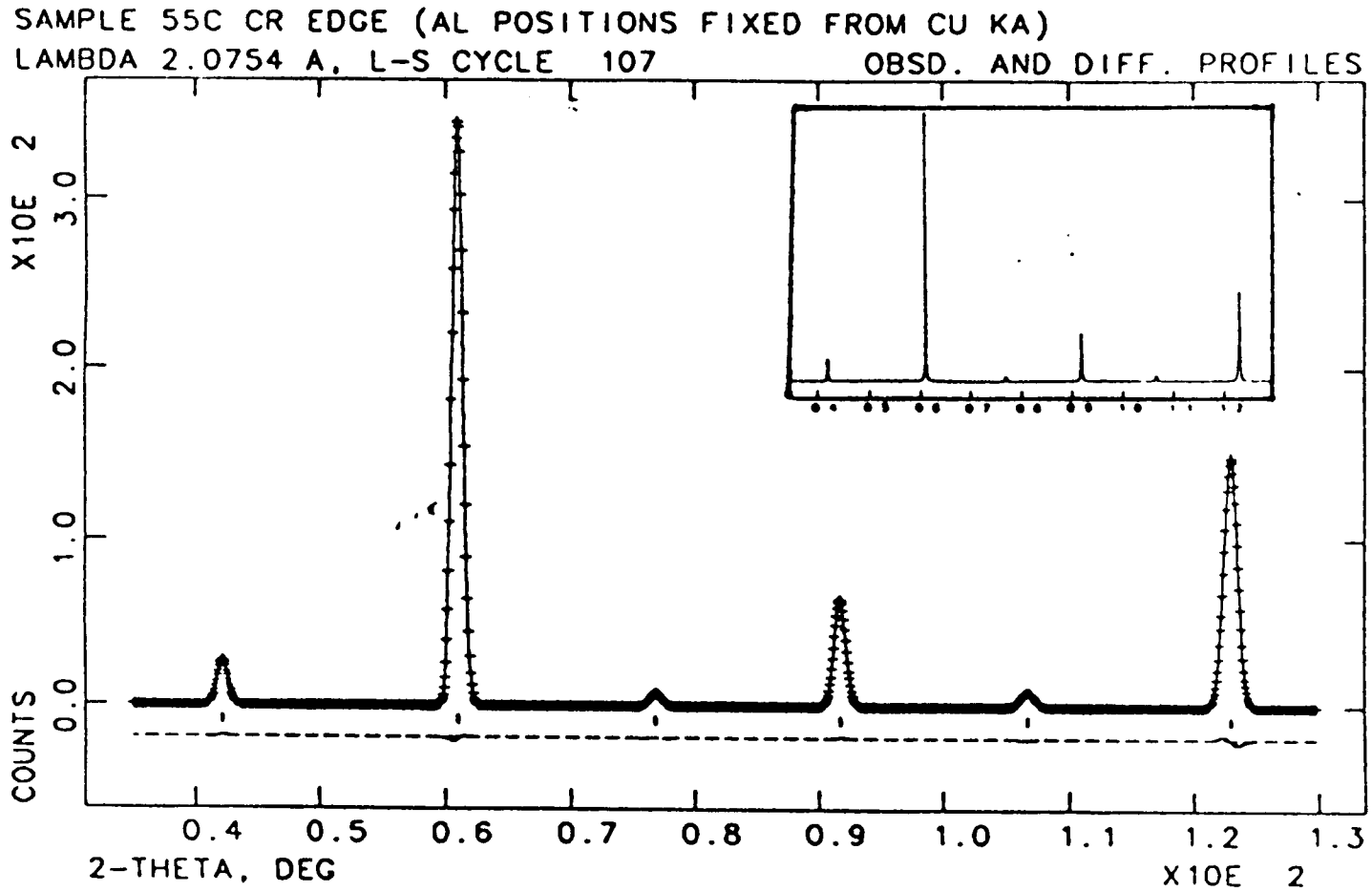

Figure 5.17 Rietveld fit (—) to constructed profile (+), and the difference profile (--) for sample $Fe_{55}Al_{40}Cr_5$ near Cr edge. Inset shows the observed diffraction profile.

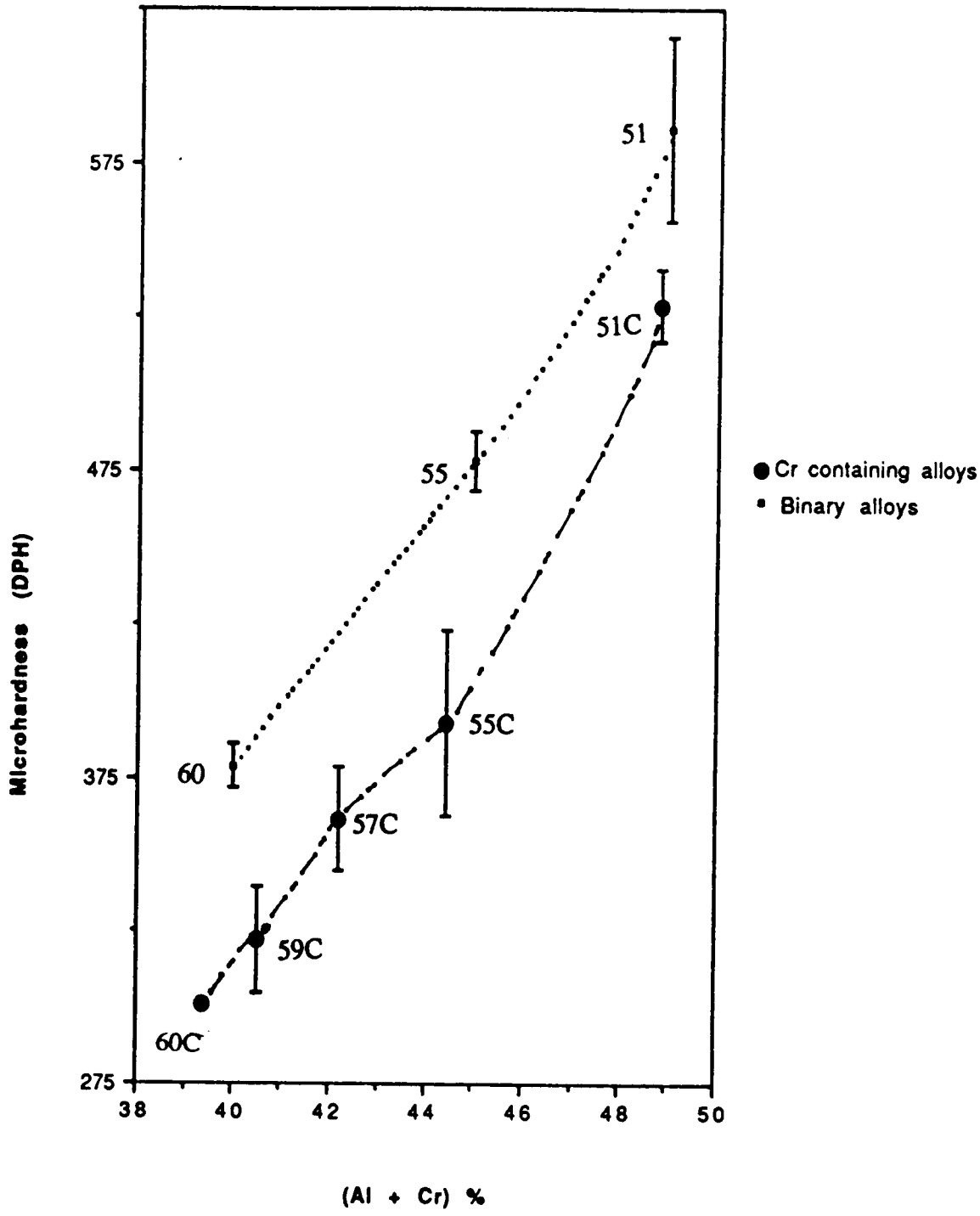

Figure 5.18 Microhardness vs (Al + Cr) conc. for specimens annealed at 1000°C (1 hour)

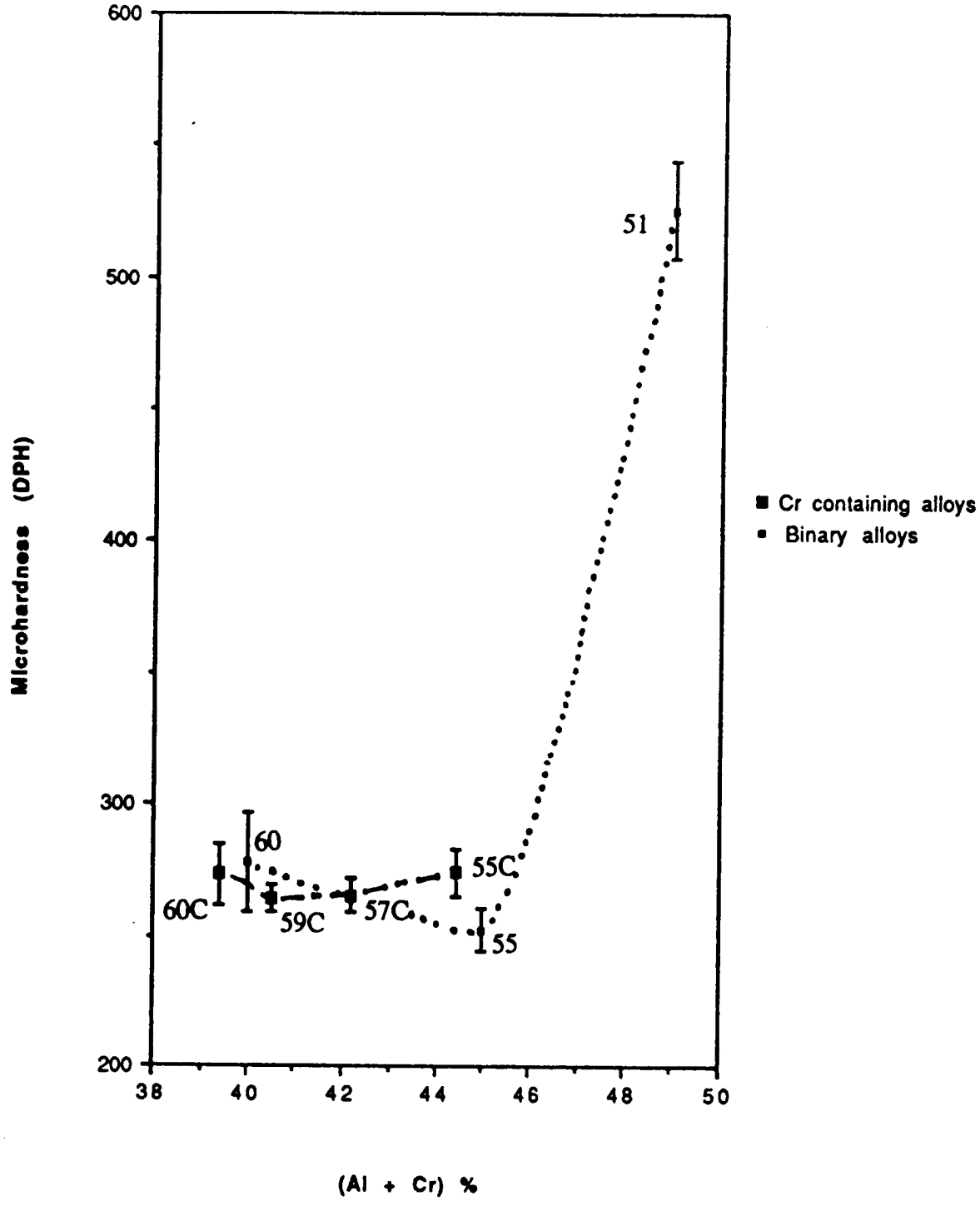

Figure 5.19 Microhardness vs (Al + Cr) conc. for specimens annealed at 400°C (5 days)

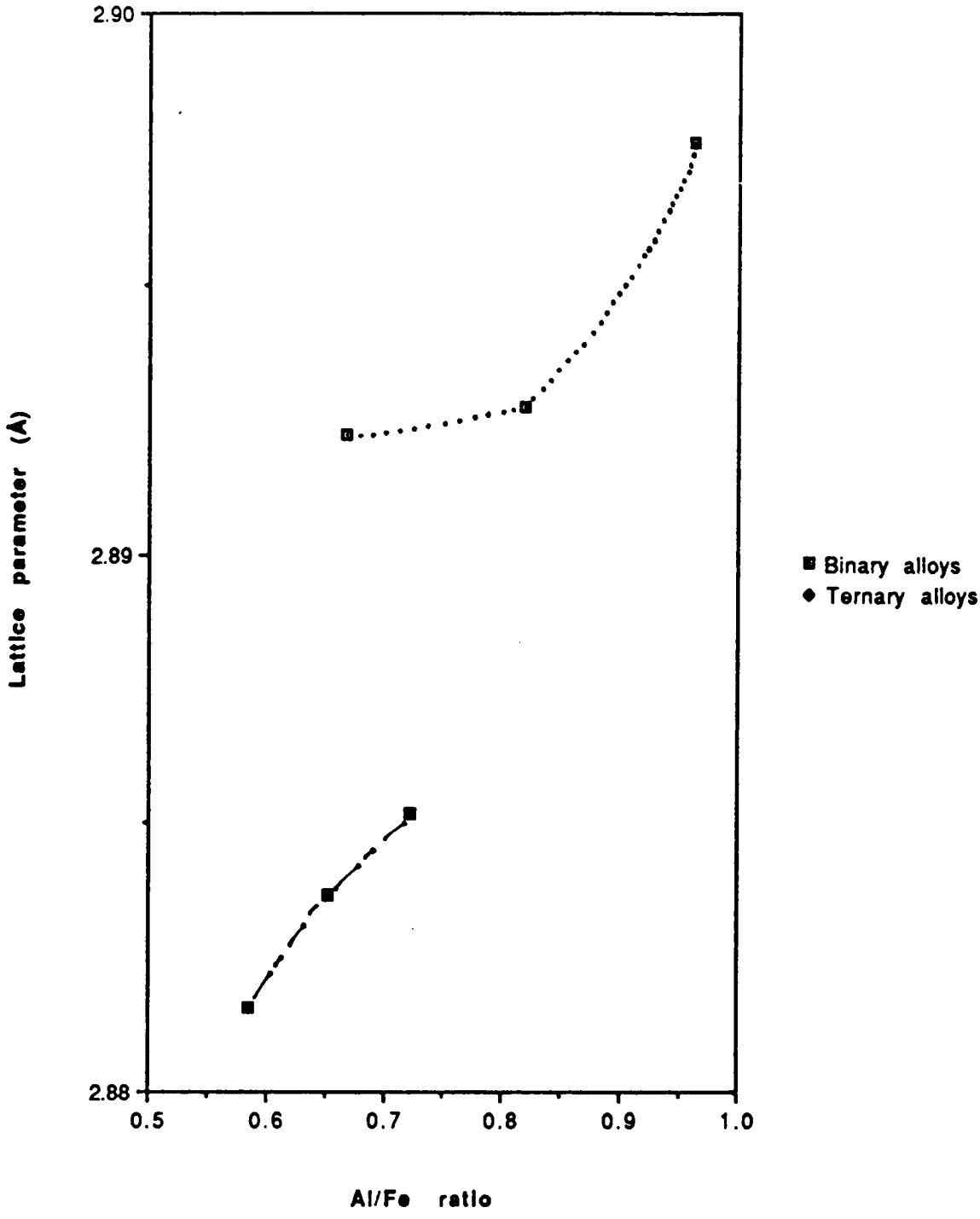

Figure 5.20 Lattice parameters of the alloys

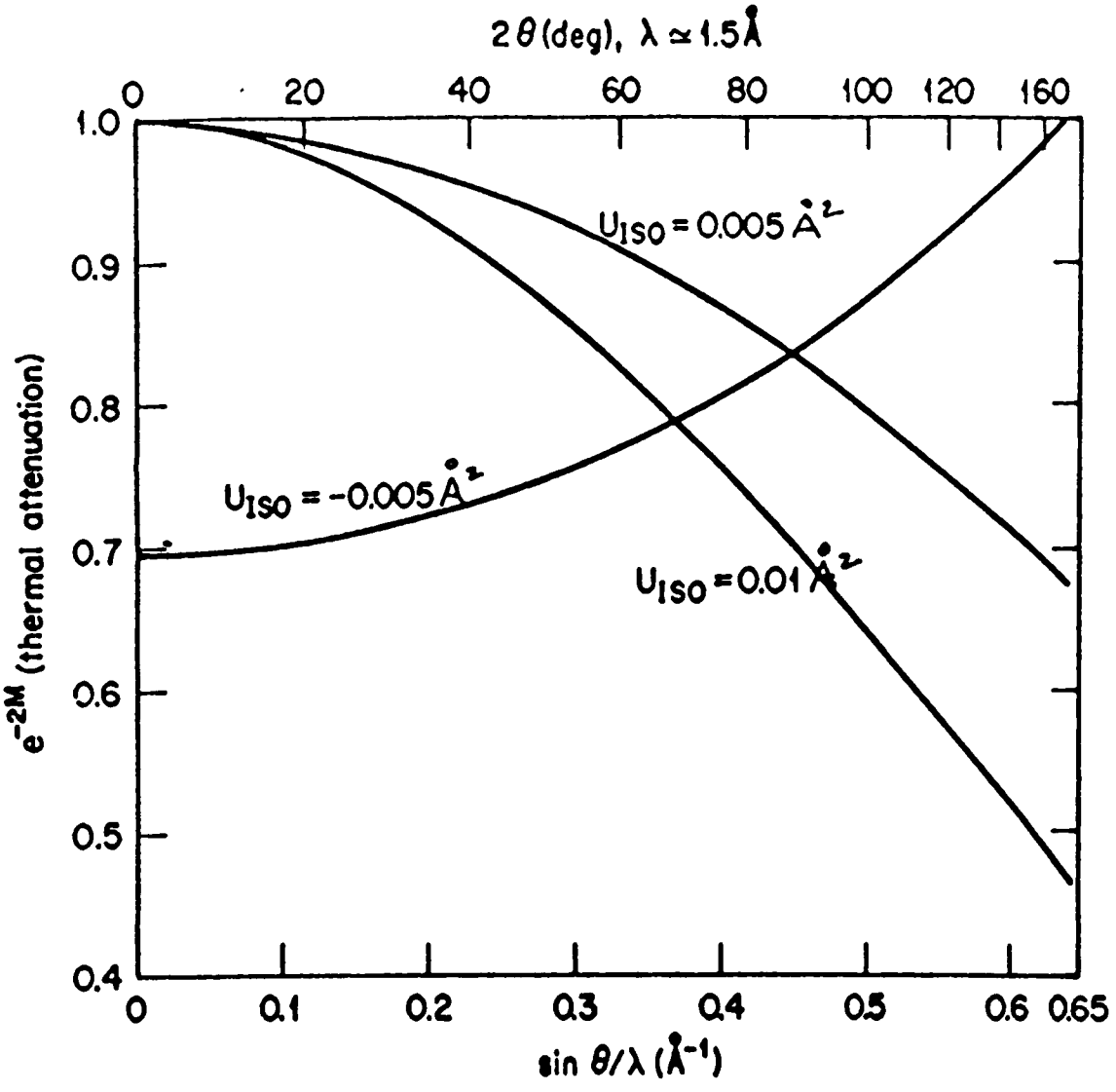

Figure 5.21 A negative thermal parameter would scale the observed intensity data to compensate for the granularity effect

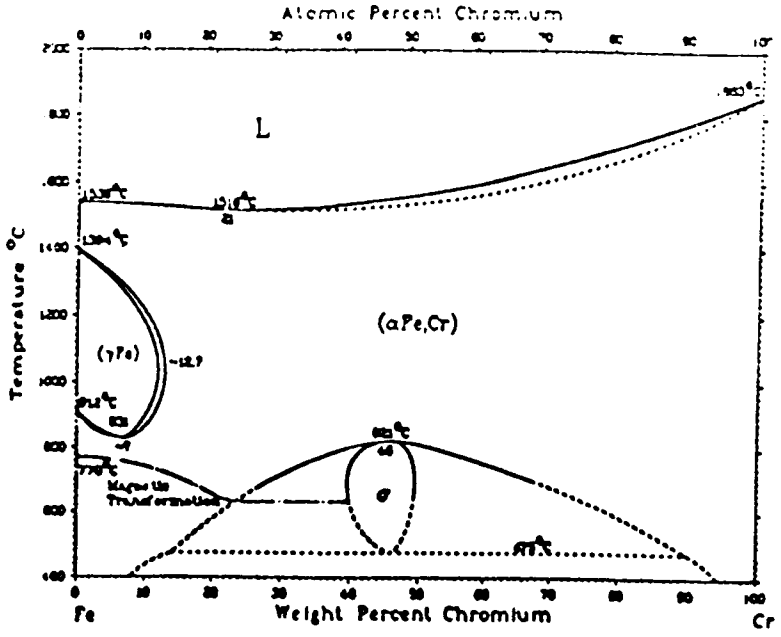

Figure 5.22 The Fe-Cr phase diagram

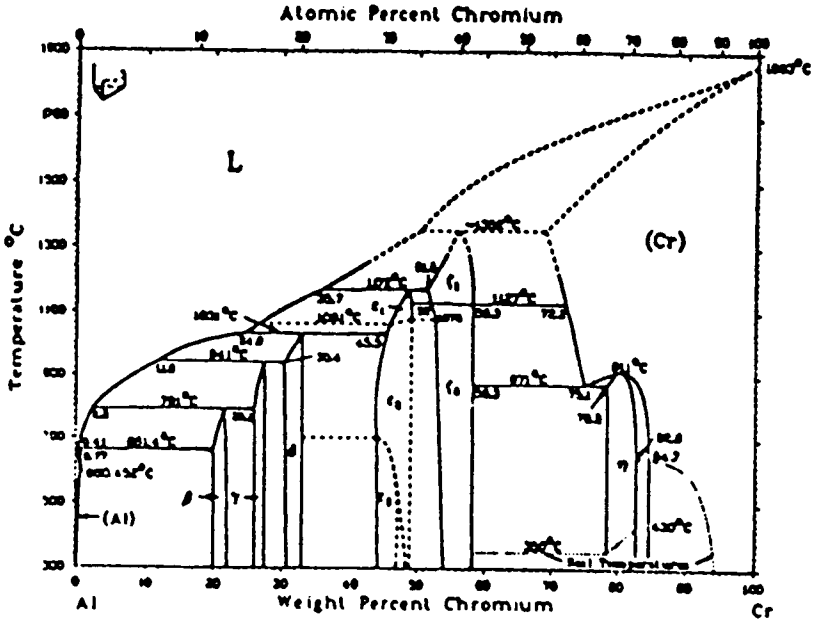

Figure 5.23 The Al-Cr phase diagram

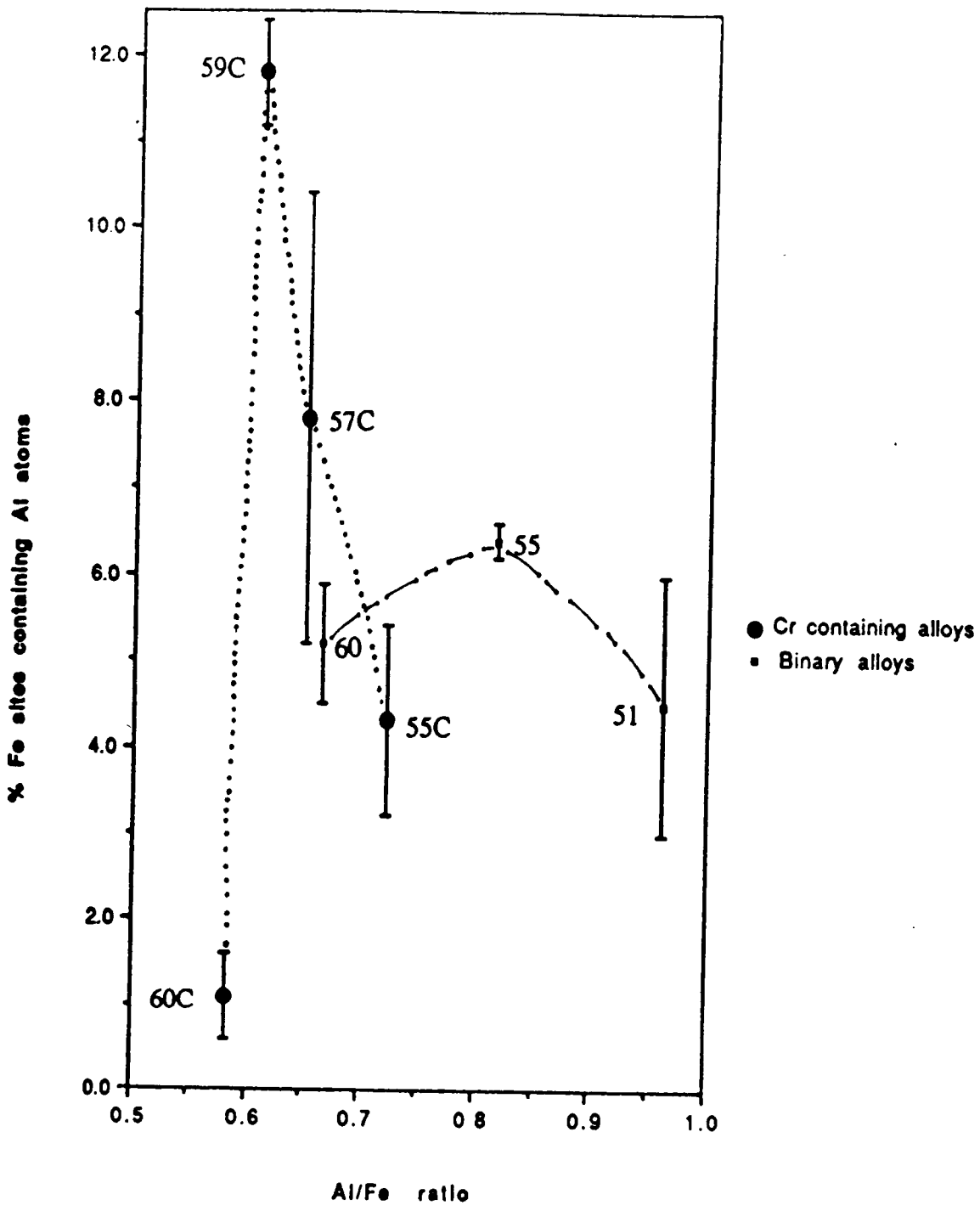

Figure 5.24 % anti-site defects vs Al/Fe ratio

Figure 5.25 Microstructure of $Fe_{59}Al_{36}Cr_5$ at magnification 50x

List of References

1. Albitani and Willis, " The Rietveld method in neutron and x-ray powder diffraction", Journal of Applied Crystallography, (1982) 15, p 361-374
2. Attfield, " Recent Advances in the Use of Anomalous Dispersion Effects", Accuracy in Powder Diffraction, (1992) p 175-182
3. Baker and Gaydosh, " Flow and fracture of Fe-Al", Materials Research and Engineering, 96 (1987), p 147-158.
4. J. Bentley, " Reliability of sublattice occupancies determined by ALCHEMI", Meeting of the Electron Microscopy Society of America.
5. Chang, Pike et al, " Correlation of the hardness and vacancy concentration in FeAl", Metallurgical Transactions A, vol 21 (1990), p 2283-2302
6. Crimp, Vedula and Gaydosh, " Room temperature tensile ductility in powder processed B2 FeAl alloys", Materials Research Society, 81 (1987), p 499.
7. Cullity, Elements of x-ray diffraction
8. Fleisher, Development potential of advanced intermetallic materials
9. Gaydosh, Draper and Nathal, " Microstructure and Tensile Properties of Fe40at. Pct. Al Alloys with C, Zr, Hf, and B Additions", Metallurgical Transactions A, vol 20A (1989), p 1701-1714
10. G.W.Groves and A.Kelly, Philosophical Magazine, 8 (1963).
11. Hardwick and Wallwork, Iron-Aluminum base alloys: A review of their feasibility as high temperature materials
12. Howard, Journal of Applied Crystallography (1982) vol 15, p 615-620
13. T. L. Johnson, R.P.Davies and N.S. Stoloff, Philosophical Magazine, 12 305 (1965).

14. Kumar, Sparks et al, " X-ray determination of site occupation parameters in ordered ternaries $Cu(Au_xM_{1-x})M=Ni,Pd$", Materials Research Society (1991), p 369 374

15. Larson and von Dreele, Generalized Structure Analysis System (1986).

16. A. Lefort et. al., " Mechanical Behaviour of $FeAl_{40}$ Intermetallic Alloys", Materials Research Society, vol 35 (1985), p 325-330

17. McKamey, Horton and Liu, " Effect of chromium on properties of Fe_3Al", Journal of Materials Research, 4 (1989), p 1156.

18. Madan G. Mendiratta, Sandra K. Ehlers, A review of recent developments in iron aluminides

19. Miedema, Boom and de Boer, " Crystal structure and chemical bonding in inorganic chemistry" (edited by C.J.M. Rooymans and A.Rabenau), North-Holland/American Elsevier (1975), p 163.

20. Miller, " Determination of the site occupation probability and the degree of order by APFIM", Journal of Microscopy, 147, part 2, August 1987, p 159-167.

21. Munroe and Baker, " Microstructure and mechanical properties of Fe-40Al+Cr alloys", Scripta Metallurgica, 24 (1990), p 2273-2278.

22. Nagpal and Baker, "Effect of Cooling Rate on Hardness of FeAl and NiAl", Metallurgical Transactions A, vol 21 A, (1990) p 2281-2282.

23. Ochiai, Oya and Suzuki, " Alloying behaviour of Ni_3Al, Ni_3Ga, Ni_3Si and Ni_3Ge", Acta Metallurgica, 32 No.2 (1984), p289-298.

24. Rietveld, Acta Crystallography, (1967) p 151-152

25. Schneibel, Grahle and Rosler, " Mechanical alloying of FeAl with Y_2O_3", Materials Science and Engineering (1992) p 684-690

26. E.M.Schulson, Res Mech 1(1981)111.

27. E.M.Schulson, C.C.Koch, C.T.Liu and N.S.Stoloff, High Temperature Ordered Intermetallic Alloys, Materials Research Society.

28. Sparks, Kumar, Specht et al, " Effect of powder sample granularity on flourescent intensity and on thermal parameters in x-ray diffraction Rietveld analysis", Advances in x-ray analysis (1992) p 357

29. Spence and Tafto, " ALCHEMI: a new technique for locating atoms in small crystals", Journal of Microscopy, vol 130, (1983) p 147-154

30. Titran, Vedula and Anderson, " High temperature properties of equiatomic FeAl with ternary additions", Materials Research Society, 39 (1985), p 309-317.

31. Turner, White and O' Connor, " Advances in ALCHEMI analysis", Journal of Microscopy, vol 162, (1991) p 369-378.

32. Wiles and Young, "A new computer program for Rietveld analysis of X-ray powder diffraction patterns, Journal of applied crystallography, (1981) 14, p 149-151

33. Wu, Tso, Sanchez, Tien, " Modelling of ternary site occupation in L12 ordered intermetallics, Acta Metallurgica, 37 No.10 (1989), p 2835-2840.

VITA

Sanjeev Khosla was born in Calcutta, India on November 29, 1966. He completed his schooling from La Martiniere for Boys, Calcutta in May 1985. In August 1985 he entered the Indian Institute of Technology, Kharagpur and graduated in Metallurgical Engineering in May 1989. In December 1989, he joined Cadbury India Limited, Bombay as a Trainee. In August, 1991 he took a study leave from Cadbury India Limited to pursue an M.S. in Metallurgical Engineering at the University of Tennessee, Knoxville. After completing all requirements for the completion of the degree, he is returning to Cadbury India Limited in September 1993. He will receive his degree from the University of Tennessee in December 1993.